NORTHWESTERN UNIVERSITY

Exploring Singlet Fission and Symmetry-Breaking Charge Separation using Ultrafast Optical Spectroscopy

A DISSERTATION

SUBMITTED TO THE GRADUATE SCHOOL
IN PARTIAL FULFILLMENT OF THE REQUIREMENTS

for the degree

DOCTOR OF PHILOSOPHY

Chemistry

By

Chenjian Lin

EVANSTON, ILLINOIS

December 2022

Abstract

Understanding the photophysical processes of organic materials is important for utilizing them as functional photonic materials. Typical photophysical processes include intersystem crossing, charge transfer (CT), symmetry-breaking charge separation (SB-CS), singlet fission (SF), etc. There are serval factors that can lead to different photophysical processes, such as the molecular energy levels, inter- and intramolecular interactions, solvent interactions, etc. Such factors can be adjusted by changing the forms of the materials or by synthetic approach. Especially for organic materials, there is more tunability by the synthetic approach.

Transient absorption (TA) spectroscopy is one of the most popular and useful platforms to investigate photophysical processes, since it has spectral resolution to differentiate most of the transient species, with the time resolution various from femtosecond to microsecond. One can understand the excited-state dynamics by deconvoluting the TA spectra with a specific dynamic model.

By using TA spectroscopy, and other ultrafast optical spectroscopies, we aim to enhance our fundamental understanding to the factors that can affect the photophysics. In this dissertation, we explore the SF and SB-CS processes for various materials in different forms, including solution, colloidal nanoparticle, polycrystalline thin film, single crystal. We also design and synthesize monomer, oligomer and donor-acceptor types of materials in order to further understand the structural-property relationship.

In Chapter 2, we investigate the substituent effects on the SF of a bis(phenylethynyl) anthracene (BPEA) system in nanoparticles form. In Chapter 3, we investigate another blue-absorbing chromophore perylenemoniimide (PMI), and find SF in the single crystal and thin film. In Chapter 4, we move to the synthetic approach by synthesizing a perylenediimide (PMI) dimer

and trimer, and investigate the effect of intramolecular coupling to coherent state mixing in the dimer and SB-CS in the trimer. Building on the results from Chapter 5, we further design and synthesize a perylene-di-perylenediimide system, and find the CT between the perylene and the PDI dimeric mixed-state.

We hope the studies in this dissertation can not only improve the understanding of the photophysics of the organic chromophores, but also provide new directions on designing and characterizing photonic materials.

Acknowledgment

We thank Prof. Michael Wasielewski, Prof. Lin Chen, Prof. Richard Schaller as the committees for this dissertation. We thank Dr. Younjue Bae for running the SAXS in Chapter 2. We thank Dr. Yue Qi and Malik Williams for running the fsTAM in Chapter 3. We thank Paige Brown for running the low-fluence fsTA and TRF in Chapter 3. We thank Dr. Michele Myong for running the XRD in Chapter 3. We thank Dr. Xingang Zhao for providing the starting materials for the synthesis in Chapter 3. We thank Dr. Robert Jacobberger for running the profilometry in Chapter 3. We thank Dr. Taeyeon Kim for running the broadband TA, fsIR and wavepackage analysis in Chapter 4. We thank Dr. Jonathon Schultz for analyzing the broadband TA result in Chapter 4. We thank Dr. Haochuan Mao and Fangbai Xie for providing the starting materials for the synthesis in Chapter 5. We thank Prof. Ryan Young for modifying the manuscripts for all the chapters.

Table of Contents

List of Tables, Illustrations, Figures, and Graphs

Introduction

Solar energy is an essential source of renewable energy. People have been studying the ways to harvest the solar energy for more than a hundred years. One of the most important ways to harvest the energy from the sun is to design a solar cell, which is a device that converts the energy of sun light into electricity. A typical solar cell requires three sequential steps to convert light into electricity. First, a functional molecule (absorber) absorbs a photon whose energy equals to the energy difference between the molecule's highest energy occupied molecular orbital (HOMO) and its lowest energy unoccupied molecular orbital (LUMO). The energy from the photon excites an electron from its ground state to an excited state and simultaneously generates a hole. Both the electrons and the holes are charge carriers which carry negative and positive charges, respectively. This electron-hole pair is called an exciton. Second, the opposite charges are separated either within the molecule, or by interacting to the charge transporting materials. Finally, the opposite charges reach the electrodes to generate an external circuit. To develop a solar cell with high efficiency, one can put efforts on enhancing the efficiencies of these steps.

Typically, in a silicon based solar cell device, when the energies of absorbed photons are higher than the band gap of the absorber, the excess energies will be wasted in terms of thermal energies.[1] To enhance the overall efficiency of the solar cell, it is important to utilize the higher energy (blue) photons in the solar spectrum. While there are countless molecules that can absorb blue photons, the energy of the generated exciton should be 1.1-1.3 eV in order to achieve the maximum theoretical efficiency in a single-junction solar cell.[2] Thus, it is important to have a photophysical process that can convert the high energy excitons to low energy excitons. Intersystem crossing (ISC) can be one of these processes, where the excited electron performs a spin-flip to generate a different spin state. Most absorbers generate singlet excitons directly after the photoexcitation, and after the ISC, triplet excitons with lower energies will be generated. Since the ISC evolves spin-forbidden transition, it will be relatively slow in most cases. The slow rate can cause it to be outcompeted by other irrelevant process, thus limit the overall efficiency. Singlet fission (SF) is a spin-allowed transition which converts a singlet exciton to two triplet excitons.[3] SF does not evolve a spin-flip due to the fact that the overall multiplicity of the two triplet excitons is still singlet. Thus, in most cases, SF will be faster than ISC and be more useful in the solar cell application. In Chapter 2 and Chapter 3 of this dissertation, we explore the fast SF in two different blue-absorbing systems. In Chapter 2, we study the factors that would increase the rate of SF in nanoparticle forms; in Chapter 3, we study the SF in solid state single crystals and thin films.

Besides by pairing the neutral excitons to charge transporting materials to separate their charges, one can also design charge transferring (CT) materials by incorporating electron donor and acceptor moieties into the molecule, to enable the charge separation (CS) within the molecule. It is important to enhance the rate of CS in order to improve the overall efficiency by suppressing the competing processes. In chapter 4 of this dissertation, we study a symmetry-breaking charge separation (SB-CS) system, where we find the acceleration of the SB-CS process can be achieved by having the electronic mixed state in the dimeric unit as the intermediate.[4] In chapter 5, we are further inspired by the idea in the previous chapter and attach the dimeric unit to an additional electron donor. We find that the charge is successfully harvested from the dimeric mixed-state. The charge recombination (CR) rate is also slower compared to the direct CT between the donor and the acceptor, enabling better efficiency for further transporting the charges.

We hope the results and discussions in this dissertation would further improve our understanding of structural-property relationship, and give inspiration on designing new functional materials for solar cell application.

Chapter 2. Singlet Fission in Nanoparticle Solutions of 9,10-bis(phenylethynyl)anthracene Derivatives

Singlet fission (SF) is a spin-allowed process where a photogenerated singlet exciton can down-convert into two triplet excitons via a correlated triplet pair state.[3] This process has received considerable attention since it was recognized that this SF has the potential to enhance the Shockly-Queisser efficiency limit of single junction photovoltaics from 33% to 45%.[2] This enhancement is due to mitigating thermalization losses that occur when the absorbed photons have higher energies than the band gap of the absorber,[1] which is a significant effect in silicon-based photovoltaic devices. Thus, it is desirable to expand the library of SF chromophores, particularly those that absorb higher energy (blue) photons that would otherwise be wasted.

Typically, SF requires the singlet energy to be twice that of the triplet state, although endoergic SF does occur in some systems.[5-7] In order to achieve the maximum theoretical efficiency in a single-junction photovoltaic cell, the triplet energy of the SF chromophore should be 1.1-1.3 eV.[2] One way to further harvest the triplet excitons from the SF chromophores is to pair them with a suitable electron acceptor or donor, where the charge carriers are generated via a charge separation (CS) process.[8-9] The SF rate should be fast enough to outcompete other irrelevant processes in order to have efficient CS from the triplet state. A high SF yield is also required for efficient CS to the terminal acceptor state. Engineering a SF system with a fast rate and subsequent high yield is therefore of considerable interest.

SF can be quite rapid, as it occurs via a correlated triplet pair intermediate, ^{1}(TT), which then dissociates to generate free triplets, making the overall process spin-allowed.[10] The ^{1}(TT) state can be accessed directly from the singlet excited state (S_1S_0) via a concerted two-electron process,[11-13] or indirectly by two consecutive electron transfer processes involving another intermediate state.[14]

Previous work has shown that the charge transfer (CT) states can serve in this role,[15-17] however the degree and type of coupling depends strongly on their energy. Specifically, if the CT state is energetically inaccessible, it can couple to S_1 and ^{1}(TT) via superexchange.[17-18] However, if the CT state is overly stabilized relative to S_1, the populated CT state will serve as an energetic trap and prohibit efficient SF.[16] While the energetics of the CT state – and hence the electronic coupling between S_1 and ^{1}(TT) – can be modulated with the local solvent environment to an extent, the precise balance of the couplings between the singlet excited, CT, and triplet states in optimizing the SF yield is still not well understood. Indeed, such environmental modulation is generally not possible in thin films, where the dielectric constants are low and CT states are often strongly destabilized.

Among the many reported SF chromophores, anthracene derivatives have the smallest organic conjugated system, which leads to bluer absorption. In particular, 9,10-bis(phenylethynyl)anthracene (BPEA) has been shown to undergo SF in solid-state films with $k_{\mathrm{SF}} = (109 \pm 4\ \mathrm{ps})^{-1}$ and a triplet yield of 180 ± 20%.[19-20] BPEA is a versatile and robust chromophore that is thermally and chemically stable and straightforward to synthesize. It is also easily synthetically tuned, with multiple positions available where substituents can alter the electronic properties of the BPEA core[19, 21]. Recently, we demonstrated how modifying the *para*-substituents on the phenyl moieties of BPEA can tune the interchromophore couplings for SF. For example, thin films of the di-fluorinated derivative were shown to have $k_{\mathrm{SF}} = (16 \pm 2\ \mathrm{ps})^{-1}$,[21] with the same 180 ± 16% triplet yield as thin films of the parent BPEA. The faster rate was attributed to a combination of electronic modulation of the BPEA core and slight changes in the interchromophore packing. However, other derivatives like 4,4’-dimethoxy-BPEA and 4-fluoro-

4’-methoxy-BPEA did not experience the same degree of rate enhancement, and the asymmetric 4-fluoro-4’-methoxy-BPEA showed a reduction in triplet yield to 110 ± 4%.

In order to enhance the rate of SF and triplet yield in BPEA systems, we need to further understand the interplay between environmental modulation of the CT state with entropy in larger extended systems. While covalent dimers offer precise control of interchromophore coupling and allow for facile solvent tuning, they do not provide a means for the triplet states to diffuse away and hence lower the entropy for the total SF process, which will have a major impact when the driving force for SF is small or slightly positive.[22] Moreover, the synthesis quickly becomes challenging when systems larger than two chromophores are considered, so this route quickly becomes limited.

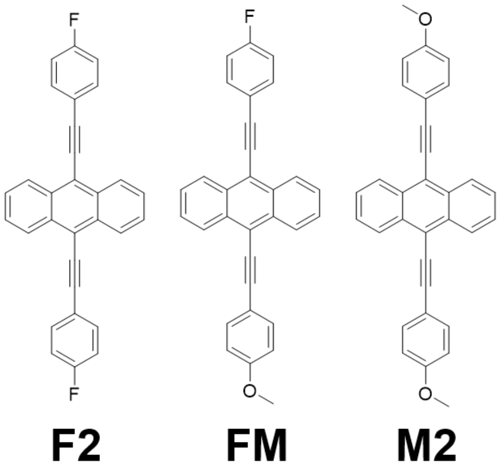

Figure 1. Chemical structures of BPEA derivatives.

Organic nanoparticles (NPs) provide a simple platform for studying creating size-controllable chromophore aggregates. With the high surface-to-volume ratio, a large portion of the chromophores can interact with the solvent environment, and many can be readily prepared in water.[23] The polar environment of aqueous organic NPs can lower the CT state energy to enhance the SF rate via the superexchange mechanism.[17] NPs are especially promising for studying the SF mechanism since NP fabrication is not synthetically intensive as it is with covalent oligomers and thus provides facile ways to tune coupling and entropy by varying the NP size. In addition, previous works on SF in aqueous NPs have found that the high dielectric environment favors SF when it occurs via the CT-mediated mechanism.[15] In fact, a recent study by Manna, et al. showed that the SF rate in BPEA NPs was enhanced to ca. $(25\,\text{ps})^{-1}$, indicating the importance of entropy gain and high dielectric environment afforded by the NP.[20]

In this work, we investigate the SF dynamics in nanoparticles of BPEA and its 4,4’-difluor-BPEA (**F2**), 4,4’-dimethoxy-BPEA (**M2**), and 4-fluoro-4’-methoxy-BPEA (**FM**) derivatives in colloidal aqueous suspensions (**Figure 1**). While the **F2** NP still shows a similar SF rate to the thin film, we find that NPs of **FM** and **M2** show an enhancement of the SF rate with the factor of four compared to the thin films, which we attribute to the higher singlet excited-state energies giving a larger driving force for SF, and the higher coupling afforded by stabilization of the CT intermediate state. Triplet lifetimes are also shown to be abbreviated compared to the thin films, which we attribute to quantum confinement by the finite volume of the nanoparticles leading to higher rates of triplet-triplet annihilation. These results show how the NPs provide a way to stabilize the CT state within an intrinsically low-dielectric organic medium while also providing sufficient electronic coupling and entropy for efficient singlet fission in BPEA.

Result and Discussion

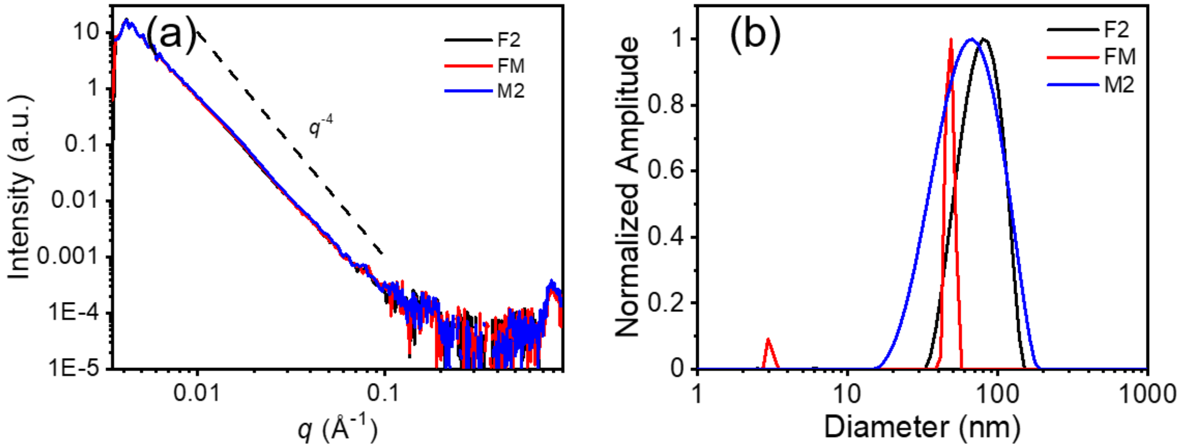

Figure 2. (a) SAXS data for the NPs. (b) Size distribution of the NPs

Structural Characterization

Structural and size information for the NPs was gained from Small Angle X-ray Scattering (SAXS). SAXS data of all three NP solutions (**Figure 2a**) show a linear relationship in the log-log plot of the scattering intensity and the scattering factor q. The slope of each plot is about -4, which confirms that the NPs are spherical.[24] There are no obvious diffraction peaks, indicating that no long-range ordering exists in the NPs. The sizes of the NPs were measured immediately after preparation by Dynamic Light Scattering (DLS, **Figure 2b**). All the NPs were polydisperse with polydispersities of 20-60% and the mean diameters of 40-80 nm (**Table 2**). DLS measurements were taken on irradiated samples and week-old non-irradiated samples and we found no obvious size changes, which indicates that the NPs are stable on this timescale (**Table 2**).

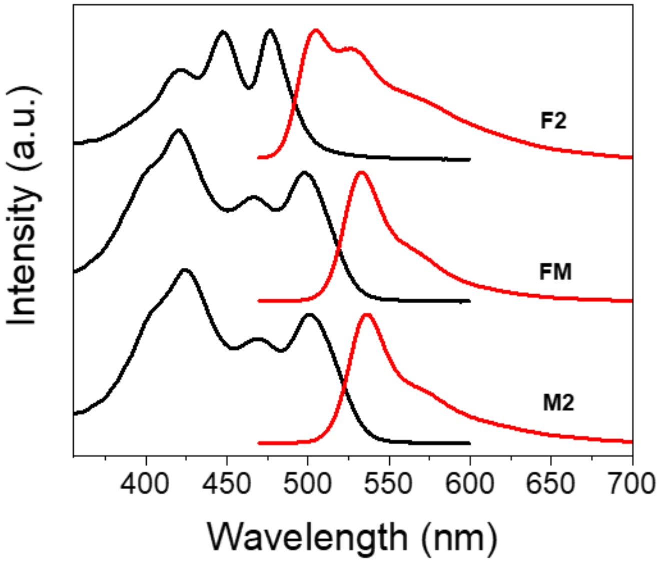

Figure 3. Absorption (black) and fluorescence (red) spectra of **F2** (top), **FM** (middle), and **M2** NPs (bottom)

Steady-State Spectroscopy

The absorption and fluorescence spectra of the NPs are shown in **Figure 3**. The absorption spectrum of the **F2** NPs exhibit broadening and are red-shifted compared to solution (**Figure 6**), however, they are narrower and less red-shifted than those of the films.[21] Additionally, the vibrionic peaks in the NP spectrum are similar to those in films. The intermediate nature of the NP absorption spectrum indicates that the interchromophore interaction in the NPs falls into a medium coupling regime between that of the solutions and the solid-state films. The fluorescence spectrum of the **F2** is also less broadened and red-shifted than that in film (**Figure 6**). Specifically, the broad red emissive peak in the film at 575 nm, which may originate from the radiative decay of the strongly coupled excimers, is not present in the NPs. The lack of excimer emission is ideal as excimers can trap excitons and hinder efficient SF. Again, this corroborates the previous assumption that the NPs have moderate interchromophore coupling. Strong quenching of the fluorescence (< 0.5%) in the NPs compared to the near-unity emission in solution suggests that there is a nonradiative decay channel induced by the interchromophore coupling. Similar behaviors of the absorption and fluorescence were found in NPs of **FM** and **M2** (**Figure 6**). By taking the crossing points of the normalized absorption and emission spectra (**Figure 3**), the singlet energies (E_{S1}) of the NPs can be calculated, which are 2.52, 2.39 and 2.37 eV for **F2**, **FM**, and **M2**, respectively. Importantly, the values of E_{S1} of the NPs are all slightly higher than those in films (2.48, 2.34 and 2.34 eV, respectively).[21]

Singlet Fission Dynamics

We performed fsTA spectroscopy of the NPs to further understand the nonradiative decay pathway upon excitation. The dynamics were analyzed by fitting the kinetic data at multiple wavelengths with a sequential 4-state (A → B → C → Ground state) model that considers the effects of singlet-singlet annihilation (see Method section for details). Upon photoexcitation of **F2**, a board absorption band appears between 550-750 nm (**Figure 4a**), which is attributed to the excited-state absorption (ESA) of the S_1 state (species A in **Figure 4b**). The small dip at 530 nm represents the stimulated emission (SE), which is corroborated by steady-state fluorescence. After tens of picoseconds, the broad S_1 ESA decays rapidly, forming an intermediate species with an absorptive peak at 500 nm (species B). The intermediate species decays after hundreds of picoseconds and generates a long-lived species (species C), which does not decay in the 7 ns time window of our instrument. By comparing the triplet sensitized spectra in solution and in film to the residual signal, we attribute this long-lived species C to the triplet state, T_1.[21] The triplet ESA signal also overlaps with the GSB between 420-500 nm. Given that the rate of triplet formation occurs in the scale of ten picoseconds in these NPs whereas a typical intersystem crossing in organic molecules occurs in nanoseconds, we conclude that the triplet excitons are generated by

SF. We assign the intermediate species B to the correlated triplet pair, ^{1}(TT), which then dissociates to form two triplet excitons.

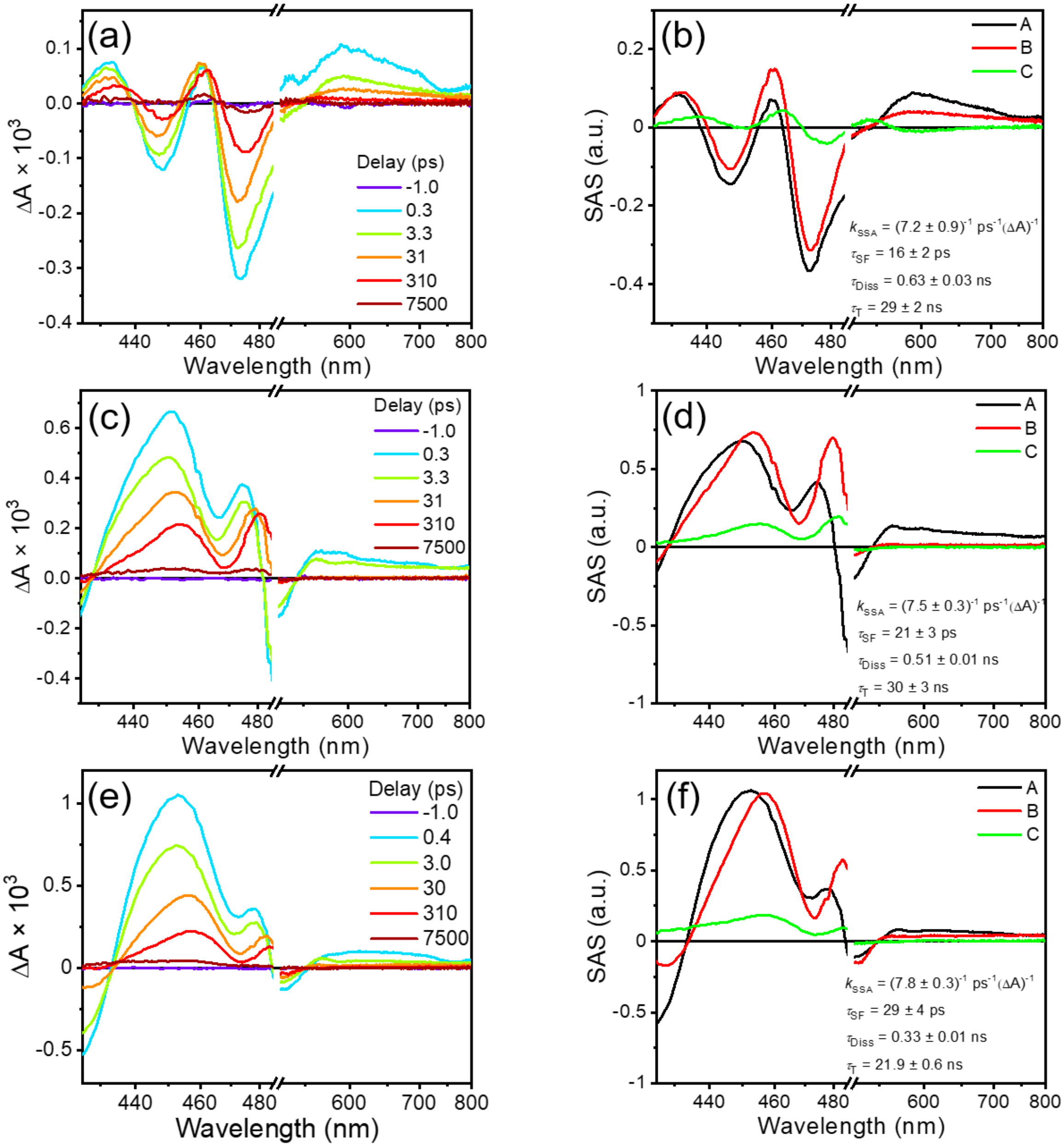

Figure 4. TA spectra of **F2** (a), **FM** (c), and **M2** (e) at selected delay times. Species-associated spectra for **F2** (b), **FM** (d), and **M2** (f). The last lifetimes are from the nsTA experiment

The species-associated spectra (**Figure 4b, d, f**) were extracted from the data using the kinetic fits; the longest reported lifetimes are from nsTA measurements. We observed similar excited-state kinetics in all the NPs with different rate constants. The excited-state kinetics are different from those in films, which may due to the high dielectric environment of NPs. Additionally, the packing of the molecules in NPs may be different from that in films. The comparison of the SF rates in NPs and in films are summarized in **Table 1**. We note that the global analysis assumes a homogeneous environment that likely over-idealized. For example, surface molecules will behave differently than the molecules at the NP core due to the different environment. Polydispersity of the size induces further heterogeneity.[15] Nonetheless, the assumption is useful when comparing the rates between NPs and films, where similar assumptions must also be made.

Table 1. SF rates of **F2**, **FM** and **M2** in NPs and films

Sample	**k_{SF} (NPs)**	**k_{SF} (Films)**[21]
F2	$(16 \pm 2\ \text{ps})^{-1}$	$(16 \pm 2\ \text{ps})^{-1}$
FM	$(21 \pm 3\ \text{ps})^{-1}$	$(90 \pm 20\ \text{ps})^{-1}$
M2	$(29 \pm 4\ \text{ps})^{-1}$	$(120 \pm 17\ \text{ps})^{-1}$

To further confirm the existence and influence of the singlet-singlet annihilation in the kinetic model, we compared the fsTA data under the pulse energies of 1 μJ/pulse and 20 nJ/pulse (**Figure 12**). The excitation density dependence of the kinetics confirms that there is bimolecular singlet-singlet annihilation. We observed a lesser degree of thermal modulation in the 20 nJ/pulse data due to the low pump fluence.

The SF rates in **FM** and **M2** are faster than those in films. There are several contributing factors to this rate enhancement, such as the changes in energetics and interchromophore coupling between the NPs and thin films. From the steady-state spectra in **Figure 6** we determine that the singlet excited state energy of each derivative is slightly higher in the NPs than in the thin films. This suggests a subtle change in the chromophore packing, which will not only weaken the coupling but also the relative energetics. Assuming that the energy of the correlated triplet pair ^{1}(TT) is twice that of the isolated triplet in the thin film (<1.12 eV),[21] the driving force for SF can be calculated to be at most -0.28, -0.15 and -0.13 eV for **F2**, **FM**, and **M2**, respectively. This is ~0.05 eV more negative than the driving forces in the respective films.

Stabilization of the CT state by the aqueous solvent may also be influencing the dynamics, as any excitons experiencing the high polarity environment near the surface will exhibit a stronger coupling as the energy difference between the singlet and CT states is reduced. Though this effect would be strongest near the surface of the NP, we estimate that there are about 10% surface molecules in the NPs based on an idealized packing model (see additional data), suggesting that they will have an active role in the photophysics. Light absorption is also favored towards the surface, as light penetration is exponentially less likely deeper into the interior of the NP. Importantly, despite the high dielectric constant of water at the interface, the CT state of BPEA is not so sufficiently stabilized to result in full symmetry-breaking charge separation as seen in molecular dimers of BPEA in less polar solvents like DMF and DCM.[25] This may also be due in part to the lower dielectric environment provided by the aromatic BPEA units from the interior the NP balancing the rapidly decaying influence of the polar solvent farther from the interface. However, the propensity to undergo symmetry-breaking charge separation in these dimers was dictated strongly by the lateral slip distance between the BPEA cores; only dimers slipped by two phenyl spacers showed significant symmetry-breaking in polar solvents. Thus, the difference in packing structure as indicated by the steady-state absorption spectra together with the moderate stabilization afforded by the environment enables sufficient coupling, and hence efficient SF.[26]

Additionally, the entropy gain associated with SF may also be a contributing factor here, however we note that this effect is present in the thin films.

Triplet Dynamics

The rapid singlet-singlet annihilation observed in the high-fluence fsTA experiments suggests that a significant amount of thermal energy is being deposited in the sample at early times, which could cause a distortion in the ground-state absorption and the appearance of triplet-like derivative features in the TA spectra. We acquired the UV/vis spectra at elevated temperatures and constructed the thermal difference spectra to compare to the long-lived T-T absorption features in the TA data, shown in **Figure 5**. The thermal difference spectra are from the subtraction of the absorption spectra at 25 ^{o}C and 55 ^{o}C, and the TA spectra are from the species-associated spectra of the species C (triplet) in nsTA (**Figure 9-11**). The two spectra are then scaled to match at the lowest intensity.

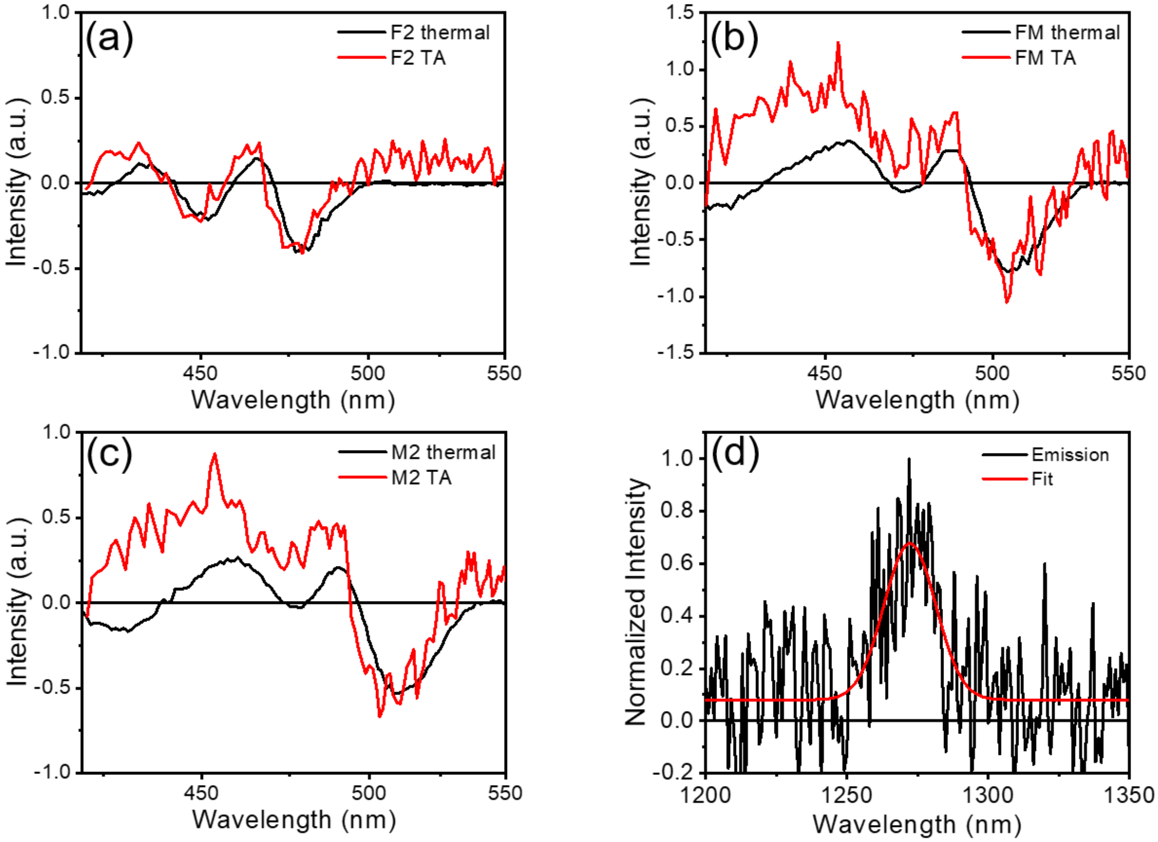

Figure 5. The comparison between the thermal difference absorption spectra (black) and TA spectra (red) of **F2** (a), **FM** (b), and **M2** (c) at selected delay times. Singlet oxygen emission spectrum of **F2** (d)

In NPs of **FM** and **M2**, we found that the nsTA features are different from those in the thermal difference absorption spectra (**Figure 5b, c**). Specifically, besides the GSB region at 480-530 nm, the TA features at 400-480 nm are all absorptive, where the thermal difference absorption spectra show alternating absorptive and emissive features. This confirms that the long-lived species are not purely from the thermal alteration of the ground state absorption. Though the TA features of **F2** look similar to the thermal-difference absorption spectra (**Figure 5a**), singlet oxygen ($^1O_2$)

emission was observed in this derivative (**Figure 5d**), indicating the presence of triplet excitons in some yield. Thus, we assign the long-lived species of all the NPs are from the SF-generated triplet.

Although it's technically difficult to calculated the triplet yield of the NPs using the traditional methods (singlet depletion and spectral deconvolution[19]) due to the uncertainty of the NP's microscopic structure, the faster SF rates in NP compared to those in films suggest that the yield of the correlated triplet pair ^{1}(TT) would be similar or greater than those in the films. The decorrelation lifetimes of **F2**, **FM**, and **M2** are 0.63 ± 0.03 ns, 0.51 ± 0.01 ns, and 0.33 ± 0.01 ns, respectively, which are also shorter than those in films (1.2 ± 0.3 ns, 1.1 ± 0.1 ns, and 2.3 ± 0.6 ns, respectively[21]). Reports have shown that fast decorrelation rates can reduce the chance for the ^{1}(TT) to evolve via other pathways, which would consequently enhance the triplet yields.[27-28] Since the triplet yields in films are relatively high (180±16%, 110±4%, 168±7% for **F2**, **FM**, and **M2**, respectively[21]), and the SF rates and the decorrelation rates are even faster in NP, we speculate that the triplet yields in NP are on the similar or greater level than those in films.

The triplet lifetimes of **F2**, **FM**, and **M2** are 29 ± 2 ns, 30 ± 3 ns, and 21.9 ± 0.6 ns, respectively, which are all shorter than those in films (74 ± 10 ns, 82 ± 8 ns, and 29 ± 8 ns, respectively[21]). We attribute the abbreviation of the triplet lifetimes to quantum confinement by the finite volume of the nanoparticles leading to higher rates of triplet-triplet annihilation.

In conclusion, NPs of **FM** and **M2** in water each exhibit SF rates about four times faster than those in their respective thin films. The aqueous solution of NPs provides a polar environment towards the surface of the NP to lower the CT state energy which enhance the SF rate via superexchange coupling. We believe that higher singlet energies and the moderate interchromophore coupling in NPs also favors the SF process. Though SF has been known for years, there is still a lack of fundamental studies of SF in blue-absorbing chromophores. In such systems, creating a polar environment, maximizing the E_{S1} while maintaining a moderate interchromophore coupling appears to be the most important factor for SF rates based on the results shown here.

Methods and Additional Data

Nanoparticle (NP) Preparation

F2, **FM**, and **M2** derivatives were synthesized as previously described.[21, 29] NP preparation was performed by the reprecipitation method.[23]

A THF solution (200 μL of ~4 mM) of **F2**, **FM**, or **M2** was injected into 10 mL of H_2O (HPLC grade, Sigma-Aldrich) while rapidly stirring. The samples were syringe-filtered (0.45 μm, Fisher Scientific) to remove large precipitates.

Small Angle X-ray Scattering (SAXS)

Small Angle X-ray Scattering (SAXS) data were acquired at the Advanced Photon Source (APS), Argonne National Laboratory using a Pilatus 2 M detector with 14 keV incident radiation. Subtracting the solvent scattering intensity from the sample scattering gives the scattering contributed by the NPs.

Dynamic Light Scattering (DLS)

The average particle sizes and size distributions were measured on Punk system at Keck Biophysics Center, Northwestern University using a 660 nm laser diode. The samples were 10-fold diluted before each measurement. 5 μL samples were loaded into disposable blade cells, and 10 sequential data frames with exposure times of 10 s were recorded, selected, and averaged for each measurement. All the measurements were done at 20.0 ± 0.2 ^{o}C. Brownian motion of each NP was tracked in real-time and deconvoluted to give the size distribution in hydrodynamic diameter using a spherical particle model. The spherical shape of the NP was confirmed by SAXS measurements. Peaks with less than 5% intensity area were ignored in the data analysis.

Table 2. Sizes and polydispersities of the NPs

Sample	Condition	Diameter / nm	Std. Dev. / nm	Polydispersity
F2	As prepared	74	33	45%
	Irradiated	79	33	41%
	Week-old	75	32	43%
FM	As prepared	48	10	22%
	Irradiated	47	11	24%
	Week-old	46	23	50%
M2	As prepared	62	38	61%
	Irradiated	82	51	62%
	Week-old	74	50	67%

*Only accounting the main size-distribution peak (> 90%)

Steady-State Spectroscopy

Steady-state absorption spectra were measured on a Shimadzu UV-3600 UV/Vis/NIR spectrometer under room temperature. Samples were measured using 1 cm quartz cuvettes with neat solvent as a reference. The temperature of the samples for the thermal-difference spectra measurements was regulated using a thermoelectric cuvette holder (Flash 100) with a temperature controller (Quantum Northwest).

Fluorescence spectra were obtained using a Horiba Nanolog spectrofluorimeter (FL3-2iHR/iHR). Samples were measured using 1 cm quartz cuvettes. Monochromatic light for excitation was generated using a 450 W Xenon lamp (Ozone free, FL-450XOFR) followed by a

1200 line/mm grating blazed at 330 nm. The emission light was diffracted using a 1200 line/mm grating blazed at 500 nm. A PMT detector (PPD-850) was used to capture the emission spectra.

The fluorescence quantum yield measurements were acquired on the same instrument with an integrating sphere (Horiba Quanta-φ). The emission spectra of the samples and blank solvent were measured inside the integrating sphere under the same conditions. The Rayleigh scatter peak was used to monitor the relative intensity of the transmittance. The quantum yield Φ was calculated using the formula as shown below.

Equation 1

$$\Phi = \frac{corr(Int) - corr(Int_R)}{corr'(Ray_R) - corr'(Ray)}$$

Int and Ray are the area under the fluorescence peak and the Rayleigh scatter peak, respectively, on a wavelength scale. $corr$ and $corr'$ are the built-in correction functions for the intensity of the fluorescence peak and the Rayleigh scatter peak, respectively. Subscript R represents the reference sample (blank solvent).

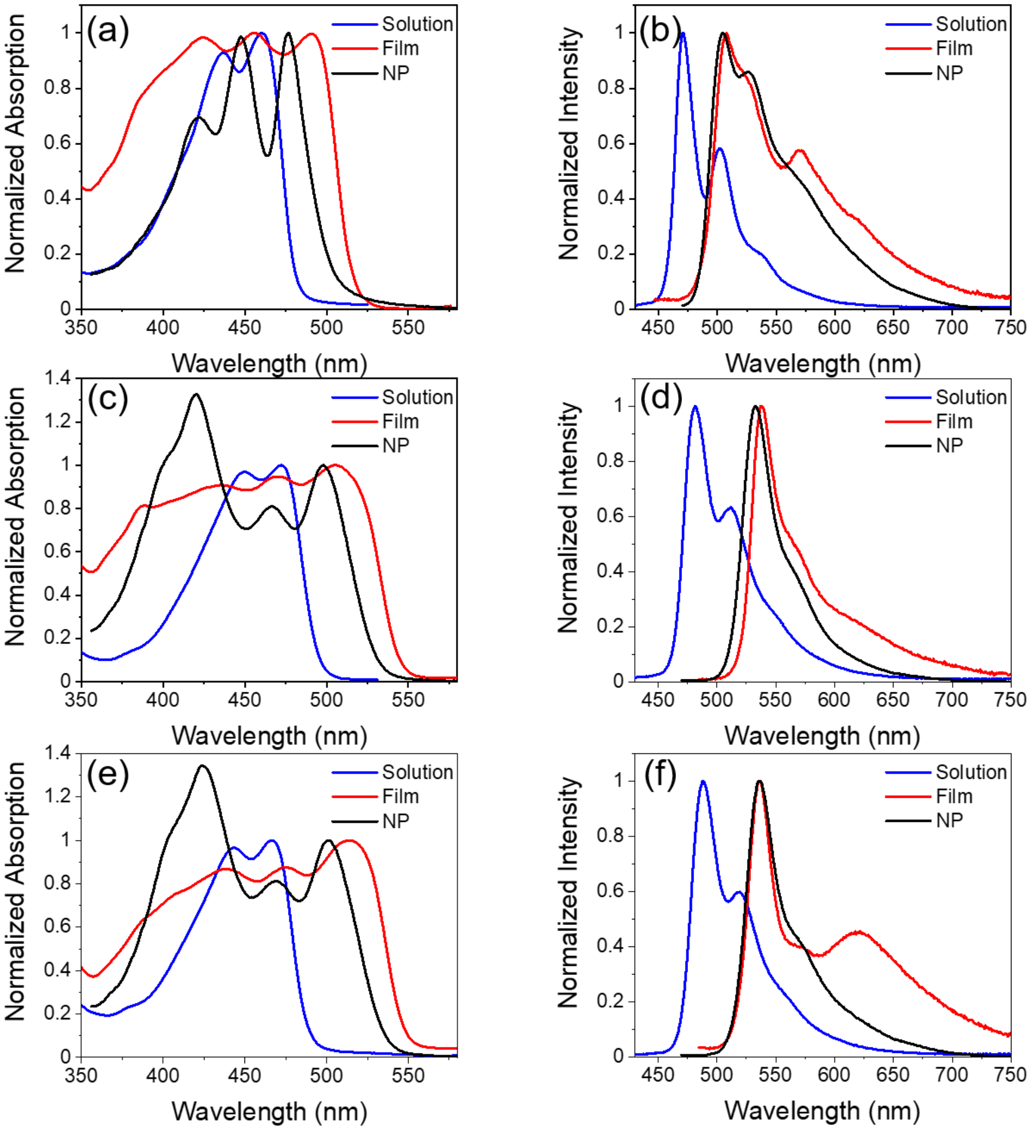

Figure 6. Comparison of the absorption (left) and fluorescence spectra (right) of **F2** (a, b), **FM** (c, d), and **M2** (e, f) in solution, film and NP forms. The solution and film data were reported previously[21]

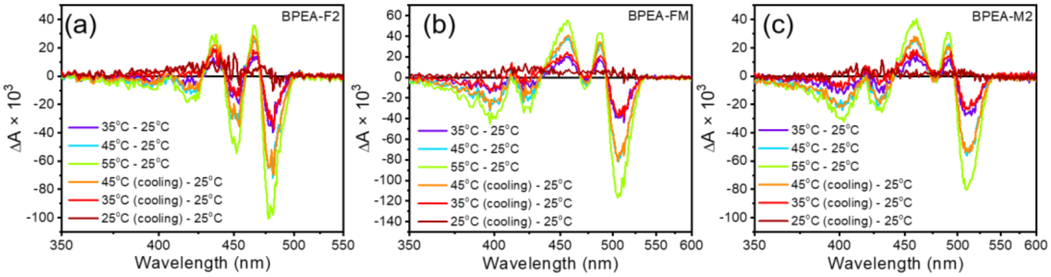

Figure 7. Thermal difference absorption spectra for **F2** (a), **FM** (b), and **M2** (c)

Transient Absorption (TA) Spectroscopy

High-fluence femtosecond transient absorption (fsTA) spectroscopy was performed on an amplified Ti:sapphire laser system described in detail previously.[30] Pump pulses at 414 nm (1 μJ/pulse) were generated by frequency-doubling the 827 nm fundamental. Nanosecond transient absorption (nsTA) spectroscopy was performed using a commercial spectrometer (EOS, Ultrafast Systems) with the same excitation beams as the high-fluence fsTA experiments. Low-fluence fsTA measurements were performed using a regeneratively amplified Yb:KGW laser system (Spirit One, Spectra-Physics, Inc.) operating at 100 kHz pumping a collinear optical parametric amplifier (Spirit-OPA-8, Light-Conversion, LLC). The 828 nm OPA output was frequency-doubled in an β-barium borate crystal to generate 1-20 nJ, 414 nm pulses of ~180 fs duration. The probe was generated and the spectra were recorded using methods previously described[30-31]. Samples were measured in 1 mm quartz cuvettes and were bubbled with N_2 for 20 min before each measurement. All time-resolved measurements were carried out at room temperature. Details of the kinetic fitting procedure have been described previously.[32]

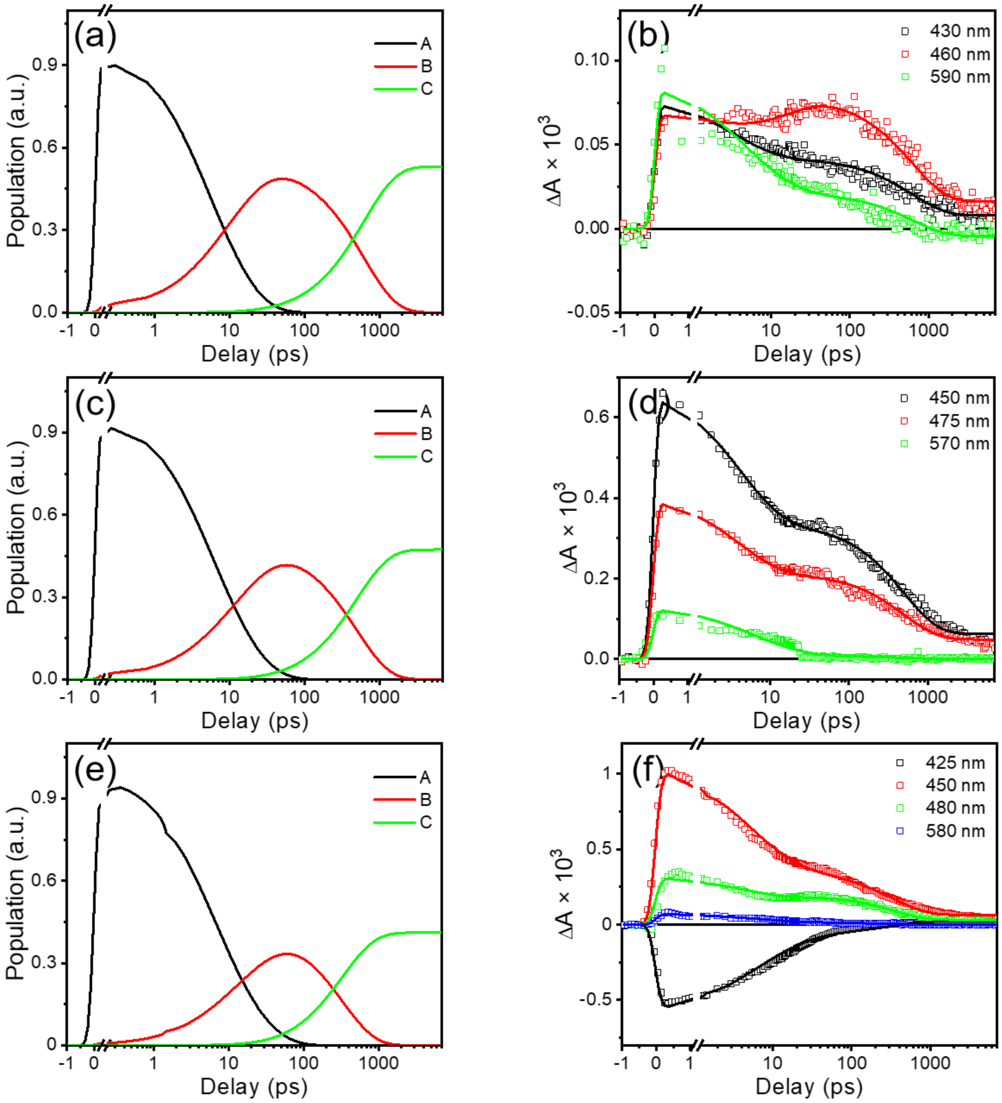

Figure 8. Additional fsTA spectra. Population distribution of the kinetic model for **F2** (a), **FM** (c), and **M2** (e). Kinetic traces at selected wavelengths for **F2** (b), **FM** (d), and **M2** (f)

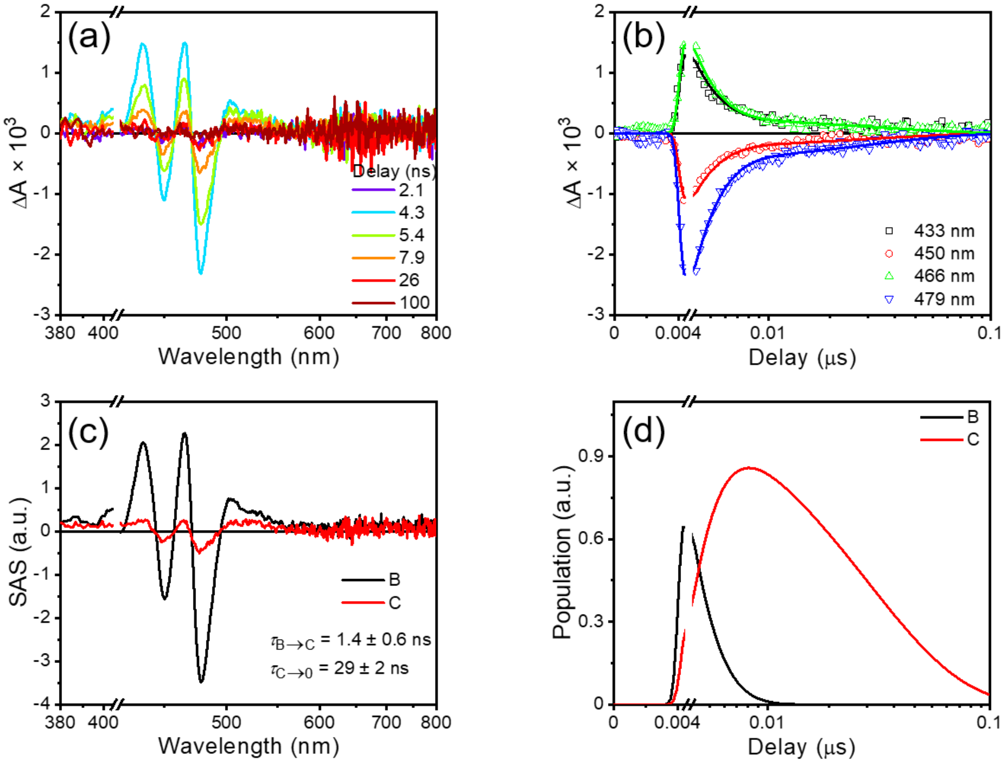

Figure 9. NsTA spectra of F2 (a) TA spectra at selected delay times. (b) Kinetic traces at selected wavelengths. (c) Species-associated spectra obtained by wavelength global fitting to a B → C → Ground state kinetic model. (d) Population distribution of the kinetic model.

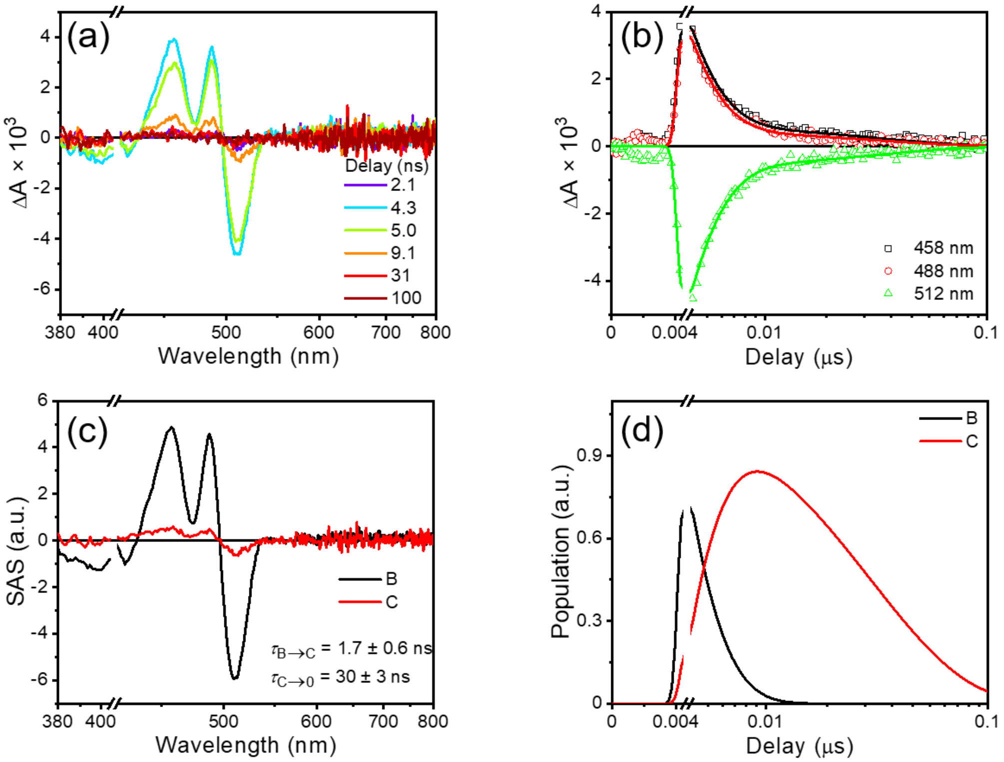

Figure 10. NsTA spectra of FM (a) TA spectra at selected delay times. (b) Kinetic traces at selected wavelengths. (c) Species-associated spectra obtained by wavelength global fitting to a B → C → Ground state kinetic model. (d) Population distribution of the kinetic model.

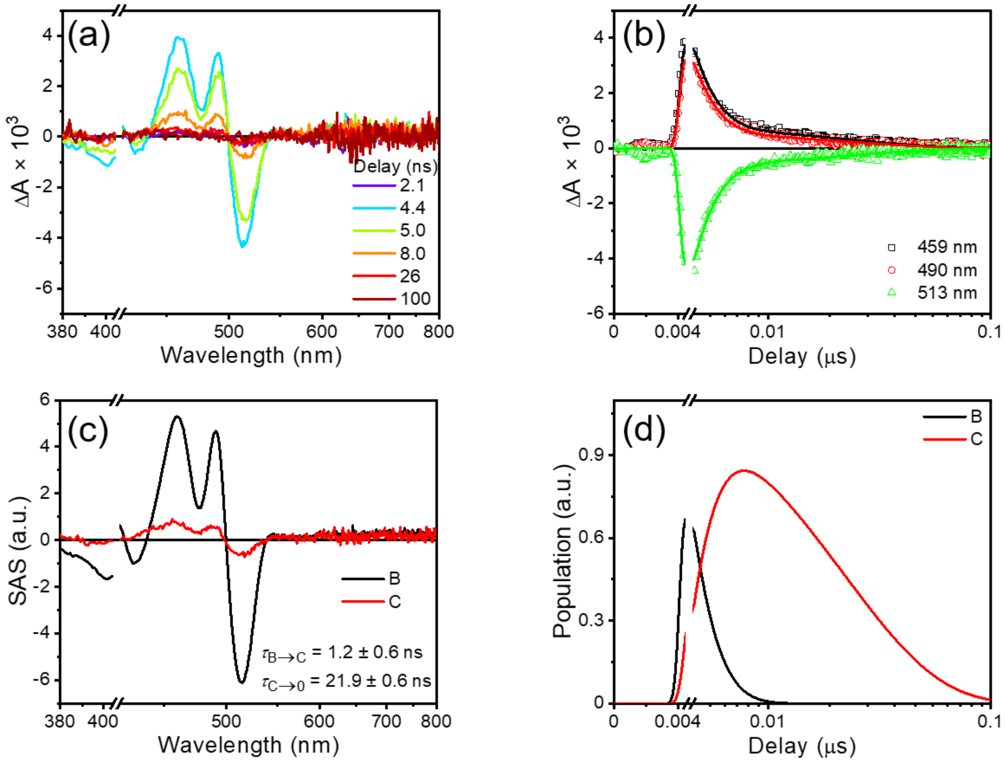

Figure 11. NsTA spectra of **M2** (a) TA spectra at selected delay times. (b) Kinetic traces at selected wavelengths. (c) Species-associated spectra obtained by wavelength global fitting to a B → C → Ground state kinetic model. (d) Population distribution of the kinetic model.

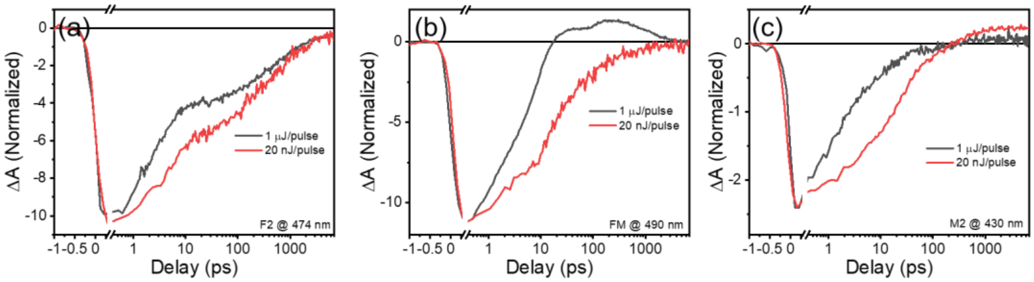

Figure 12. Comparison of the fsTA kinetic traces collected at different pulse power for **F2** (a), **FM** (b), and **M2** (c) at selected wavelengths. The spectra were normalized to the maximum bleaching

Estimation of the Surface Portion

By a rough optimization of the BPEA molecules using the force field and molecular mechanics (~21×12 Å^2), and assuming the depth of the molecule as twice of the π-stacking distance (~2×4 Å), we can consider a BPEA molecule as a cuboid with the size of 21×12×8 Å^3. Assuming that these cuboids are closely packed to form the NP as a cube with 80 nm length, there will be approximately 38×67×100 cuboids inside the cube. Ignoring the doubly-counted cuboids on the edges, the number of the surface cuboids can be estimated using the Equation 2, where φ is the ratio of the surface cuboids, and a, b, c, are the numbers of the cuboids on each edge.

Equation 2

$$\boldsymbol{\varphi \approx \frac{2 \times (ab + bc + ca)}{abc} = \frac{2 \times (38 \times 67 + 67 \times 100 + 100 \times 38)}{38 \times 67 \times 100} \approx 10\%}$$

We note that this estimation is based on a very idealized model. The actual surface portion can be infected by the packing of the molecules, and the size and the polydispersity of the NP, etc.

Chapter 3. Singlet Fission in Perylenemonoimide Single Crystals and Thin Films

Among the many chromophores reported to undergo SF, perylene-3,4:9,10-bis(dicarboximide) (PDI) derivatives have emerged as robust candidates for applications because SF occurs with high efficiencies even though it is slightly endoergic. The physical properties of PDI can be readily changed by modify the functional groups on the periphery of the molecule. For example, by eliminating one imide group, perylene-3,4-dicarboximide (PMI) has a higher singlet excited state energy than PDI, while retaining its low triplet state energy ($E_T \sim 1.1$ eV)[33]; thus making SF in PMI systems slightly exoergic.[33] While there have been three reports on SF in PMI covalent dimers,[33-35] there are no SF studies of PMI in the solid state, which is important for solar cell applications.

It has been shown earlier that slip-stacking of adjacent PDI π systems along their N-N axes results in efficient SF in the solid state.[36-37] We have now synthesized 2,5-diphenyl-*N*-(2-ethylhexyl)perylene-3,4-dicarboximide (**dp-PMI**), whose phenyl groups enforce crystallization with slip-stacking along the long molecular axis. Transient absorption spectroscopy and microscopy show that **dp-PMI** SF to form the ^{1}(TT) state occurs in 20.0 ± 0.3 ps in single crystals and in $\tau = 9.4 \pm 0.6$ ps in polycrystalline thin films with a triplet yield of 150 ± 20 %. Ultrafast SF in the solid state and the high triplet yield make **dp-PMI** an attractive candidate for SF-based solar cells.

Result and Discussion

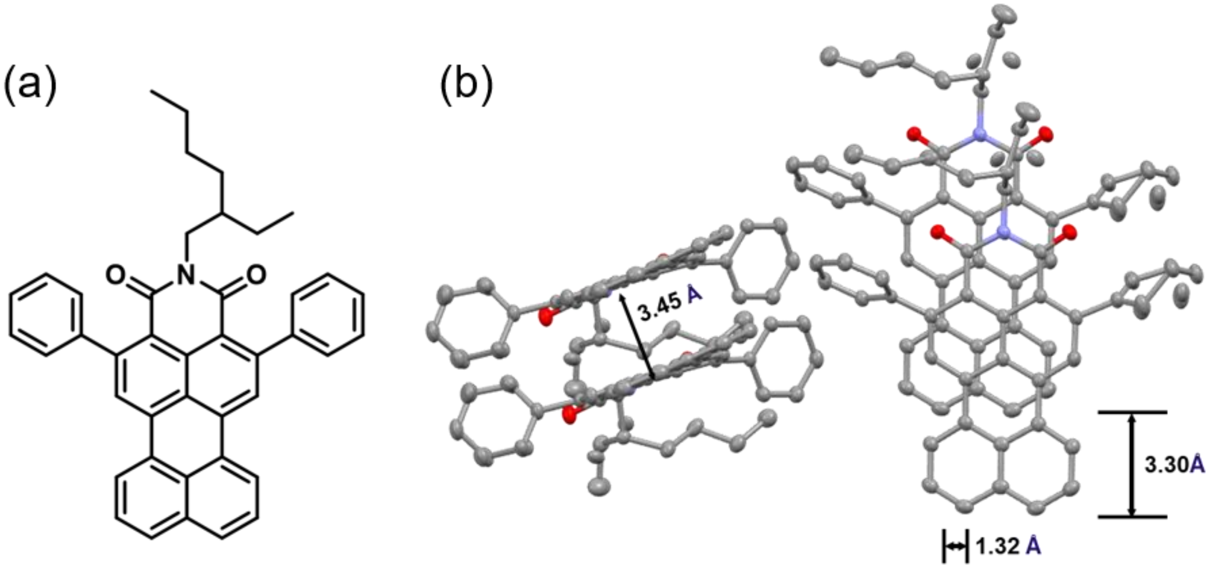

Figure 13. (a) Molecular structure of **dp-PMI**. (b) Crystal structure of **dp-PMI.**

Synthesis and Structural Characterization

dp-PMI was synthesized by C-H activation of the 2,5-positions of PMI with a Ru catalyst in the presence of phenylboronic ester using published procedures (**Figure 13a**).[38] The two phenyl rings on the 2,5 positions are designed to prevent cofacial stacking of the molecules in the solid state, which is well known in unsubstituted rylene systems.[39] Cofacial stacking often leads to strong intermolecular electronic coupling that can result in excimer state formation, which can serve as a trap state and kinetically outcompete SF. While it is also possible that the excimer state can be an intermediate in the SF photophysical mechanism,[40] slip-stacking of the molecules has proven to be a preferred structure to achieve high-performance SF in many cases.[41-42]

Single crystals of **dp-PMI** were grown by the vapor diffusion method in chloroform solution (~0.1 mg/mL) with methanol as the antisolvent. Intensity data of a single crystal of **dp-PMI** were collected at 100.0 K (see additional data). The XRD crystal structure of **dp-PMI** shows that the molecules are slip-stacked as designed (**Figure 13b**). While the adjacent molecules still interact via π-π stacking, the large dihedral angle between the phenyl rings and the perylene core provides sufficient steric hindrance for the molecules to be slip-stacked mainly along the molecular long axis. There are two main π-π stacking directions in the unit cell, both of which have similar stacking patterns. The π-π distance is 3.44 Å, and the slipping distances are 3.26 Å and 1.32 Å for the molecular long and short axes, respectively.

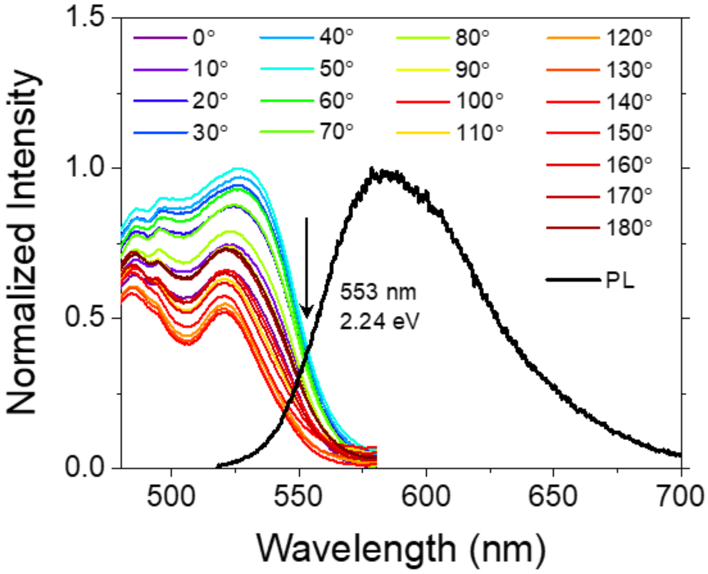

Figure 14. Normalized polarization-dependent absorption spectra and the photoluminescence spectrum of the **dp-PMI** single crystal. Photoluminescence spectra were taken from integration of the time-resolved fluorescence data (see additional data).

Steady-State Spectroscopy

Polarization-dependent absorption spectra of **dp-PMI** single crystals show that the absorption intensity increases when the probe polarization changes from parallel to perpendicular to the crystal long axis, although the absorption band edge broadens and red shifts about 25 nm (**Figure 14** and **Figure 19**). There is no obvious polarization-dependent peak shift present in the data; thus, we will use the most absorptive polarization (parallel to the crystal short axis) for the transient absorption measurements. The polarization-averaged absorption spectrum of the crystal strongly resembles that of the polycrystalline film. The singlet energy E_S defined as the crossing point of the normalized absorption and emission spectra the singlet energy in the single crystal and the polycrystalline thin film is E_S = 2.24 eV.

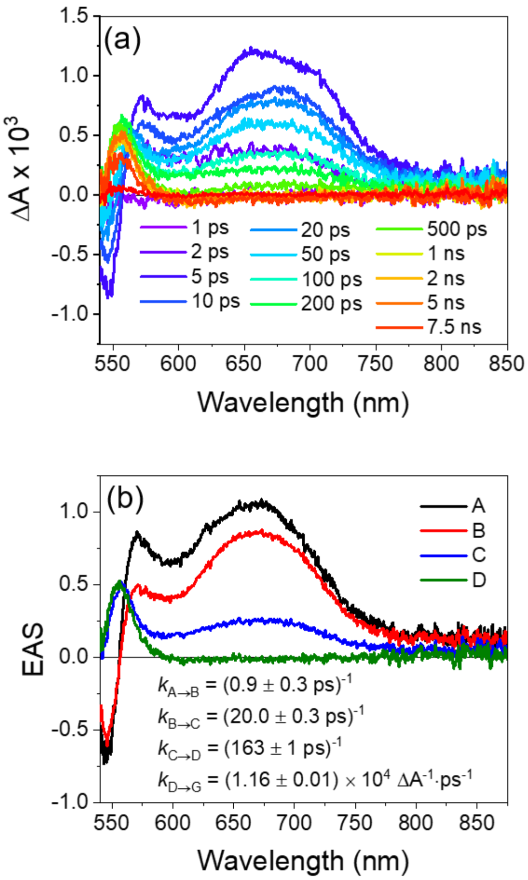

Figure 15. (a) FsTA spectra (ex: 480 nm, 20 nJ/pulse) of **dp-PMI** in single crystal and (b) evolution-associated spectra of a single crystal obtained by global fitting to the model discussed in the text.

Time-Resolved Spectroscopy

To understand the excited-state dynamics of **dp-PMI**, femtosecond transient absorption (fsTA) measurements were carried out on **dp-PMI** in DCM solution, single crystals, and polycrystalline thin films. Immediately upon photoexcitation of **dp-PMI** in DCM solution a broad negative absorption change appears from 435-575 nm appears, which is a combination of ground-state bleach (GSB) and stimulated emission (SE) features (**Figure 21**). The excited-state absorption (ESA) features appear simultaneously at 345, 628 and 1085 nm. A slight shift of the GSB, SE and ESA features occurs in $\tau = 1.5 \pm 0.4$ ps, which most likely results from solvation or structural relaxation of the excited singlet state (S_1). The S_1 state then decays to the ground state in $\tau = 5.8 \pm 0.6$ ns as determined from the corresponding nanosecond transient absorption data (**Figure 22**) with no sign of long-lived triplet formation, which is also in accord with the near-unity fluorescence quantum yield of **dp-PMI** in DCM.

Femtosecond transient absorption microscopy (fsTAM)[43] on the **dp-PMI** single crystals was performed using pump polarization parallel to the crystal long axis (**Figure 15**, **Figure 23**, and **Figure 24**). The fsTAM spectra showed no obvious dependence on the probe polarization, so only data for the polarization parallel to both the pump and the crystal short axis (aligned with the transition dipole moment) are presented. In the **dp-PMI** single crystals, strong intermolecular electronic coupling between adjacent **dp-PMI** molecules dramatically changes the photophysics. Upon photoexcitation, a GSB between 540-560 nm appear along with broad ESA features at 550-750 nm. The 670 nm ESA peak decreases substantially over the first 100 ps. Global analysis of the fsTAM data shows four principal spectral components, where the first spectrum is assigned to S_1 decaying through singlet-singlet annihilation due to the high flux of the microscope while the second component is the isolated singlet exciton. The singlet exciton decays in 20.0 ± 0.3 ps to a new state with some intensity at 670 nm but a new feature peaking at 555 nm. This new intermediate decays to a long-lived (>>8 ns) state with the prominent 555 nm feature but no intensity at 670 nm. The long-lived species decays over several microseconds as seen by nanosecond TAM (**Figure 24**) and is thus assigned to the ^{3*}**dp-PMI** state.

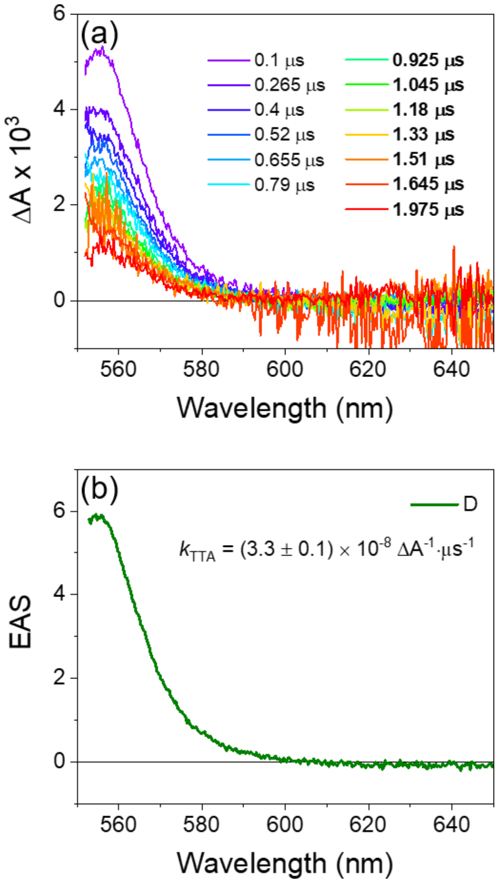

Figure 16. (a) nsTA spectra of **dp-PMI** in a single crystal (ex: 405 nm) at selected pump-probe delay times, and (b) evolution-associated spectra obtained by global fitting to the model discussed in the text.

Global analysis shows that this decay is well fit by a bimolecular $T_1 + T_1$ triplet-triplet annihilation process. The assignment of the long-lived species to the triplet state implies that the intermediate state C exhibits both singlet and triplet character, and so is tentatively assigned to the

^{1}(TT) state. Thus, from the global analysis of the TAM data, singlet fission in the single crystal occurs with $k_{B \rightarrow C}$ = (20 ps)$^{-1}$, and decorrelation of the ^{1}(TT) state to T_1 + T_1 occurs with $k_{B \rightarrow C}$ = (163 ps)$^{-1}$.

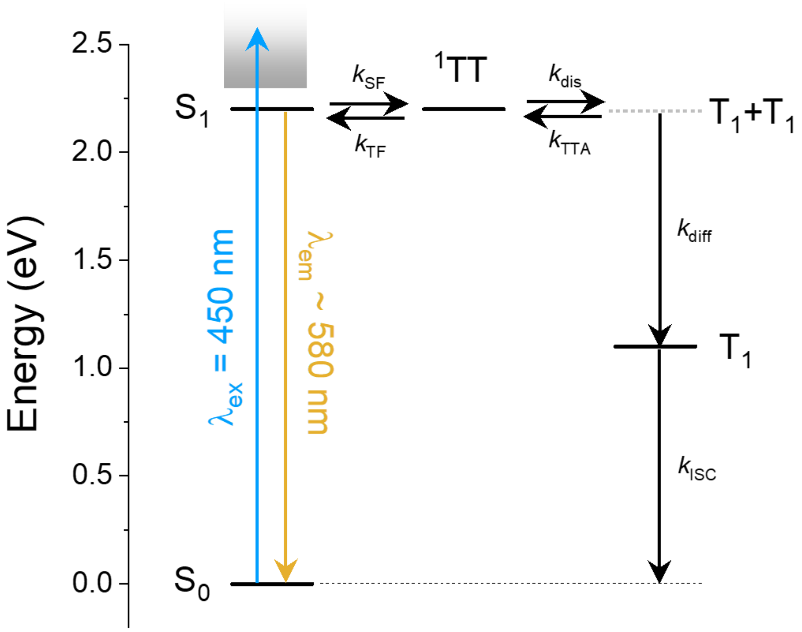

Figure 17. Singlet fission dynamics in **dp-PMI**.

The nature of the intermediate state in the single crystals is further probed by time-resolved fluorescence (TRF) spectroscopy (**Figure 30** and **Figure 31**). The emission decays biphasically over the first few nanoseconds with no obvious spectral changes, and spectra that overall resemble the broadened, redshifted solution-phase fluorescence. The initial singlet fission event is faster than the instrument response (~20-30 ps), however, there is an observable 167 ps emissive process with the same singlet-like spectrum. The time constant for this decay corresponds to the decorrelation of the TT state as observed by fsTAM. The singlet-like emission and the simultaneous appearance of the singlet ($S_n \leftarrow S_1$) and triplet ($T_n \leftarrow T_1$) ESA features in this intermediate suggest that the TT state is in rapid equilibrium with the S_1 state (**Figure 17**), where singlet fission and triplet fusion are both fast and spin-allowed. The long-lived emission with the singlet spectrum following singlet fission is attributed to delayed emission following triplet-triplet annihilation,[33] and indeed the energetics of this system are favorable for this process, as discussed above. In this way, emission originates from repopulation of the S1 state, either through direct triplet fusion from TT, or following triplet-triplet annihilation back to either S_1 or TT.

In order to estimate the yield of **dp-PMI** singlet fission in the solid state, we measure the dynamics in polycrystalline thin films. The transient absorption dynamics in the film (**Figure 25** and **Figure 26**) are remarkably similar to those of the single crystal. Singlet fission occurs in 9.6 ± 0.3 ps, and the ~1 ps process is absent due to the low-fluence conditions of the film TA experiment. The intermediate TT state is also observed, as indicated by the coexistence of features of the initial singlet and terminal triplet spectra; this state decays in 121 ± 6 ps, in good agreement with the intermediate state lifetime observed in the crystal. High-fluence nanosecond TA spectroscopy (**Figure 26**) shows a similar bimolecular decay process. The film TA experiment also allows for confirmation of the assignment of the triplet state through sensitization with a $PdPc(OBu)_8$ (**Figure 27**). Analysis of the triplet spectrum using the singlet-depletion method, giving an estimate of 150 ± 20 %, as calculated with the singlet depletion method (see additional data). This is consistent with the uncertainty of the film thickness (~10%). We note that due to singlet-singlet annihilation losses as a result of the high excitation fluence in the nsTA experiment, this yield should be considered a lower bound (see additional data for details).

In conclusion, we synthesized 2,5-diphenyl-*N*-(2-ethylhexyl)perylene-3,4-dicarboximide (**dp-PMI**) that crystallizes in a slip-stacked geometry in the solid state. Both the polycrystalline thin films and single crystals show ultrafast SF on the sub-ten-picosecond timescale. With one fewer imide group, the **dp-PMI** has less symmetry than PDI, one would expect the quadrupolar interactions normally at play in more symmetric systems to be dominated by the strong dipolar interactions here.

Methods and Additional Data

Synthesis

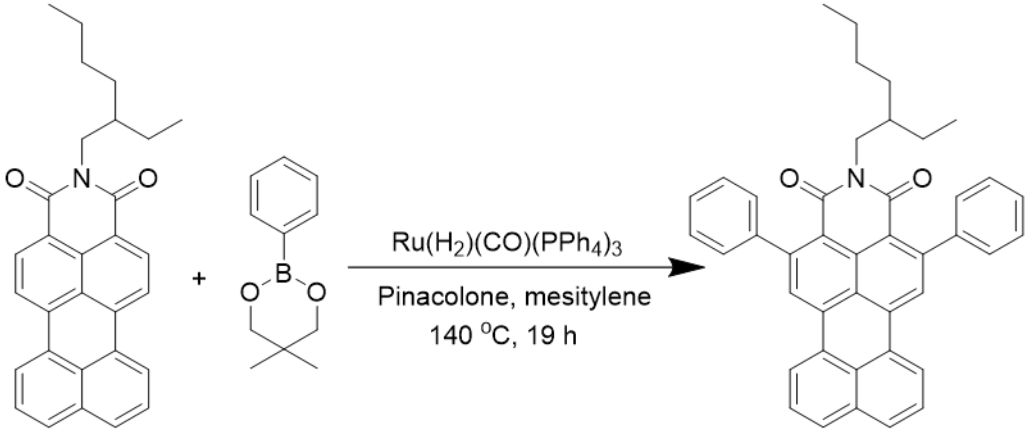

Dp-PMI. N-(2-ethylhexyl)perylene-3,4-dicarboxylic imide (400 mg, 0.92 mmol), 5,5-dimethyl-2-phenyl-1,3,2-dioxaborinane (700 mg, 3.7 mmol), $Ru(H_2)(CO)(PPh_4)_3$ (170 mg, 0.18 mmol) were added into a round-bottom flask. The system was degassed and injected with pinacolone (4.0 mL) and mesityene (4.0 mL). The system was then heated to 140 ^oC for 19 h. The crude product was purified by chromatography with hexanes and dichloromethane, and yielded 250 mg (46%) **dp-PMI**. ^{1}H-NMR ($CDCl_3$): δ 8.40 (d, 2H), 8.24 (s, 2H), 7.89 (d, 2H), 7.59 (t, 2H), 7.52-7.46 (m, 5H), 7.46-7.41 (m, 5H), 3.91 (d, 2H), 1.31-1.17 (m, 9H), 0.81 (dt, 6H). ^{13}C-NMR ($CDCl_3$): δ 163.6, 148.2, 143.3, 135.5, 134.3, 131.8, 130.9, 129.1, 128.3, 128.1, 128.0, 127.6, 127.2, 125.9, 125.1, 123.9, 118.8, 44.0, 37.2, 30.4, 28.6, 23.7, 23.4, 14.3, 10.7. MALDI-TOF (m/z): calcd. for $C_{42}H_{35}NO_2$, 585.27; found, 584.92($[M]^-$)

Profilometry

The thickness of the solid-state thin films was measure on the High Resolution Stylus Profilometer at the Keck-II facility of Northwestern University's NUANCE center. Three samples with three measurements on each sample were performed resulting in an average 100 ± 20 nm film thickness.

X-Ray Diffraction (XRD)

Intensity data of a suitable single crystal of **dp-PMI** were collected at 100.0 K. A suitable single crystal with dimensions of 0.048×0.096×0.655 mm^3 was mounted on a MiTeGen loop with paratone oil on an XtaLAB Synergy diffractometer equipped with a micro-focus sealed X-ray tube PhotonJet (Cu) X-ray source and a Hybrid Pixel Array Detector (HyPix) detector. Temperature of the crystal was controlled with an Oxford Cryosystems low-temperature device. Data reduction was performed with the CrysAlisPro software using an empirical absorption correction. The structure was solved with the ShelXT structure solution program[44] using the Intrinsic Phasing solution method and by using Olex2 as the graphical interface.[45] The model was refined with ShelXL using least squares minimization.[46]

Crystal structure data of **dp-PMI** ($C_{42}H_{35}NO_2$): space group C 2/c (no.15), a = 48.1834(7) Å, b = 4.92160(10) Å, c = 27.1745(6) Å, α = 90°, β = 104.458(2)°, γ = 90°, V = 6240.07 $Å^3$, Z = 4, R-Factor = 5.59%. The final structure has been submitted to the Cambridge Crystallographic Data Centre: CCDC 2213059.

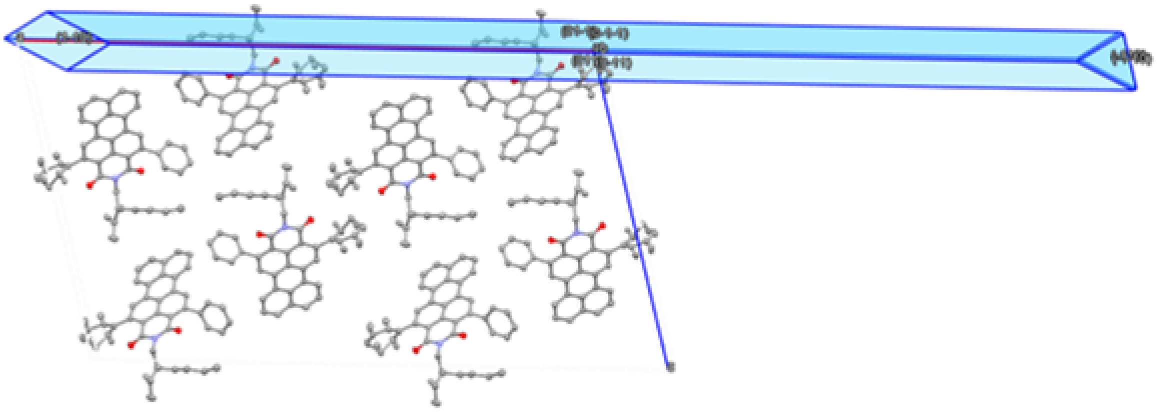

Figure 18. Crystal structure and crystal faces of **dp-PMI**. The long axis of the crystal is parallel to the crystal *a* axis. Two short axes are parallel to the crystal *b*+*c* and *b*-*c* axis, respectively.

Film Preparation

Thin films of **dp-PMI** were spin-coated on the sapphire substrates with injecting 150 µL saturated DCM solution (> 15 mg/mL) at 1200 rpm. Solvent vapor annealing was perform with acetone for 30 min. Triplet sensitized films were spin-coated on the glass substrates with DCM solution of **dp-PMI** and PdPc(OBu)$_8$ (10:1 weight ratio) at a concentration of 10 mg/mL. Spin-coating and annealing conditions of the sensitized films were the same as the neat films.

Steady-State Spectroscopy

Steady-state absorption and fluorescence spectra were collected on the same instruments described in Chapter 1.

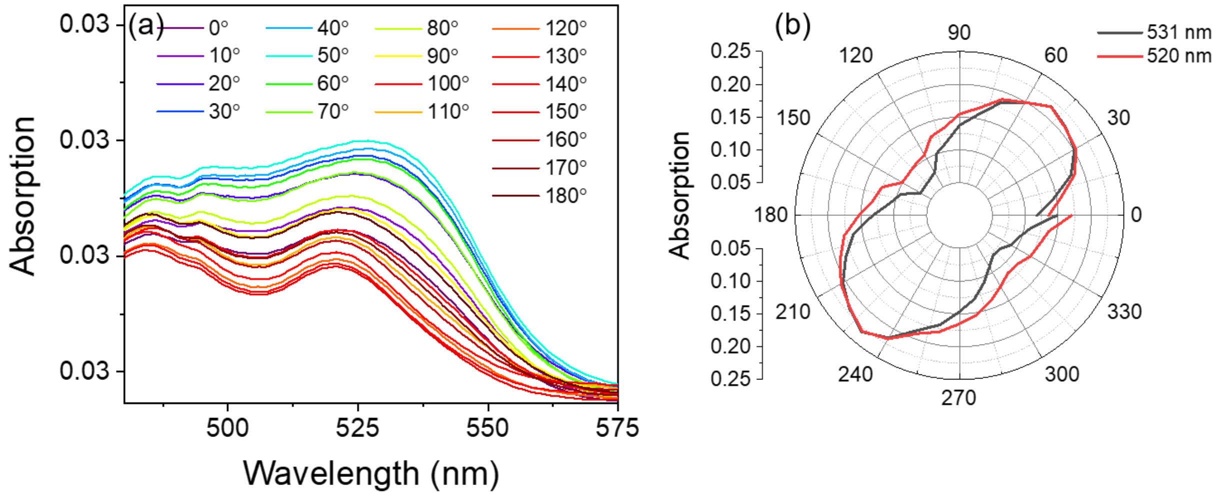

Figure 19. Polarization-dependent absorption spectra of the **dp-PMI** single crystal.

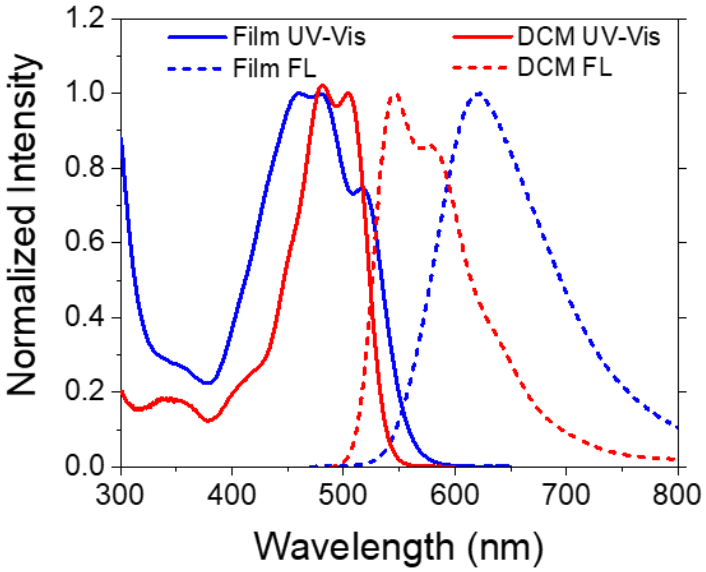

Figure 20. Normalized absorption (solid lines) and emission (dashed lines) spectra of **dp-PMI** in thin films (blue) and DCM solution (red).

The absorption spectrum of **dp-PMI** in the thin film experiences a red-shifting of the 0-0 absorption band from 504 nm in DCM solution to 517 nm in the film as well as significant broadening. The emission spectrum in DCM shows distinct 0-0 and 0-1 bands at 547 and 579 nm, while the spectrum of the thin film shows a broad, featureless, red-shifted emission at 621 nm. The fluorescence of the thin film is strongly quenched ($\phi_F < 0.005$) compared to the near-unity quantum yield in DCM ($\phi_F = 0.99 \pm 0.01$).

Solution-Phase TA Data

High-fluence femtosecond transient absorption (fsTA) spectroscopy and nanosecond transient absorption (nsTA) spectroscopy were performed on the same system described in Chapter 1.[30] Pump pulses at 480 nm and 740 nm (1 μJ/pulse) were generated by a commercial collinear optical parametric amplifier (TOPAS-Prime, Light-Conversion, LLC). Low-fluence fsTA measurements were performed using a regeneratively amplified Yb:KGW laser system (Spirit One, Spectra-Physics, Inc.) operating at 100 kHz pumping a collinear optical parametric amplifier (Spirit-OPA-8, Light-Conversion, LLC). The 960 nm OPA output was frequency-doubled in an β-barium borate crystal to generate 1-20 nJ, 480 nm pulses of ~180 fs duration. The probe was generated and the spectra were recorded using methods previously described.[31] FsTAM were performed on a commercial amplified system (Spirit One, Spectra-Physics, Inc.) described in detail previously.[43] The white light continuum was generated by focusing the 1040 nm fundamental (100 kHz) to an yttrium aluminum garnet (YAG) crystal. The visible pump pulses were modulated at 50 kHz with an electro-optic amplitude modulator (EOAM-NR-C4, Thorlabs). Solution samples were measured in 1 mm quartz cuvettes and were freeze-pump-thawed for three cycles before each measurement. Thin film samples were measure under vacuum condition. Single crystal samples were measure under the N_2 flow. All time-resolved measurements were carried out at room temperature. Details of the kinetic fitting procedure have been described previously.[32]

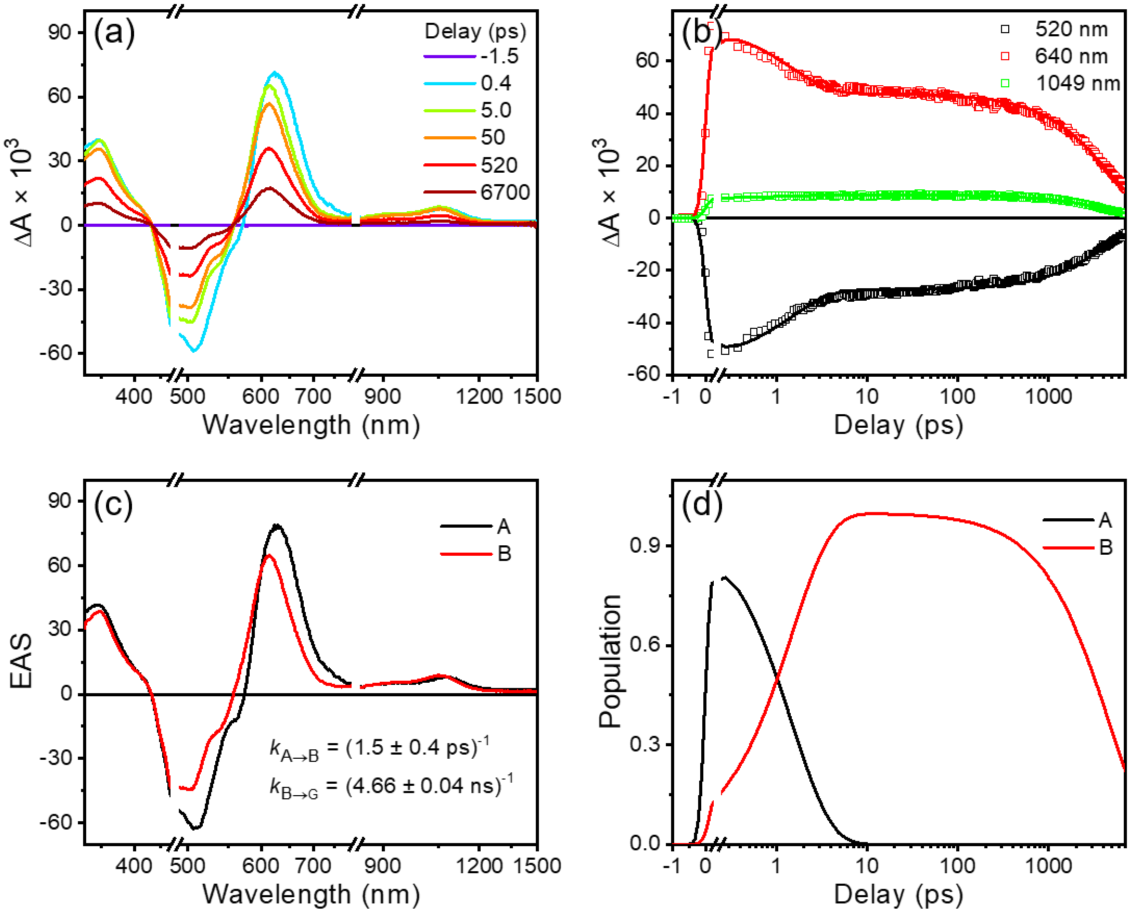

Figure 21. FsTA spectra (ex: 480 nm, 1.0 μJ/pulse) of **dp-PMI** in DCM (a) TA spectra at selected delay times. (b) Kinetic traces at selected wavelengths. (c) Evolution-associated spectra obtained by wavelength global fitting to a A → B → Ground state kinetic model. (d) Population distribution of the kinetic model.

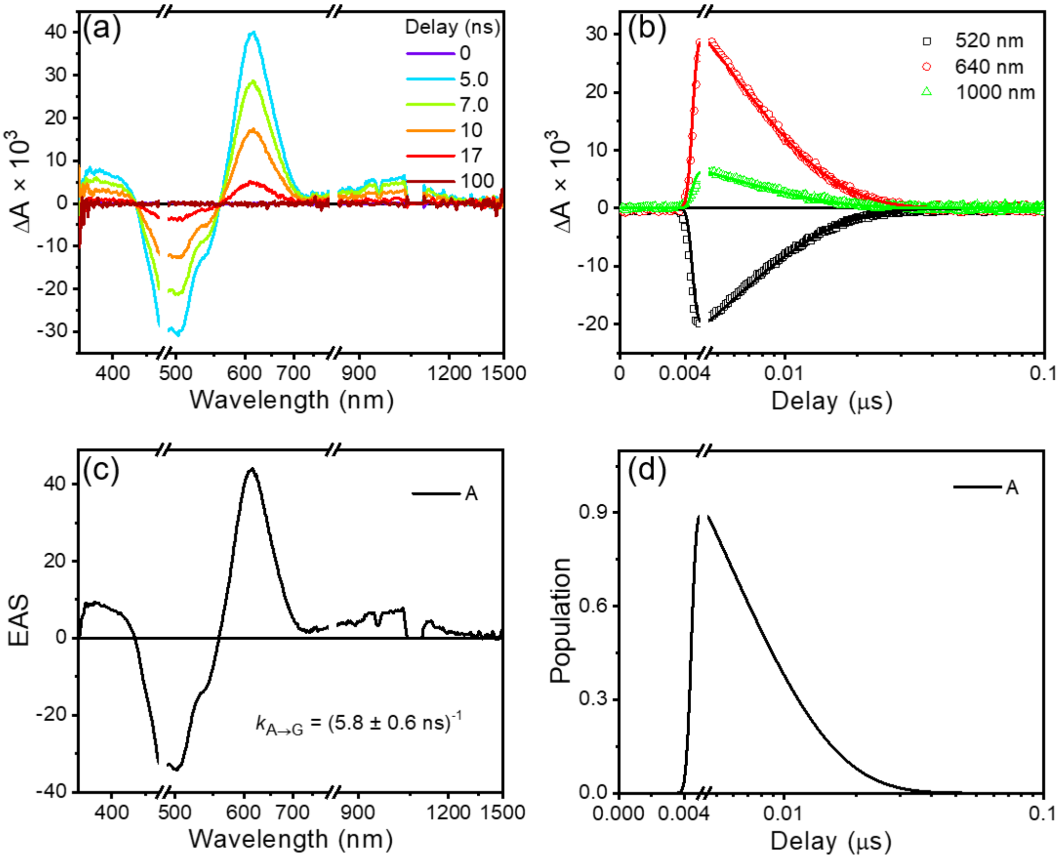

Figure 22. NsTA spectra (ex: 480 nm, 1.0 μJ/pulse) of **dp-PMI** in DCM (a) TA spectra at selected delay times. (b) Kinetic traces at selected wavelengths. (c) Evolution-associated spectra obtained by wavelength global fitting to a A → Ground state kinetic model. (d) Population distribution of the kinetic model.

Single-Crystal TAM Data

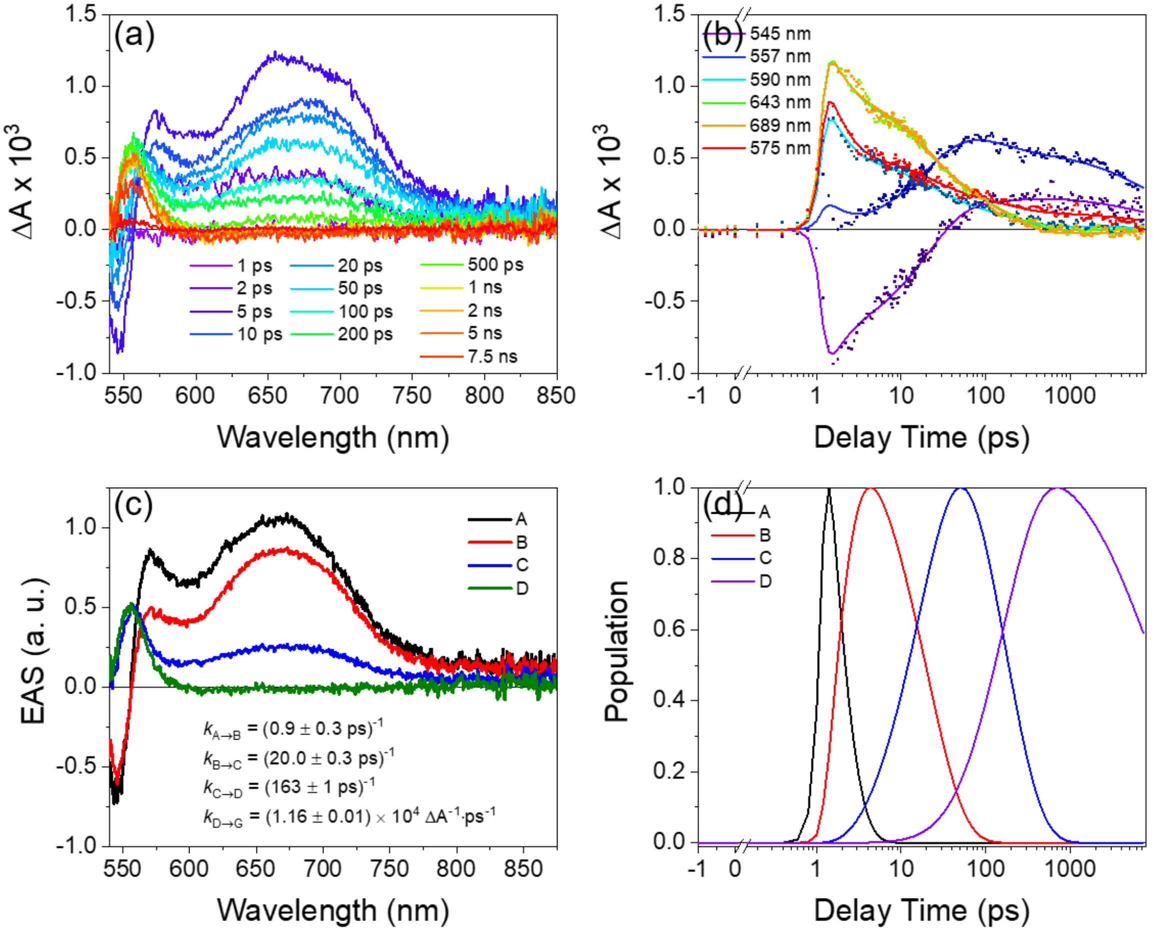

Figure 23. (a) FsTAM spectra of a **dp-PMI** crystal (ex: 450 nm, 1.0 μJ/pulse). (b) Selected wavelengths and kinetic fits from global analysis. (c) Evolution-associated spectra and time constant. (d) Population curves of kinetic states.

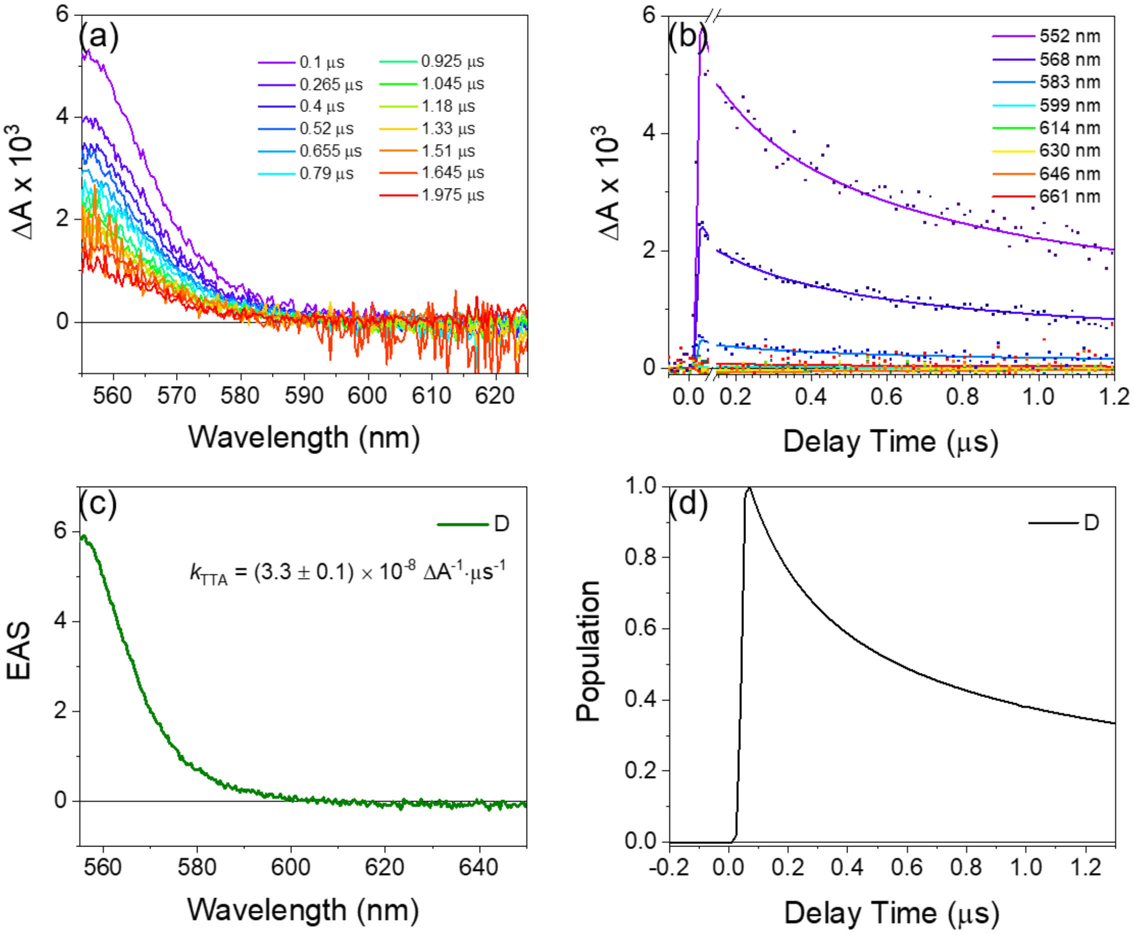

Figure 24. (a) NsTAM spectra of a **dp-PMI** crystal excited at 450 nm. (b) Selected wavelengths and kinetic fits from global analysis. (c) Evolution-associated spectra and time constant. (d) Population curves of kinetic states.

Thin Film TA data

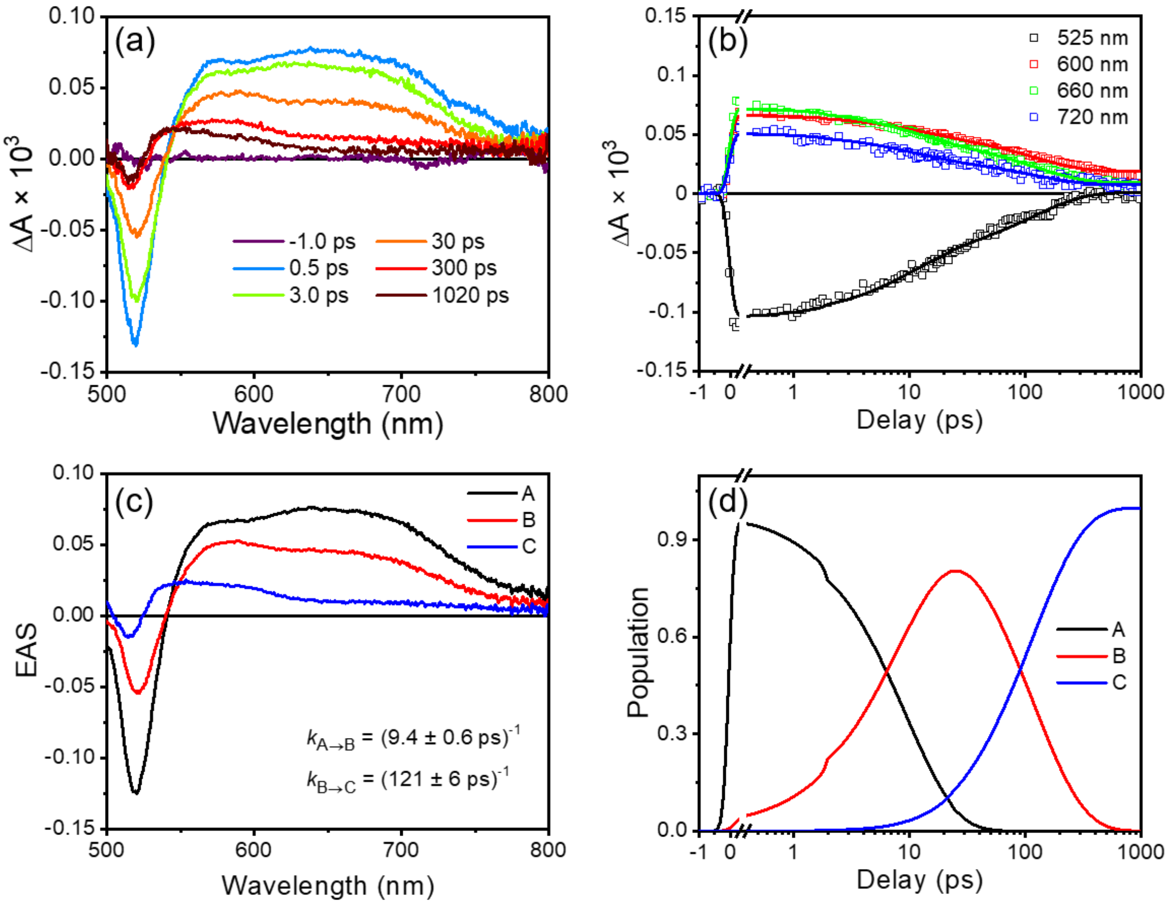

Figure 25. (a) FsTA spectra of a **dp-PMI** thin film (ex: 450 nm, 6.9 nJ/pulse). (b) Selected wavelengths and kinetic fits from global analysis. (c) Evolution-associated spectra obtained by wavelength global fitting to a A → B → C kinetic model. (d) Population distribution of the kinetic model.

Using global fitting to a sequential A → B → C model, we observe that SF occurs in 9.4 ± 0.6 ps. The intermediate state is assigned to the ^{1}(TT) because it has similar spectrum to the terminal, isolated triplet (T_1) observed by nsTA experiments,[27] and the similarity to the intermediate spectrum observed in the single crystal. Similar to the single crystal, the ^{1}(TT) state decays in τ = 121 ± 6 ps two independent triplet states. The final triplet exciton population decays primarily by rapid bimolecular triplet-triplet annihilation (TTA) on the nanosecond timescale as probed with nanosecond transient spectroscopy.

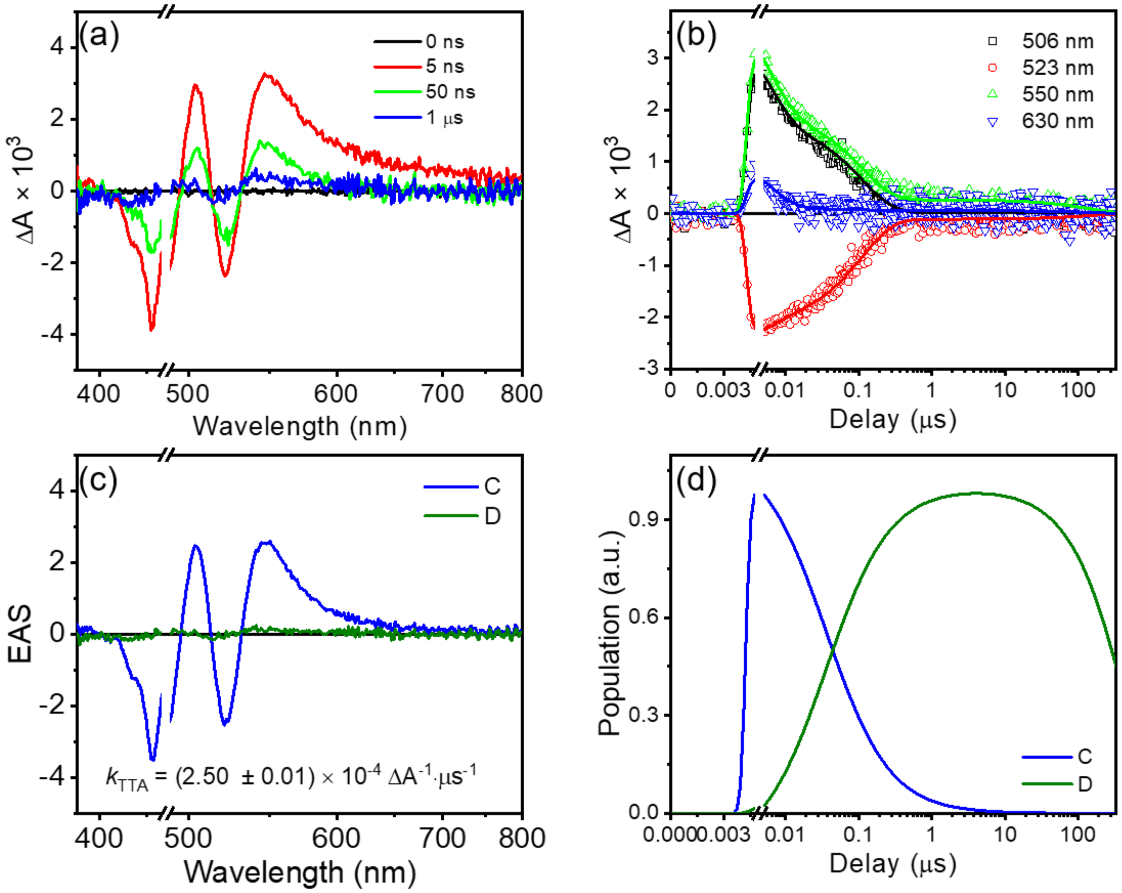

Figure 26. (a) NsTA spectra of a **dp-PMI** thin film (ex: 480 nm, 1 μJ/pulse). (b) Selected wavelengths and kinetic fits from global analysis. (c) Evolution-associated spectra obtained by wavelength global fitting to a bimolecular triplet-triplet annihilation decay. (d) Population distribution of the kinetic model.

Sensitized Film Data

The triplet spectrum of the **dp-PMI** was measured using a sensitized film with PdPc(OBu)$_8$ (E_T = 1.24 eV) [47-48] and selectively excited the sensitizer at 740 nm. The nsTA spectra at between 0-100 ns of the sensitized film were averaged to get the triplet spectrum. The spectrum was then normalized and compared to the EAS of the longest-lived state for the neat film in the nsTA data. Since the sensitized triplet spectrum of **dp-PMI** strongly resembles the EAS for the final, long-lived state extracted from the nsTA data, we assign this last state as the **dp-PMI** triplet state.

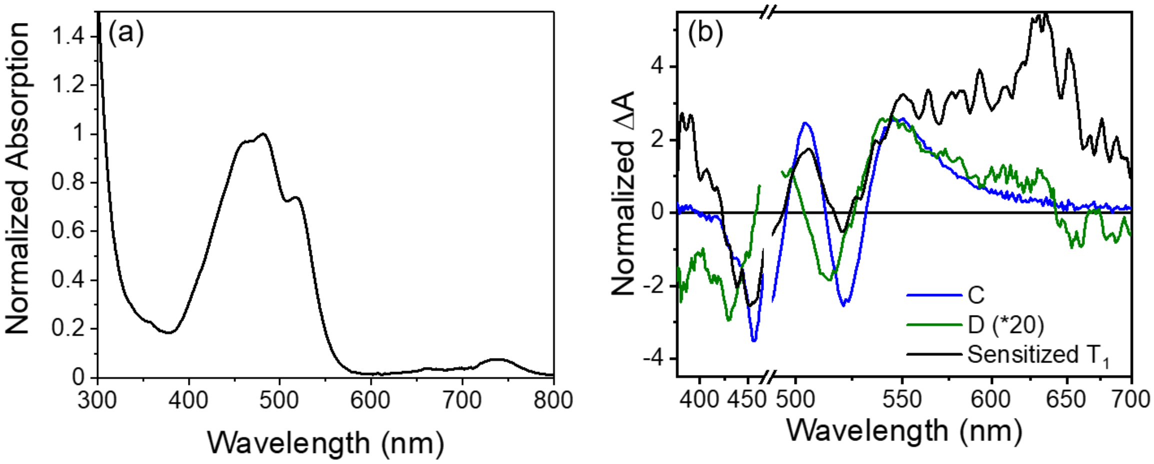

Figure 27. (a) Steady-state absorption of the PdPc(OBu)$_8$-sensitized **dp-PMI** film. b) Triplet spectrum obtained from exciting the sensitized film at 740 nm (red) overlaid with species C and D from the nsTA data of the thin film (blue) shown in **Figure 26**. Some residual PdPc(OBu)$_8$ triplet is observed at 650 nm.

Temperature-Dependent Differential Absorption Spectra

Temperature-dependent absorption measurements were also performed on the **dp-PMI** films to probe the effects of increased thermal energy deposited into the film following photoexcitation. We compare the thermal differential absorption spectrum (subtracting the absorption spectrum at 25 °C from 65 °C and the EAS of the triplet normalized at the ESA peak at 550 nm. Though the peak positions of the absorptive and emissive features are similar, the relative ratio of the features differ substantially from those in the EAS and thermal difference spectrum. Additionally, the TA data show a bleach in the 400-480 nm region that is not present in the thermal difference spectra. We conclude that while thermal effects may still be present in the solid-state due to the high pump fluences, the long-lived feature does not fully originate from the thermal distortion of the absorption spectrum, but rather is due to a long-lived triplet state.

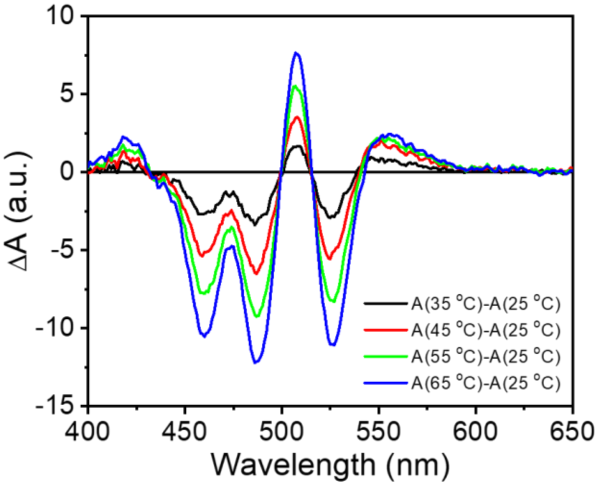

Figure 28. Thermal difference absorption spectra by subtracting the spectrum at 25 °C and at elevated temperatures.

Triplet Yield Calculation

Triplet yield calculation is using the singlet depletion method as described previously.[49] The excitation density (ξ) is calculated based on the excitation pulse energy (E), wavelength (λ), absorption (A) at 480 nm, spot size (a), and the film thickness (l), using the following equation:

Equation 3

$$\xi = \frac{E \cdot \lambda \cdot K \cdot (1 - 10^{-A})}{l \cdot a}$$

where K is a composite of physical constants, $5.034 \cdot 10^{15}$ J^{-1} nm^{-1}. [49] The pulse energy is 1.0 μJ/pulse, and the absorption at 480 nm is 0.35. The film thickness is (100 $\pm$ 10) nm, and the spot size of pump is 1.0 mm^2. The excitation density ξ is calculated to be $1.3 \cdot 10^{19}$ cm^{-3}.

The scaling factor ε gives the expected ground-state absorption spectrum that produces expected bleach at 0 ns delay, which is calculated based on excitation density (ξ), the unit cell volume (V), and the number of molecules per unit cell (Z) using the following equation:

Equation 4

$$\varepsilon = \frac{\xi \cdot V}{Z}$$

where ξ has been calculated above, V =6240 $Å^3$, and $Z = 4$. The scaling factor ε is calculated to be $2.0 \cdot 10^{-2}$. The remaining portion p_T of the excitons after the singlet-singlet annihilation (SSA) is estimated by the population of the last state which is 0.35. Thus, the expected ground state bleach at 480 nm (A_{exp}) can be calculated using the following equation:

Equation 5

$$A_{\mathrm{exp}} = \varepsilon \cdot p_{\mathrm{T}} \cdot A$$

The expected ground state bleach at 480 nm (A_{exp}) is calculated to be $2.5 \cdot 10^{-3}$. The expected ground state bleach spectrum is then obtained by scaling the absorption spectrum to $\Delta A = 2.5 \cdot 10^{-}$

^{3} at 480 nm. We then subtract this expected ground state bleach from the nsTA spectrum at 5 ns to recover the undistorted triplet spectrum with no negative features, which is shown in **Figure 29**. A ratio of 1.5 is used to get the undistorted spectrum, thus, the triplet yield at 5 ns is 1.5. At 5 ns, the triplet barely decays while the (TT) state almost completely decays, thus, the triplet yield at time zero is estimated to be the same as it at 5 ns. An error of 0.2 is estimated by the uncertainties of the measurements and the error propagation of the calculation. We note that the thermal distortion of the spectrum will increase the Δ*A* of the spectrum which makes the calculated triplet yield higher than actual. The calculated triplet yield should be the lower bound of the actual triplet yield.

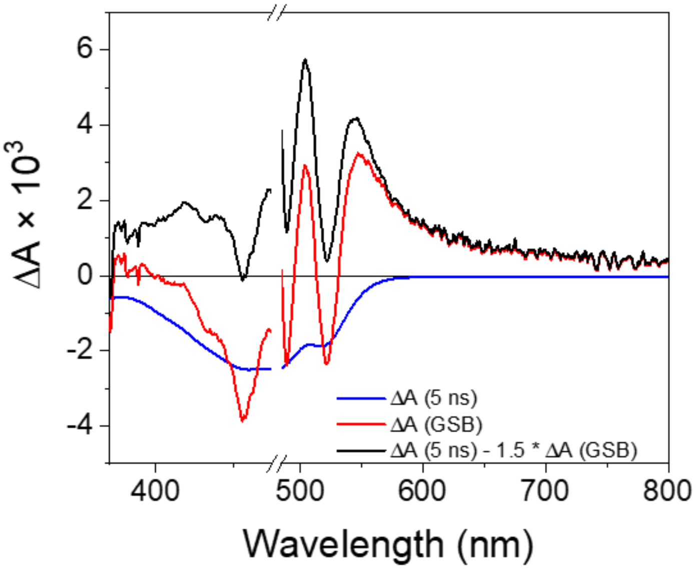

Figure 29. Comparison of the expected ground state bleach spectrum (red), nsTA spectrum at 50 ns (blue), and the calculated undistorted triplet spectrum (black)

Single-Crystal TRF Microscopy Data

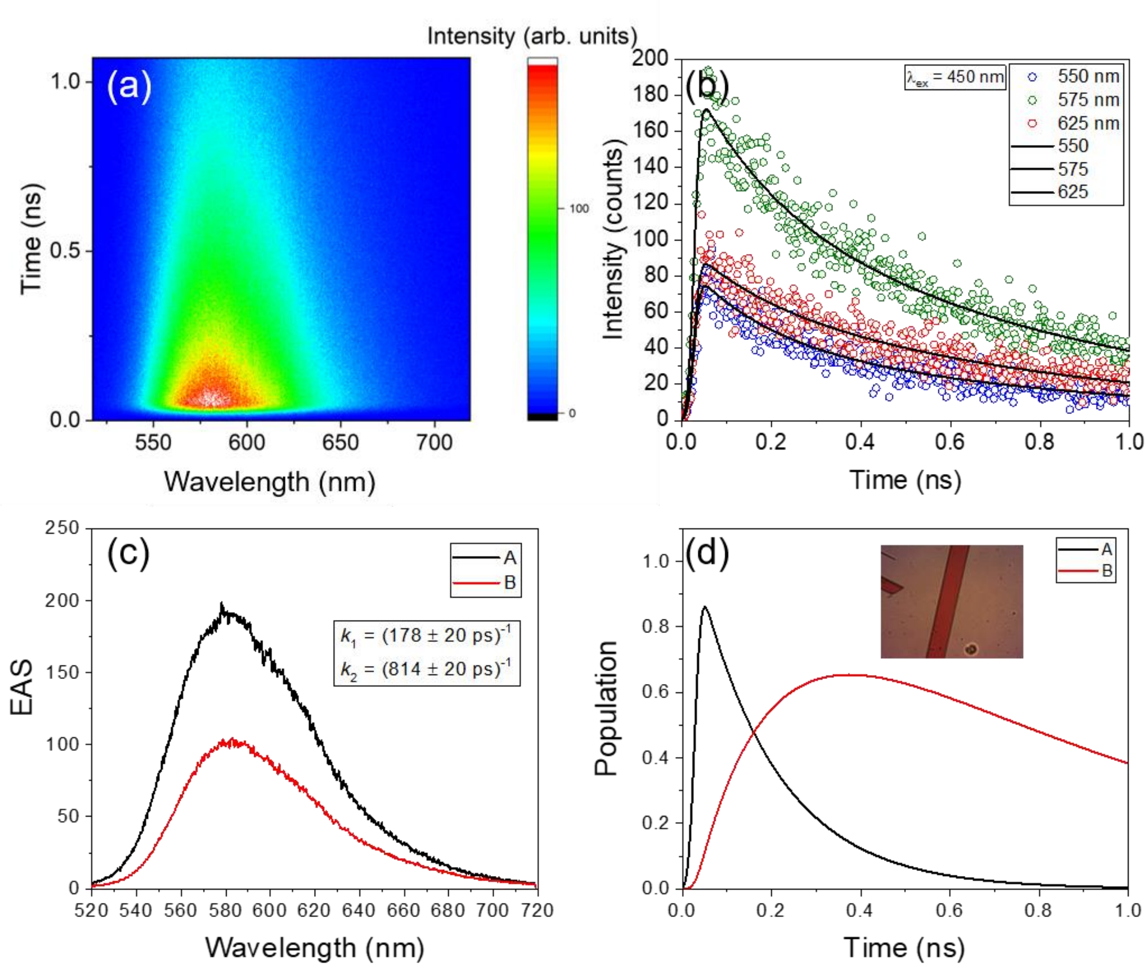

Figure 30. (a) TRF spectra of a **dp-PMI** crystal excited at 450 nm over a 1 ns window. (b) Selected wavelengths and kinetic fits from global analysis. (c) Evolution-associated spectra and time constants. Inset: micrograph of crystal. (d) Population curves of kinetic states.

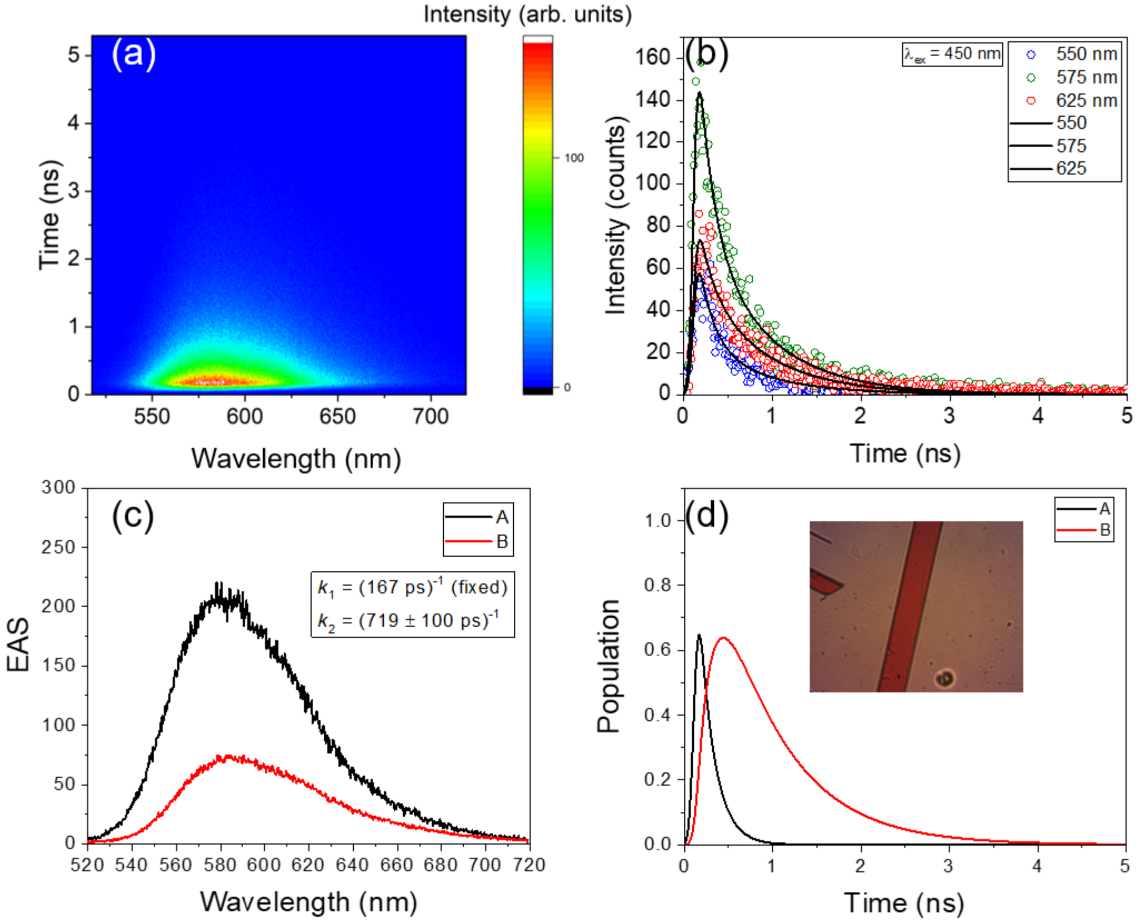

Figure 31. (a) TRF spectra of a **dp-PMI** crystal excited at 450 nm over a 5 ns window. (b) Selected wavelengths and kinetic fits from global analysis. (c) Evolution-associated spectra and time constants. (d) Population curves of kinetic states. Inset: micrograph of crystal.

Chapter 4. Accelerating Symmetry-Breaking Charge Separation in a Perylenediimide Trimer through a Vibronically Coherent Dimer Intermediate

Photoinduced symmetry-breaking charge separation (SB-CS)[50-52] occurs in systems ranging from the chlorophyll special pair in photosynthetic reaction center proteins[53-54] to organic photovoltaics.[55-56] It is thus important to understand the fundamental mechanism of SB-CS as well as other competing relaxation pathways in chromophore oligomers, such as excimer formation and singlet fission (SF), to design functional organic materials for photonic applications. The 'oligomer approach' employs molecular π stacks that mimic these systems using a small number of constituent units and has been successful for understanding structure–property relationships in discrete, well-defined constructs.[16, 57-59] Among the various chromophores studied with this approach, perylenediimide (PDI) has been one of the most actively investigated because of its robustness, tunable absorption spectrum range, appreciable extinction coefficients[39] and propensity for strong π–π interactions.

In recent years, the molecular exciton theory developed by Kasha and Davydov[60-61] has been advanced by Spano and colleagues[62-63] to emphasize the vital role of short-range charge-transfer (CT)-mediated coupling in molecular aggregates.[64-66] This short-range coupling is very sensitive to the molecular packing geometry, such that sub-ångstrom displacements along the molecular long or short axis can impact the coupling strength. Thus, various photophysical pathways[67] such as excimer formation[58, 68-75], SB-CS[76-79] or even SF[80-83] may be promoted or suppressed depending on the molecular packing geometry, along with the relative energies of the Frenkel excitons (FEs), CT states and correlated triplet pair states.

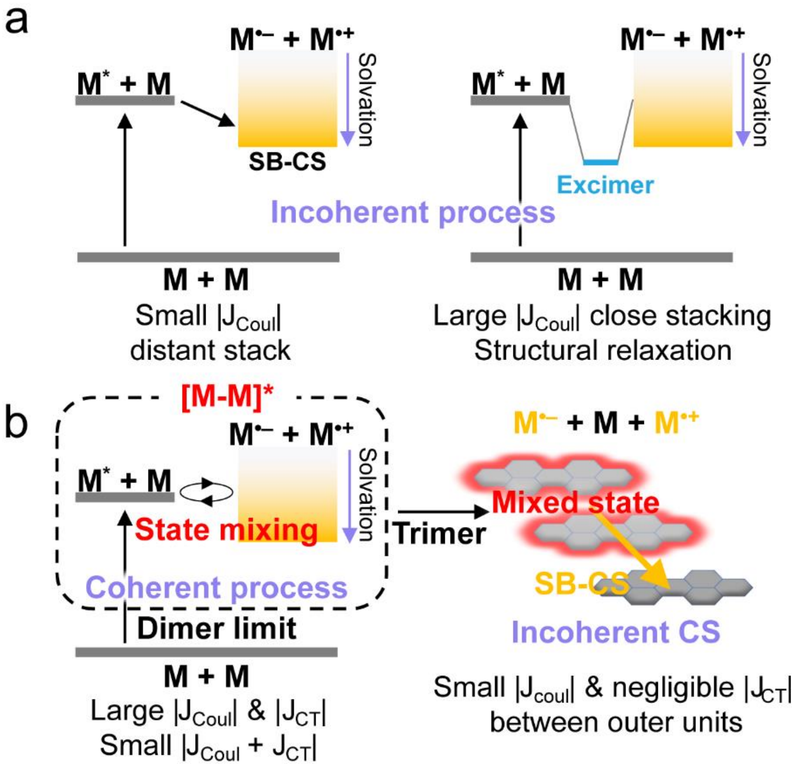

Figure 32. Representative photoinduced dynamics of PDI stacks. a, Typical SB-CS process (left) and excimer formation (right). b, Mixed FE/CT state formation, which further evolves to the SB-CS state between the outer PDI units in trimer case.

Accordingly, as shown in **Figure 32**, we allocate the photoinduced dynamics of PDI dimer stacks into three categories in terms of the long-range Coulombic and short-range CT coupling interactions (**Figure 32a,b**): (1) when the Coulombic coupling is small (longer interchromophore distance), the chromophores relax to the SB-CS state by an incoherent charge separation process;[79] (2) when the Coulombic coupling is strong (shorter interchromophore distance), structural relaxation can lead to the excimer state,[73, 84-85] which can act as an energy trap; (3) when both coupling strengths cancel, the chromophore stack lies in the so-called ‘null-type’ regime, because the overall electronic coupling strength is approximately zero. In the latter case, vibronic coupling may lead to electronic state mixing between the FE and CT states,[83, 86-87] although a null-type interchromophoric geometry is not a necessary condition for state mixing when the vibronic coupling is strong. In **Figure 32c** we depict these cases in the coupling plane, including previous works on π-stacked PDIs. We assume that sufficient solvation takes place and exclude the SF channel and linear PDI assemblies for simplicity. Under these restrictions, there are four dimers composed of the same PDI unit but having different geometries compared to this work. One dimer possesses an interchromophore distance of 3.5 Å and forms an excimer state upon excitation,[73] whereas the other three dimers have distances of 6.4–10.8 Å, with little orbital overlap, and undergo SB-CS.[79] It should be noted that we explicitly neglect through-bond interactions in this comparison, which should be negligible when the number of bonds in the linker is large, as is the case in this study, although they can result in SB-CS at intermediate interchromophore distances, where direct coupling through the chromophore π orbitals is weak.[79]

In this work we report the synthesis and characterization of a null-type PDI dimer (**2**) and trimer (**3**) to explore the role of vibronic coupling in coherent SB-CS. Using complementary electronic transient absorption (TA) and time-resolved infrared and vibrational coherence (VC) spectroscopies, in dimer **2** we observe rapid mixed-state formation between the adjacent PDI units in 200 fs by vibronic coupling along the high-frequency coordinates, whereas incoherent SB-CS takes place in PDI trimer **3** via electron or hole transfer from the initial coherent FE/CT mixed state to the additional distal PDI within 2–3 ps. This incoherent SB-CS is accelerated by the interchromophore low-frequency vibrations that collapse the mixed state. Because this ultrafast SB-CS process in **3** is three orders of magnitude faster than in a dimer of similar chromophore separation,[79] our findings provide fundamental insights into the efficient SB-CS enabled by the intermediate mixed electronic state. Additionally, we demonstrate that interactions between a coherently mixed dimer electronic state and a third PDI chromophore lead to rapid dephasing of the PDI dimer mixed state, which can have considerable implications for utilizing vibronic coherence in solid-state applications.

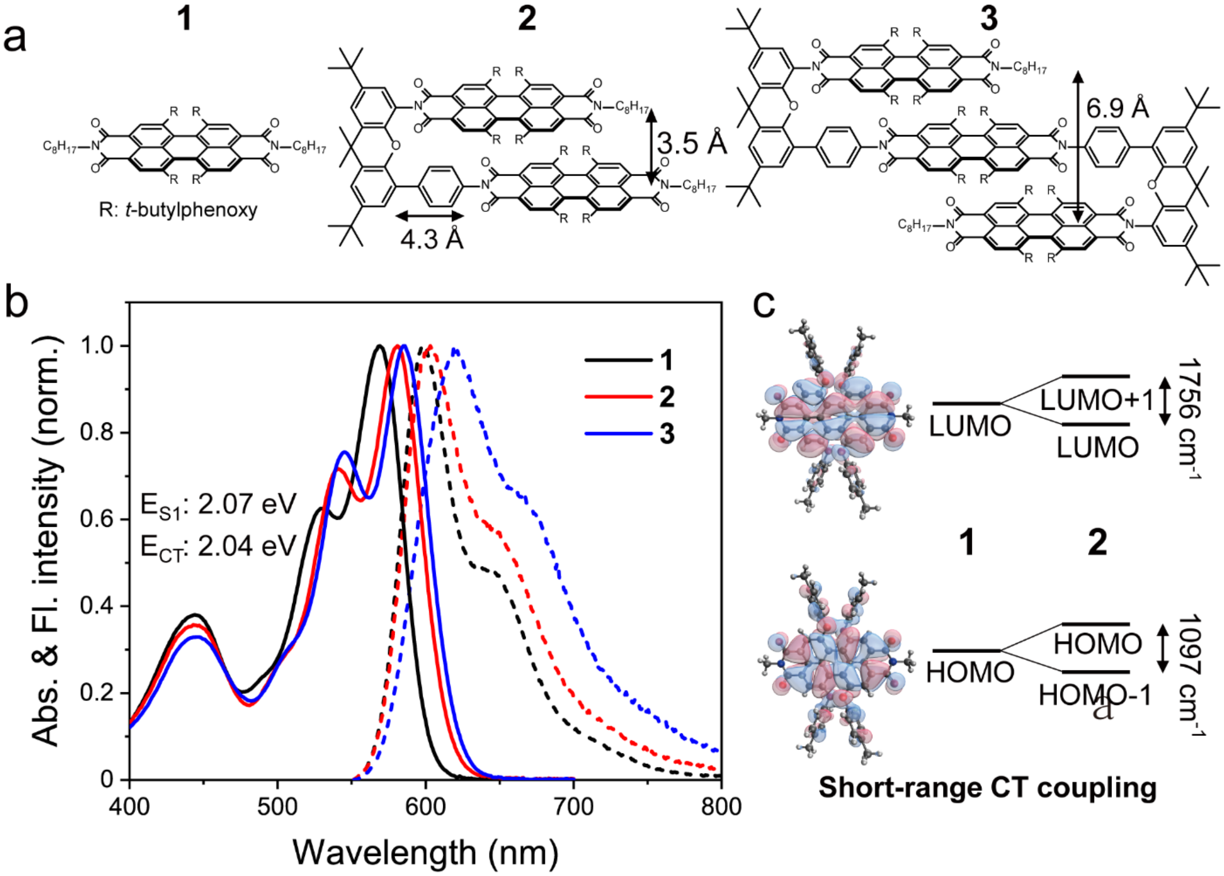

Figure 33. a, Molecular structures of monomer (**1**), dimer (**2**), and trimer (**3**) where R is a 4’-*t*-butylphenoxy group and where rotation angles between neighboring chromophores are ca. 15 degree. **b,** Steady-state absorption and fluorescence spectra of **1**, **2**, and **3** in THF. c, Energy level splitting between HOMOs and LUMOs in **2** due to the short-range CT coupling. E_{S1} and E_{CT} of **2** are denoted in (b).

Results and Discussion

Synthesis and Molecular Structures

The molecular structures of **1**, **2** and **3** are shown in **Figure 33a**, with **2** and **3** synthesized by condensing the corresponding 1,6,7,12-tetrakis(4′-tert-butylphenoxy) perylene(3,4:9,10)bis(dicarboxydianhydride) or the corresponding monoimide-monoanhydride with the xanthene spacer (**Figure 38**). The PDI units are slipped by 4.3 Å along their long molecular axes and stacked with an average distance of 3.5 Å in both 2 and 3 (based on density functional theory (DFT) optimization; see additional data for details). The π–π stacking distances of 2 and 3 are 3.5 Å and 6.9 Å, respectively, and the center-to-center PDI–PDI distance is 5.8 Å in **2** and the center-to-center distance between the two outer PDIs in **3** is 11.7 Å. Multi-dimensional NMR spectra (**Figure 55-67**) show the interchromophore proton correlations, which further support the stacked structures of **2** and **3**. Detailed analyses are provided in additional section.

Steady-State Spectroscopy and Electronic Coupling Strength

The UV–vis absorption spectra of **1**, **2** and **3** in THF are shown in **Figure 33b**. The absorption maxima of **1**, **2** and **3** appear at 569, 581 and 585 nm, respectively. The redshifted 0–0 bands in **2** and **3** are consistent with the increased Coulombic coupling in J-type aggregates. Compared to **1**, both **2** and **3** show a slight increase in their I_{0-1}/I_{0-0} vibronic band ratios, which comes from weak H-type electronic interactions between PDI units. These increased ratios in **2** and **3** are small compared to those in cofacial H-type dimers showing inversion of the vibronic band ratio, which have competitive relaxation pathways between SB-CS and excimer formation.[77] The vibronic band ratio reports on the electronic coupling strength (J), which is described as the sum of long-range Coulombic (J_{Coul}) and short-range CT couplings (J_{CT}). Using the absorption spectra of **2** and **3**, and following the method developed in ref.,[88] the calculated values of J are 15 and 46 cm^{-1} for **2** and **3**, respectively.[4] Although estimating the couplings (J_{Coul} and J_{CT}) in the perturbative limit may be inaccurate when FE and CT states are not well separated,[65] the cancellation of these values is also evident in **2**.[4] This results from the presence of considerable opposite short-range CT coupling due to the substantial highest occupied molecular orbital-highest occupied molecular orbital (HOMO-HOMO) (lowest unoccupied molecular orbital-lowest unoccupied molecular orbital (LUMO-LUMO)) orbital overlap of **2**, which splits the MO levels (ΔHOMOs of 1,097 cm^{-1} and ΔLUMOs of 1,756 cm^{-1}),[4] in keeping with differential pulse voltammetry measurements (**Figure 33c** and **Figure 54**). Owing to the small electronic coupling strengths ($|J| < 100\ \mathrm{cm}^{-1}$) of **2** and **3**, they are classified as null-type aggregates.[89-90] As a result, the fluorescence spectra of **2** and **3** show monomeric shapes rather than the broadened excimer emission observed in cofacial PDI oligomers.[58, 77] The substantial quenching of the fluorescence quantum yields observed for **2** and **3** in THF (both 0.015 ± 0.005) relative to **1** (0.90 ± 0.01) indicates the presence of rapid non-radiative deactivation processes. However, in toluene (Tol), the quantum yields of **2** (0.35 ± 0.01) and **3** (0.39 ± 0.01) remain at an intermediate level, indicating that these non-radiative processes depend on the solvent polarity (

Table 3). Additional steady-state data are shown in **Figure 39**.

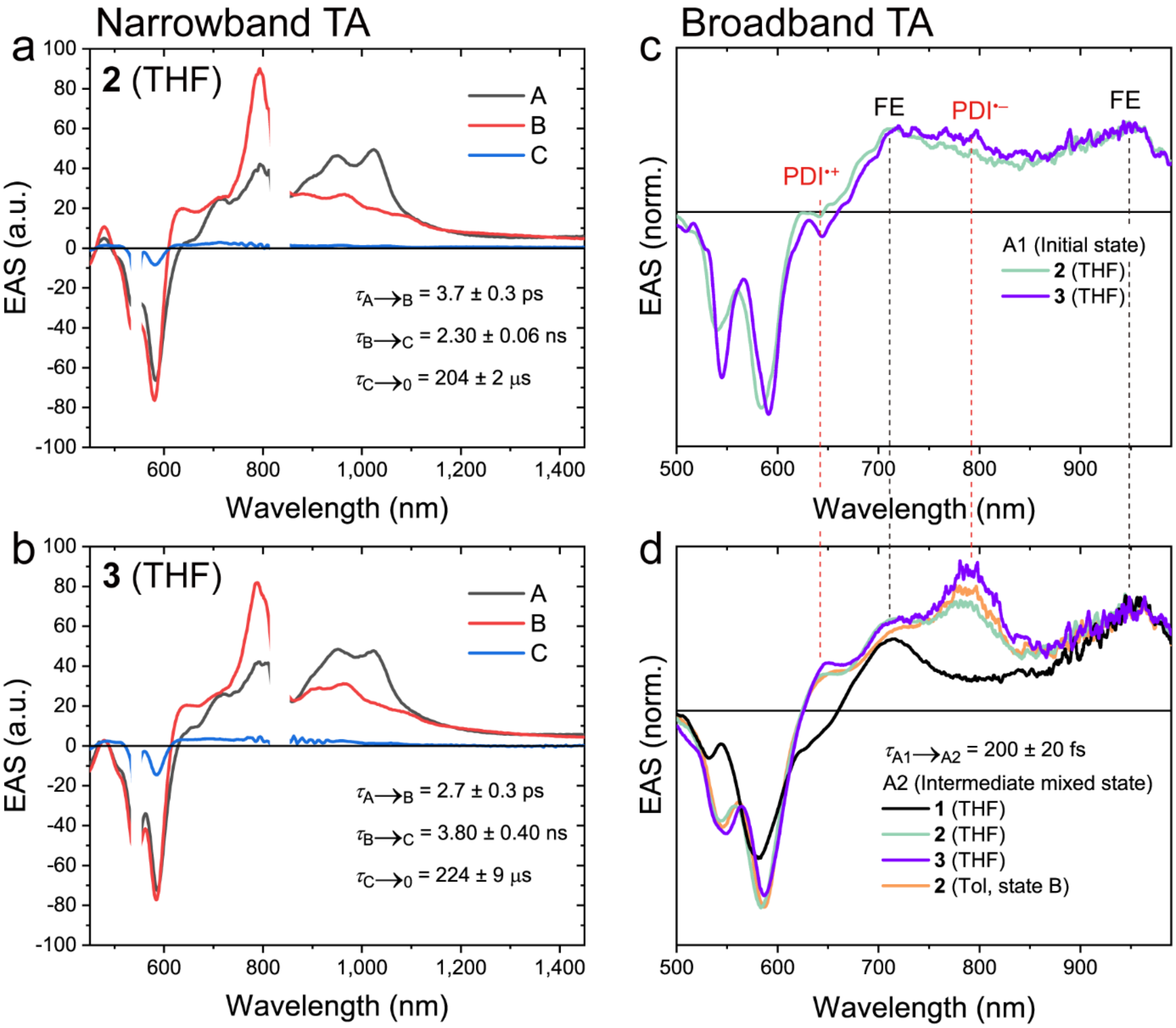

Figure 34. TA spectra (narrow and broadband excitation) and analysis. **a-b,** Evolution-associated spectra (EAS) from narrowband TA measurements (**a**) **2** and (**b**) **3**. **c-d**, EAS spectra before reaching state B (in narrow band measurements) obtained by broadband TA measurements (**c**) the initial state and (**d**) the intermediate mixed state. Dashed lines indicate FE (black) and charged-species (red) bands. Note that A2 state of **2** and **3** show both FE and CT character.

TA Spectroscopy

We performed TA spectroscopy to understand the general excited-state dynamics in three different temporal ranges. The TA spectra of **2** and **3** in THF, acquired on a narrowband femtosecond-excitation TA instrument (instrument response function (IRF) = 350 fs), are shown in **Figure 34a,b**. The evolution-associated spectra (EAS) were obtained by global fitting to an A → B → C → ground state model, where the last lifetime was determined from the nanosecond TA data (**Figure 45** and **Figure 51**). The sub-picosecond regime was studied using broadband-excitation TA measurements (IRF = 20 fs), with the 20-fs output of a noncollinear optical parametric amplifier used as the pump. Following broadband photoexcitation, the initial TA spectra of **2** and **3** in THF show dominant contributions from the FE state (710 and 950 nm), ground-state bleach (GSB, 581 nm) and a slight contribution from the CT state (636 and 793 nm) (**Figure 34c**), where the FE band was assigned by matching the EAS spectra of **1** and the CT band observed in previous studies.[79, 91] The CT character of this mixed state arises in 200 ± 20 fs and results in an intermediate state (**Figure 34d**). Note that both the initial and intermediate states contribute to state A in narrowband-excitation TA measurements; for this reason, we label the broadband EAS as states A1 and A2, respectively. The dynamics and spectra of **2** and **3** in Tol are also similar at this timescale, having 200-fs components with increasing CT character, and the fast dynamics appear regardless of the solvent polarity. Because Frenkel exciton delocalization across more than three units is known in PDI stacks,[72, 89] the similarity of the mixed-state formation times and spectra for the dimer and trimer suggests that **3** rapidly localizes into a mixed state of two adjacent units, as the outer units have negligible CT coupling. Subsequently, the intermediate states further evolve to state B (**Figure 34a,b**) with more CT and less FE character, with time constants of 2–3 ps, whereas **2** still has more FE character than **3**. Notably, the lifetimes of state B are different in **2** (2.30 ± 0.06 ns) and **3** (3.8 ± 0.4 ns), indicating that adding a third chromophore alters the nature of this state, even though the TA spectra remain similar. State B decays to triplet excitons (state C) that live for ~200 μs (**Figure 45**). In Tol, after state B is generated in 6–7 ps, we observe ~100-ps components for **2** and **3**, which we assign to slow structural relaxation (**Figure 42**) followed by decay in 8.6 ± 0.6 and 8.9 ± 0.6 ns, respectively. The SB-CS and charge recombination kinetics of **3** provide evidence for localization of the charges on the distal PDI units. The mixed-state lifetimes of **2** and **3** in Tol, which represent the 'dimer limit', are the same, whereas, in THF, full SB-CS does not occur in **2**, but proceeds rapidly from the initially formed FE/CT mixed state in **3**. Moreover, the charge recombination lifetime of the radical ion pair of **3** in THF is 65% longer than the FE/CT mixed-state lifetime in **2**, which is consistent with the reduced electronic coupling expected for radical ions localized on the distal PDIs (**Table 4**). Although the TA results imply the formation of a mixed electronic state with both FE and CT character, we will employ time-resolved vibrational spectroscopy to provide additional evidence for this assignment.

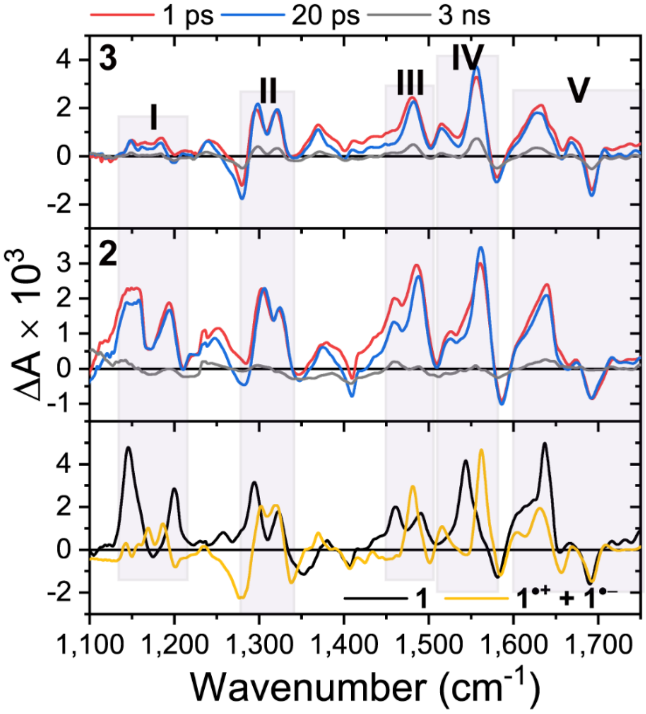

Figure 35. FsIR spectra of **1**, **2**, and **3** in CD_2Cl_2. fsIR spectra of **1** at 10 ps and the charged species (bottom), **2** (middle), and **3** (top) at three time delay points. I–V regions are marked for discussion

in the main text. Excited-state IR-active modes effectively discern the mixed (**2**) and SBCS state (**3**) as they are more sensitive to the electron density of chromophores than electronic transitions, which have broad signals and are congested with various signals.

Transient Infrared Spectroscopy

To probe the FE/CT mixed state with higher spectral resolution, we performed femtosecond infrared (fsIR) absorption (A) measurements (**Figure 35**) probing from 1,100 to 1,750 cm^{-1}, where the signature peaks from the FE and PDI radical anion/cation appear.[79] The fsIR spectra of **1** and charged species ($\mathbf{1}^{\bullet-}$and $\mathbf{1}^{\bullet+}$) are displayed at the bottom, and the calculated fsIR spectra of the charged species are in good agreement with the experimental results. Note that the instrument response of the fsIR instrument is ~500 fs, limiting the observation of FE state evolution to the mixed FE/CT state in **2** and **3**. We explored five spectral regions to demonstrate that **2** forms a mixed FE/CT state, whereas **3** rapidly forms the fully separated SB-CS state. Specifically, in region I (1135-1212 cm^{-1}), containing FE and radical ion features, **2** exhibits strong and broad signals covering all these features, whereas the spectra of **3** show similar characteristics to those of the pure charge-separated species. Region III (1442-1,500 cm^{-1}) has distinct features from FE (1459 cm^{-1}) and charged species (1482 cm^{-1}); whereas **2** displays features from both states, **3** shows a flat absorption profile and low signal at the FE region, and this weak signal diminishes rapidly. Additional analyses on the other regions (II, IV and V) are provided in the additional section. The fsIR spectroscopy gives more detailed information on the dynamic state composition and the nature of the state mixing than electronic TA measurements, suggesting that states B in **2** and **3** from the electronic TA spectra discussed above are indeed different. The fsIR spectra for **2** indicate the coexistence of the FE and CT features, whereas, for **3**, the spectral features correspond to the fully separated SB-CS state.

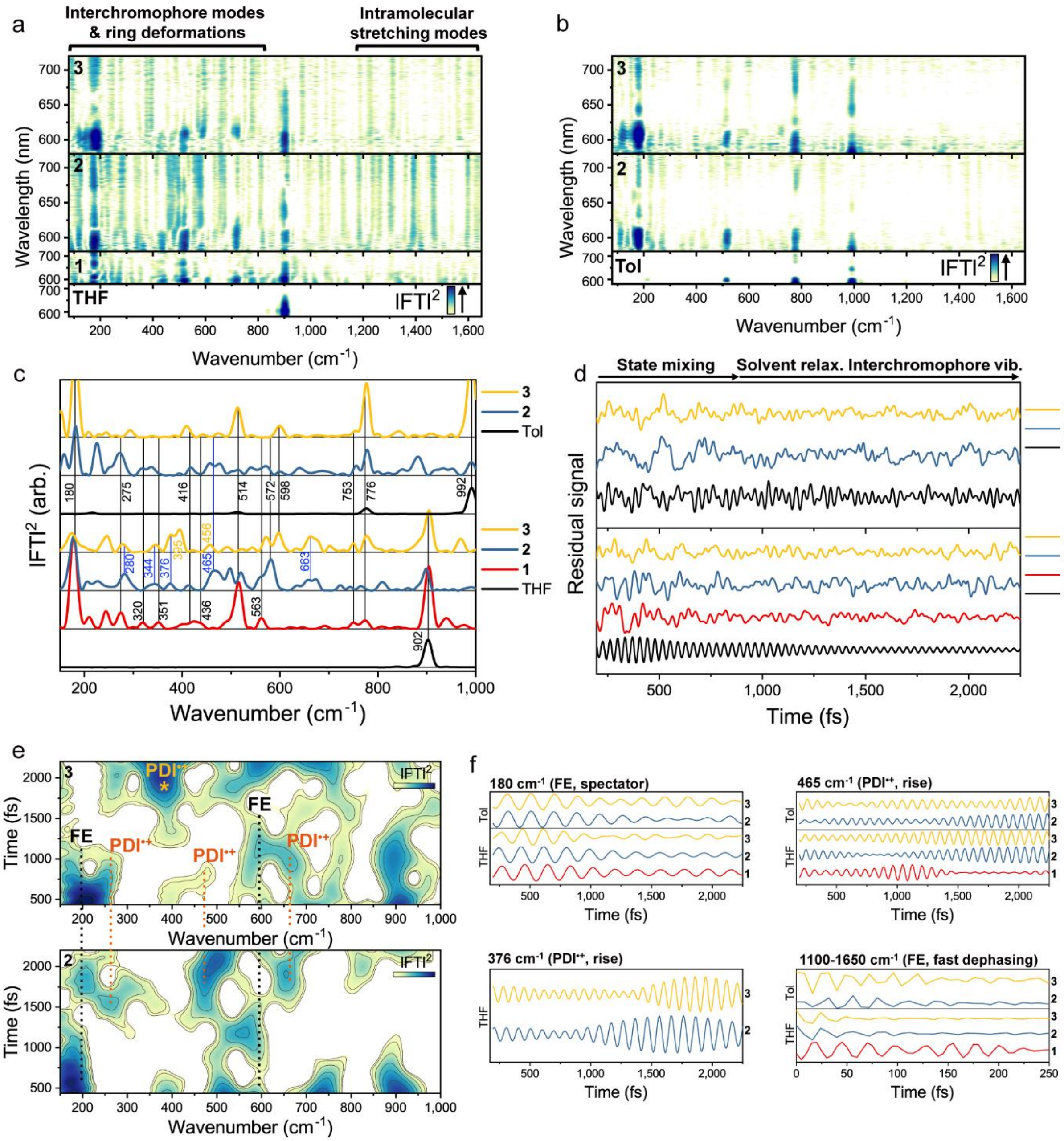

Figure 36. Vibrational coherence measurements and analysis. **a-b,** Fourier power map of (**a**) **1**, **2**, and **3** in THF and (**b**) **2** and **3** in Tol. **c**, Corresponding FT power spectra in the low-frequency region for 630-680 nm SE and ESA signals where FC active modes (black) and the evolution to the mixed state (blue) or/and SBCS (yellow) are denoted with lines and numbers. **d**, Residual oscillatory signals for 630-680 nm (averaged) after subtraction of the population dynamics. **e**,

Short-time Fourier transform analysis (Hanning sliding window) on **2** and **3** in THF where dotted lines represent FE (black) and mixed state (orange) which then further relaxes to the SBCS state (yellow) in **3**. **f**, FFT filter analysis for several regions. As Franck-Condon active modes are similar between chromophores, wavepacket evolution directly gives insights into how vibronic coherences correlate with the electronic state's nature.

Coherent Wavepacket Dynamics

To obtain fundamental insights into the VC in mixed-state formation and solvent relaxation, we carried out broadband TA measurements using an 11-fs compressed pump pulse, the bandwidth of which covers the steady-state absorption spectra of **1**, **2** and **3** and is polarized parallel to the probe pulse. Fourier transform (FT) power maps (**Figure 36a,b**) were obtained by Fourier-transforming the residual signals after subtracting the population dynamics from the TA signals. We can differentiate the VCs from the ground and excited states because the former predominantly lie in the 580-600-nm GSB region and the latter in the 630-680-nm region, which includes contributions from the PDI SE/ESA, FE and radical cation bands. Note that the PDI radical anion absorption band exists at 800 nm and is weak at 630-680 nm[79], and thus does not contribute greatly. Also, detection of the radical anion region near 800 nm proved challenging due to temporal walk-off. This classification is also well reflected in the FT power spectra of **2** and **3** in THF, where most of the vibrational modes in the SE/ESA region are from the excited state. Surprisingly, numerous excited-state wavepackets were detected in **2** and **3**, including low-frequency (<1,000 cm^{-1}) and high-frequency (1,000-1,650 cm^{-1}) regions. The FT power spectra of **2** and **3** for the SE/ESA region are substantially different from those of 1, as shown in **Figure 36c**. The mode assignments of **2** and **3** are based on the spectrum of **1** and DFT calculations on the charged species.

Interestingly, although the residual signals of **1** and the solvents show typical dephasing behavior, those of **2** and **3** have different oscillating patterns, especially in the low-frequency regions (**Figure 36d**): using a temporally broadened pulse (~20 fs) to minimize coherent artefact signals near time zero, we found that, during formation of the mixed state (before 1 ps), **2** and **3** (THF) exhibit rapid dephasing of the oscillatory signals from the high-frequency modes compared to **1**. According to several previous works that have shown that vibronic coherence dephases on timescales intermediate to the purely vibrational and electronic limits,[92-103] this observation indicates vibronic coupling along the high-frequency coordinates of **2** and **3**. Hence, the hastened dephasing of high-frequency modes in the dimeric and trimeric systems can be explained by vibronic coupling along these coordinates. A potential high-frequency vibration that may be coupled to the mixed-state formation is the core C=C stretching mode (~1,590 cm^{-1}), which is supported by its presence in the Fourier power spectra and by a previous study of a CT reaction in a PDI compound.[104] Subsequently, multiple VCs assigned to the radical cation species start to appear due to impulsive population transfer[105] or wavepacket evolution[106] coinciding with solvent relaxation after 1 ps. Most of the growing wavepackets are evident in the low-frequency region. The residual analysis also verifies the similarity of mixed states between **2** and **3** in Tol as their oscillatory signals are comparable (**Figure 36d**). These dynamic oscillatory signals were further examined through the short-time Fourier transform (**Figure 36e**) and the fast Fourier transform (FFT) filter method (**Figure 36f**). Modes that shift or grow are assigned to PDI radical cation modes (260, 390, 465 and 660 cm^{-1}), and the others are assigned to FE modes (180 and 580 cm^{-1}) or solvent modes. Because the FE modes in the low-frequency region are present initially and dephase evenly across the molecular series, they are probably spectator modes orthogonal to the reaction coordinate.[105] In contrast, the low-frequency radical cation modes are presumably coupled to the photoinduced reaction along the solvent relaxation coordinate.[107] Three radical cation modes (260, 465 and 660 cm^{-1}), which become prominent after 1.5 ps in **2**, appear earlier than 1 ps in **3**. Afterwards, **3** exhibits different dynamics: the 260, 465 and 660 cm−1 radical cation bands diminish, and the other radical cation band appears at 390 cm^{-1}. These results suggest that the low-frequency radical cation modes of **3** are sequentially populated following the reaction from the FE to SB-CS state, where the mixed state acts as an intermediate between the two states.

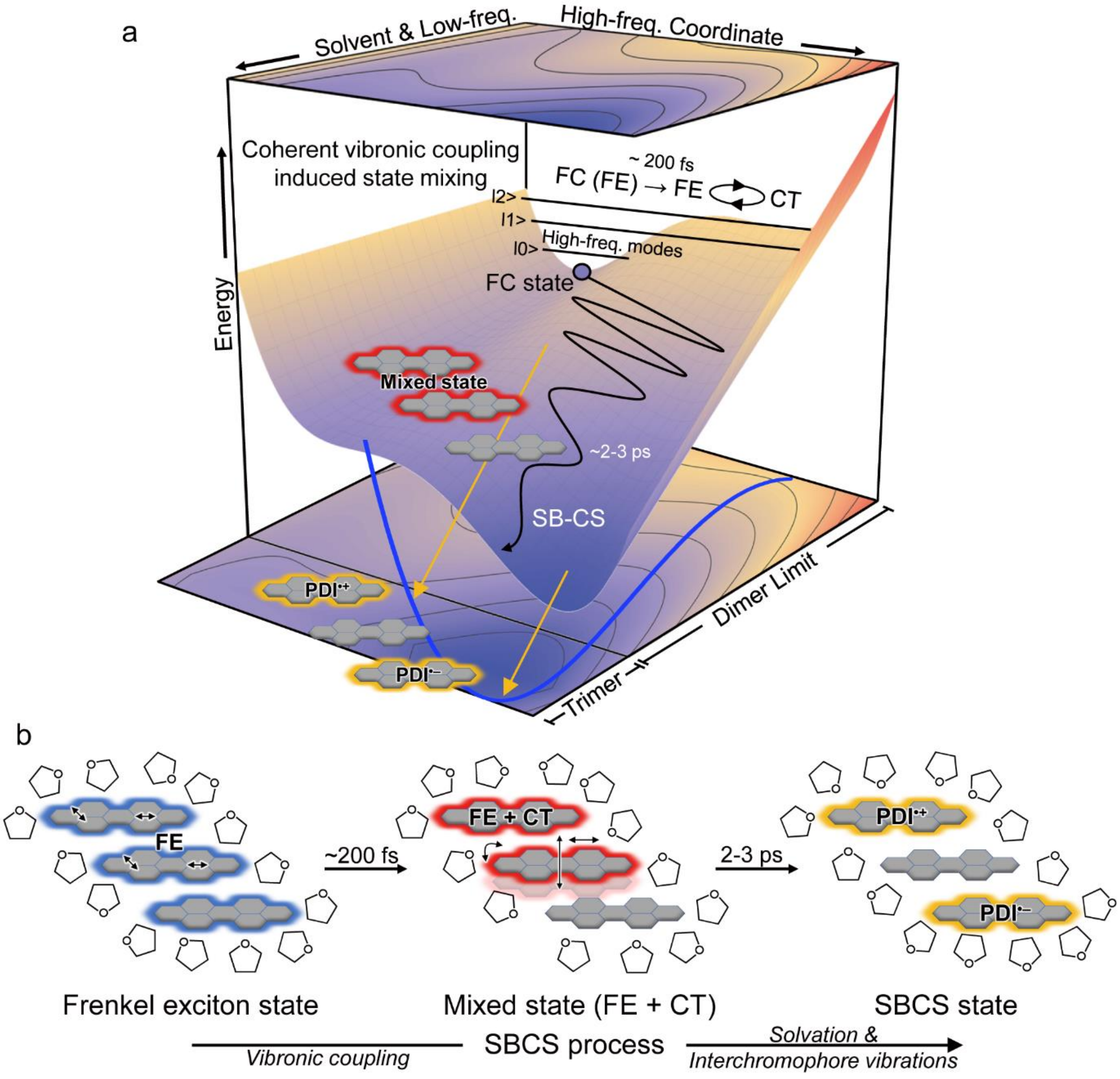

Figure 37. Potential energy surface. **a,** Potential energy surfaces involving the FE/CT mixed state space (dimer limit) and SB-CS state in the trimer (**3**) along the high-frequency and solvation/low-frequency coordinates where vibronic coupling facilitates state mixing followed by solvation/low-frequency collapse the coherence and populate the SB-CS state. **b,** The extent of solvation increases in line with the photoinduced reaction in the trimer which describe the lower energy level of SB-CS state compared to that of the mixed state due to enhanced solvent-solute interactions.

Excited-state Energy Landscape

We can depict the excited-state potential energy surfaces of **2** and **3** along both generalized high-frequency PDI and low-frequency PDI and solvent coordinates (**Figure 37a**). The rapid dephasing (<50 fs in THF) of high-frequency collective stretching modes at 1,100-1,650 cm^{-1} stems from coherent vibronic coupling that induces FE/CT state mixing by modulating the bond order between the π-stacked PDIs. As the mixed state is readily formed within 200 fs, regardless of solvent, vibronic coupling plays a dominant role along the relevant high-frequency coordinate. Although the solvent/low-frequency motions along the other coordinate can stabilize the CT state, increasing the CT character in the FE/CT mixed state and generating the multiple low-frequency VCs observed for the radical cation, strong vibronic coupling still results in FE dominance in the FE/CT mixed state, limiting the ability of the solvent to stabilize it.

Essentially the same FE/CT mixed state is formed initially in both **2** and **3**. However, the solvent is screened from the central PDI in 3, because it is sandwiched between the two distal PDI molecules, each of which has one π surface that is fully solvated. Solvation of the distal PDI in 3 that is not involved in formation of the initial FE/ CT mixed state results in lowering of the energy of the ion pair on the distal PDIs relative to that on the proximal ion pair, whose central ion cannot be as well solvated (**Figure 37b**), resulting in the charges residing on the distal PDI molecules

(**Figure 37b**). SB-CS is also aided by interchromophore low-frequency vibrational modes that can substantially fluctuate the short-range CT coupling, for example, the out-of-plane interchromophore vibration (390 cm^{-1}) observed for the PDI radical cation species. This result thus emphasizes the role of the additional chromophore in collapsing the FE/CT mixed state, with the attendant formation of the desired SB-CS state comprising the distal PDI units.

In conclusion, we have synthesized a null-type, slip-stacked PDI dimer (**2**) and trimer (**3**) and explored the fundamental mechanism that drives ultrafast SB-CS in **3** using the electronic (TA) and vibrational (fsIR and VC) spectroscopies. Following photoexcitation, we find that a mixed FE/CT electronic excited state rapidly forms through coherent vibronic coupling primarily to a 1,590-cm^{-1} high-frequency mode. Solvent relaxation alters the balance between the FE and CT contributions, as indicated by growing VCs from the PDI radical cation. Although **2** remains in the mixed state due to these vibronic and CT couplings, **3** reaches the SB-CS state by interacting with the adjacent chromophore, assisted by solvent relaxation and low-frequency interchromophore vibrational modes (for example, 390 cm^{-1}). The radical ion pair product probably resides on the distal PDI units where these couplings are no longer effective. Therefore, vibronic coupling ultimately accelerates SB-CS between the two outer PDI units, following collapse of the FE/CT mixed state involving two of the three PDI units. This work expands our fundamental understanding of the SB-CS process and provides design principles for efficient charge separation or SB-CS beyond the contact radical ion pair characteristic of dimers.

Methods and Additional Data

Additional broadband TA spectra, fsIR spectra, vibrational coherence measurements and computational details for this work are published in ref.[4]

Synthesis

The overall synthetic procedure is shown in **Figure 38**. Compound **1**, **1a**, **1b**, **4**, **4a** were synthesized according to the previously reported procedures.

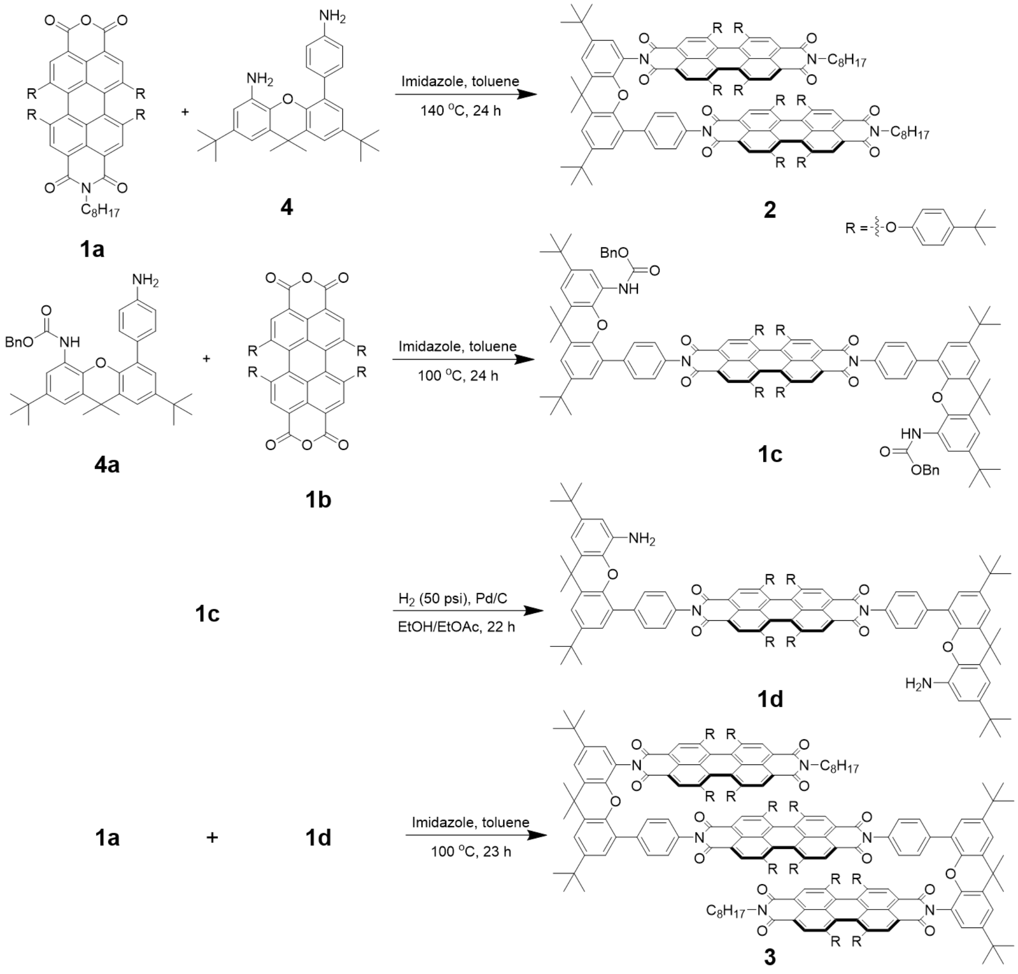

Figure 38. Overall synthesis procedure.

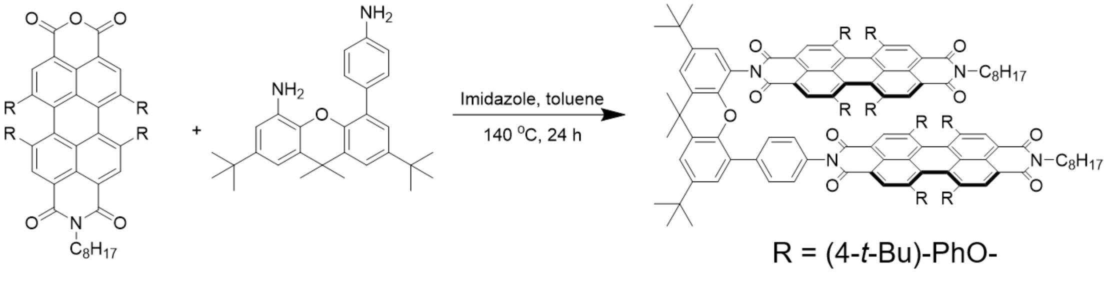

Compound 2.

5-(4-aminophenyl)-2,7-di-tert-butyl-9,9-dimethyl-9H-xanthen-4-amine (**4**, 20 mg, 47 μmol), 5,6,12,13-tetrakis(4-(tert-butyl)phenoxy)-9-octyl-1H-isochromeno[6',5',4':10,5,6]anthra[2,1,9-def]isoquinoline-1,3,8,10(9H)-tetraone (**1a**, 60 mg, 55 μmol), and imidazole (1.0 g) were added into a 50 mL 2-neck round-bottom flask. The system was degassed and injected with toluene (3.5 mL). The system was then heated to 140 °C for 24 h. The crude product was purified by chromatography with hexanes and dichloromethane, and yielded 24 mg (34%) **2** as purple solid. ^{1}H-NMR (CDCl$_3$): δ (ppm) 8.28-8.22 (m, 2H), 8.12 (s, 2H), 8.01 (s, 2H), 7.92 (s, 2H), 7.50 (d, 2H), 7.37 (d, 2H), 7.28 (d, 4H), 7.16 (d, 4H),7.11 (d, 4H), 7.03 (dd, 4H), 6.99 (dd, 4H), 6.94 (br, 4H), 6.75 (d, 4H), 6.64 (d, 4H), 6.23 (d, 4H), 4.09 (m, 4H), 1.81 (s, 6H), 1.36 (s, 18H), 1.33-1.20 (m, 24H), 1.29 (s, 9H), 1.28 (s, 9H), 1.24 (s, 18H), 1.21 (s, 18H), 1.16 (s, 18H), 0.84 (t, 6H). Additional multi-dimensional NMR data for **2** are given in Supplementary Figures 43-45.

MALDI-TOF (m/z): calcd. for $C_{173}H_{178}N_4O_{17}$, 2584.32; found, 2584.26([M]$^+$)

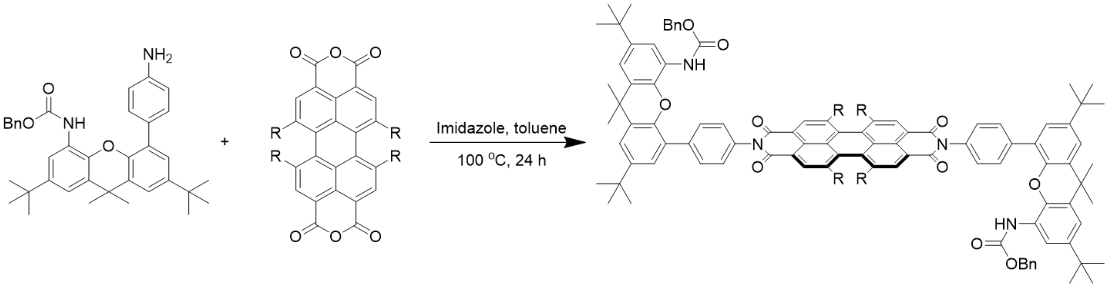

Compound 1c.

Benzyl(5-(4-aminophenyl)-2,7-di-tert-butyl-9,9-dimethyl-9H-xanthen-4-yl)carbamate (**4a**, 12 mg, 21 μmol), 5,6,12,13-tetrakis(4-(tert-butyl)phenoxy)anthra[2,1,9-def:6,5,10-d'e'f']diisochromene-1,3,8,10-tetraone (**1b**, 11 mg, 11 μmol), and imidazole (0.5 g) were added into a 50 mL 2-neck round-bottom flask. The system was degassed and injected with toluene (5.0 mL). The system was then heated to 100 °C for 24 h. The crude product was purified by chromatography with hexanes and dichloromethane, and yielded 20 mg (86%) **1c** as purple solid.

MALDI-TOF (m/z): calcd. for $C_{138}H_{136}N_4O_{14}$, 2074.01; found, 2073.00([M-H]$^-$)

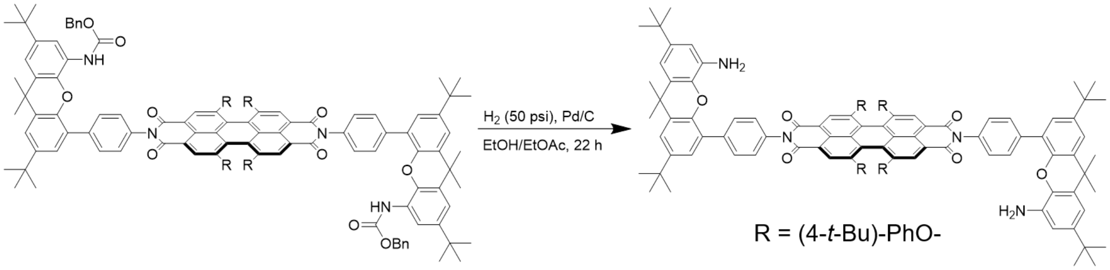

Compound 1d.

To a solution of **1c** (20 mg, 9.6 µmol) in EtOH (5 mL) and EtOAc (10 mL) in a Parr bottle, was added Pd/C (25 mg). The Parr bottle was attached to a Parr hydrogenation apparatus, purged with H_2 (4×55 psi) and then set to shake under H_2 (55 psi) for 22 h. The reaction solution was passed through a celite plug to afford 26 mg of the crude product **1d**. The existence of the target molecule was confirmed by MALDI-TOF and the crude material was carried to the next step without further purification.

MALDI-TOF (m/z): calcd. for $C_{122}H_{124}N_4O_{10}$, 1805.94; found, 1805.93([M]$^+$)

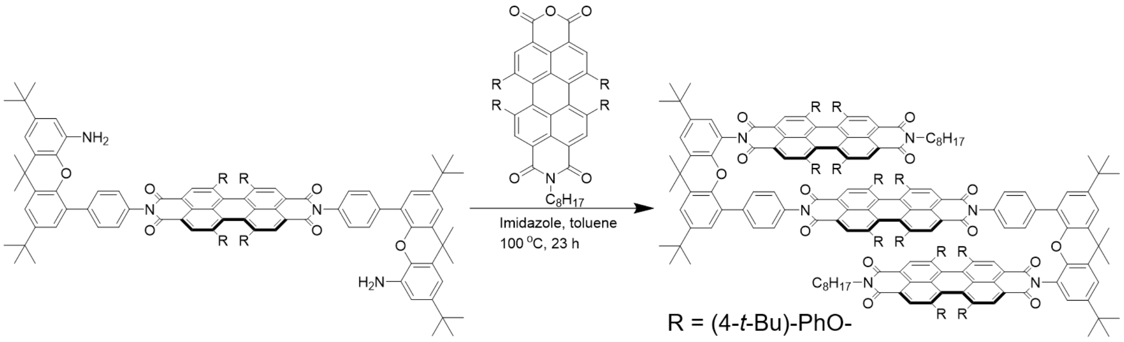

Compound 3.

1d (26 mg, 14 µmol, if pure), **1a** (20 mg, 18 µmol), and imidazole (0.5 g) were added into a 50 mL 2-neck round-bottom flask. The system was degassed and injected with toluene (15 mL). The system was then heated to 100 °C for 24 h. The crude product was purified by chromatography with hexanes and dichloromethane, and yielded 2 mg (5%) **3** as purple solid. ^{1}H-NMR ($CDCl_3$): δ

(ppm) 7.95 (s, 4H), 7.91 (s, 2H), 7.76 (s, 2H), 7.47 (d, 2H), 7.36 (s, 2H), 7.35-7.26 (m, 2H), 7.33 (d, 2H), 7.31 (d, 4H), 7.21 (d, 4H), 7.11 (s, 2H), 7.10 (d, 4H), 7.04-7.01 (m, 8H), 6.98-6.93 (m, 12H), 6.90 (d, 4H), 6.82 (d, 4H), 6.69 (d, 4H), 6.63 (d, 4H), 6.43 (d, 4H), 6.17 (d, 4H), 3.14 (m, 2H), 2.41 (m, 2H), 1.80 (s, 6H), 1.60 (s, 6H), 1.35 (s, 18H), 1.32 (s, 18H), 1.31-1.04 (m, 24H), 1.28 (m, 36H), 1.25 (s, 18H), 1.22 (s, 18H), 1.15 (s, 9H), 1.14 (s, 9H), 1.09 (s, 18H), 0.71 (t, 6H)

Additional multi-dimensional NMR data for 3 are given in Supplementary Figures 46-48.

MALDI-TOF (m/z): calcd. for $C_{266}H_{266}N_6O_{26}$, 3961.97; found, 3961.39([M]$^-$)

Fluorescence and UV-Vis in DCM and Toluene

Steady-state absorption and fluorescence spectra were taken on the same instruments mentioned in the previous chapters.

The steady-state absorption and fluorescence spectra of **2** and **3** in DCM and Tol are shown in **Figure 39**.

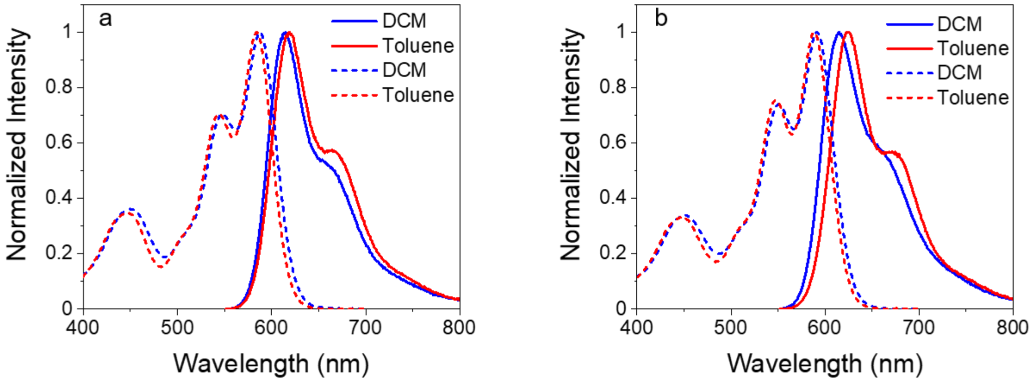

Figure 39. Fluorescence and UV-Vis in DCM and Toluene for **2** (a), and **3** (b)

The energies of the Frenkel exciton state (E_{S1}) are calculated by taking the crossing point of the absorption and emission spectra.

Table 3. Fluorescence quantum yields in DCM and Toluene for **2** (a), and **3** (b)

Compound	**Solvent**	**Quantum yield**	**E_{S1} / eV**
2	DCM	< 0.005	2.07
2	Toluene	0.35 ± 0.01	2.07
3	DCM	< 0.005	2.06
3	Toluene	0.39 ± 0.01	2.05

*The errors for the toluene measurements come from the standard deviations of triplicate measurements. Quantum yields in DCM are below the instrument sensitivity threshold of 0.005, which is taken as the uncertainty.

Narrowband Excitation Transient Absorption Spectroscopy

Femtosecond transient absorption spectroscopy (fsTA) experiments and nanosecond transient absorption spectroscopy (nsTA) experiments were performed on the same instruments mentioned in previous chapters.

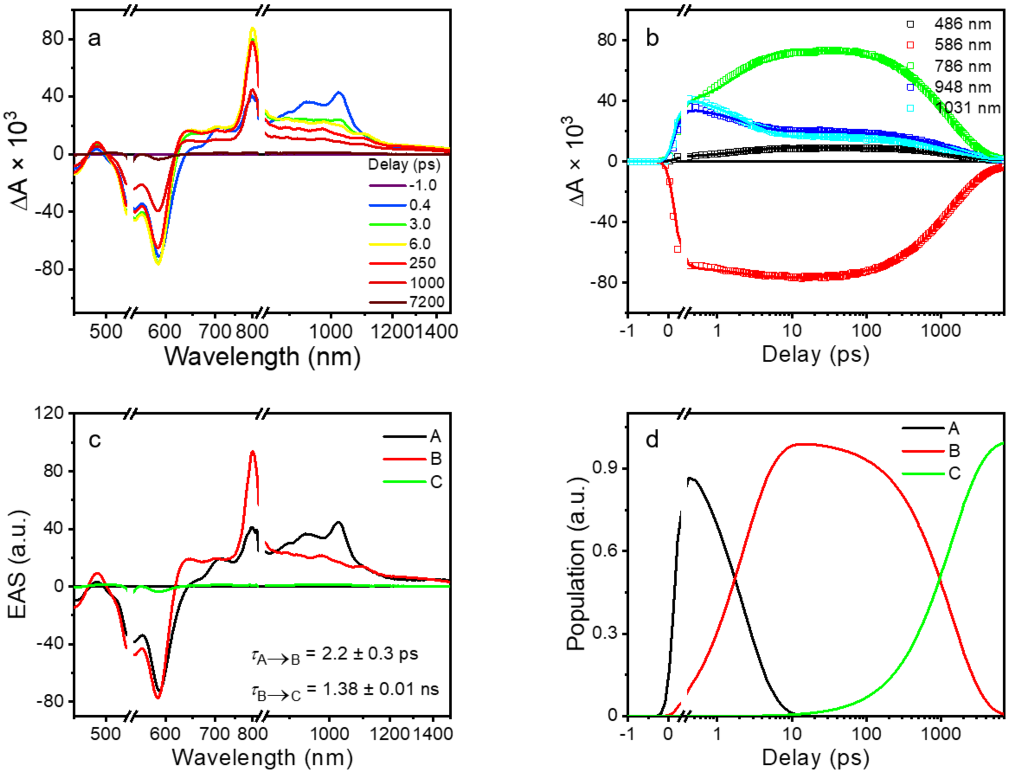

Figure 40. FsTA spectra (ex: 545 nm) of **2** in DCM (a) TA spectra at selected delay times. (b) Kinetic traces at selected wavelengths. (c) Evolution-associated spectra obtained by wavelength global fitting to an A → B → C kinetic model. (d) Population distribution of the kinetic model.

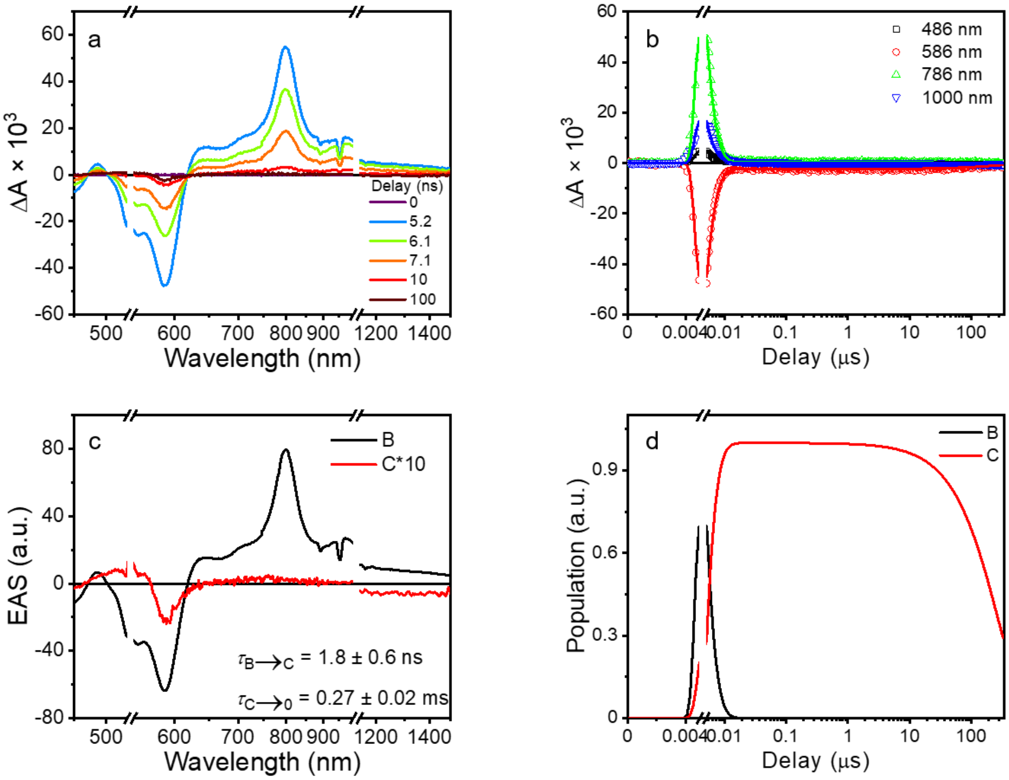

Figure 41. NsTA spectra (ex: 545 nm) of **2** in DCM (a) TA spectra at selected delay times. (b) Kinetic traces at selected wavelengths. (c) Evolution-associated spectra obtained by wavelength global fitting to a B → C → Ground state kinetic model. (d) Population distribution of the kinetic model.

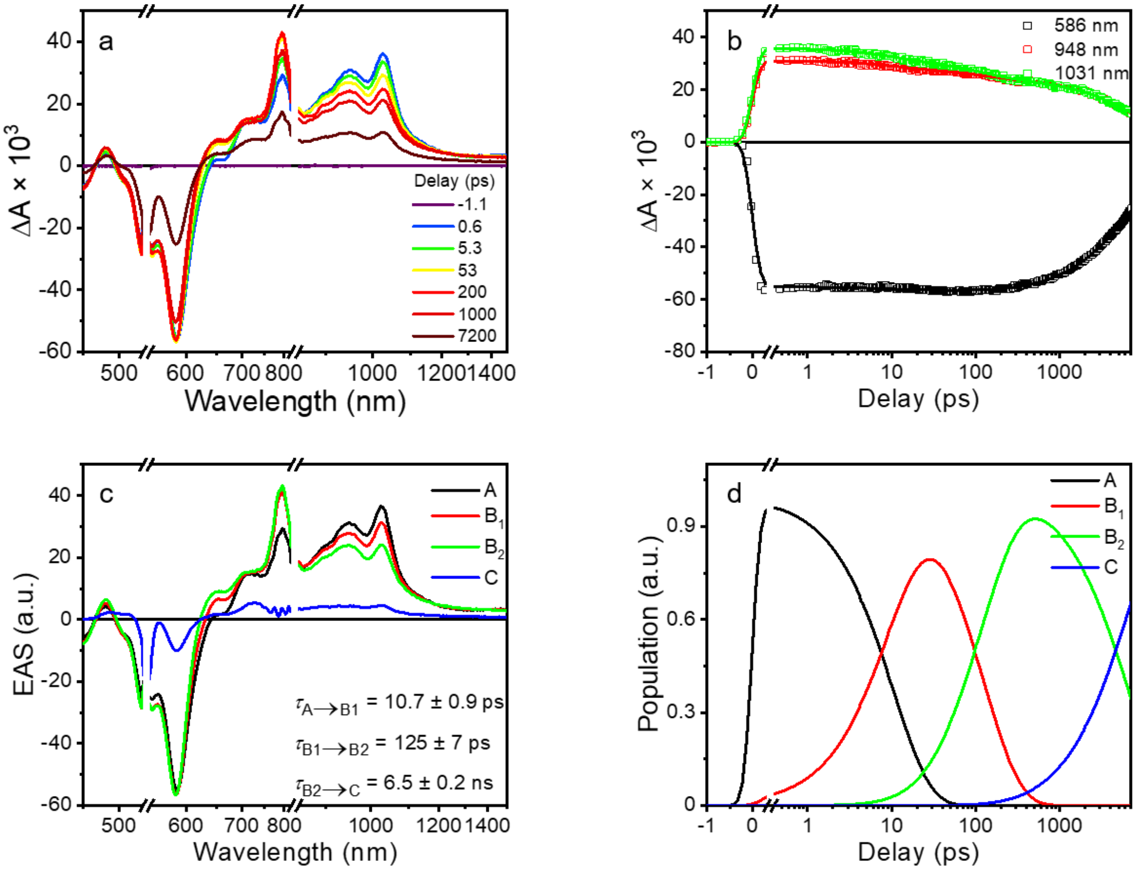

Figure 42. FsTA spectra (ex: 545 nm) of **2** in Toluene (a) TA spectra at selected delay times. (b) Kinetic traces at selected wavelengths. (c) Evolution-associated spectra obtained by wavelength global fitting to an A → B_1 → B_2 → C kinetic model. State D is not fully resolved in this timescale due to the slow rate and 8 ns temporal window of the instrument. (d) Population distribution of the kinetic model.

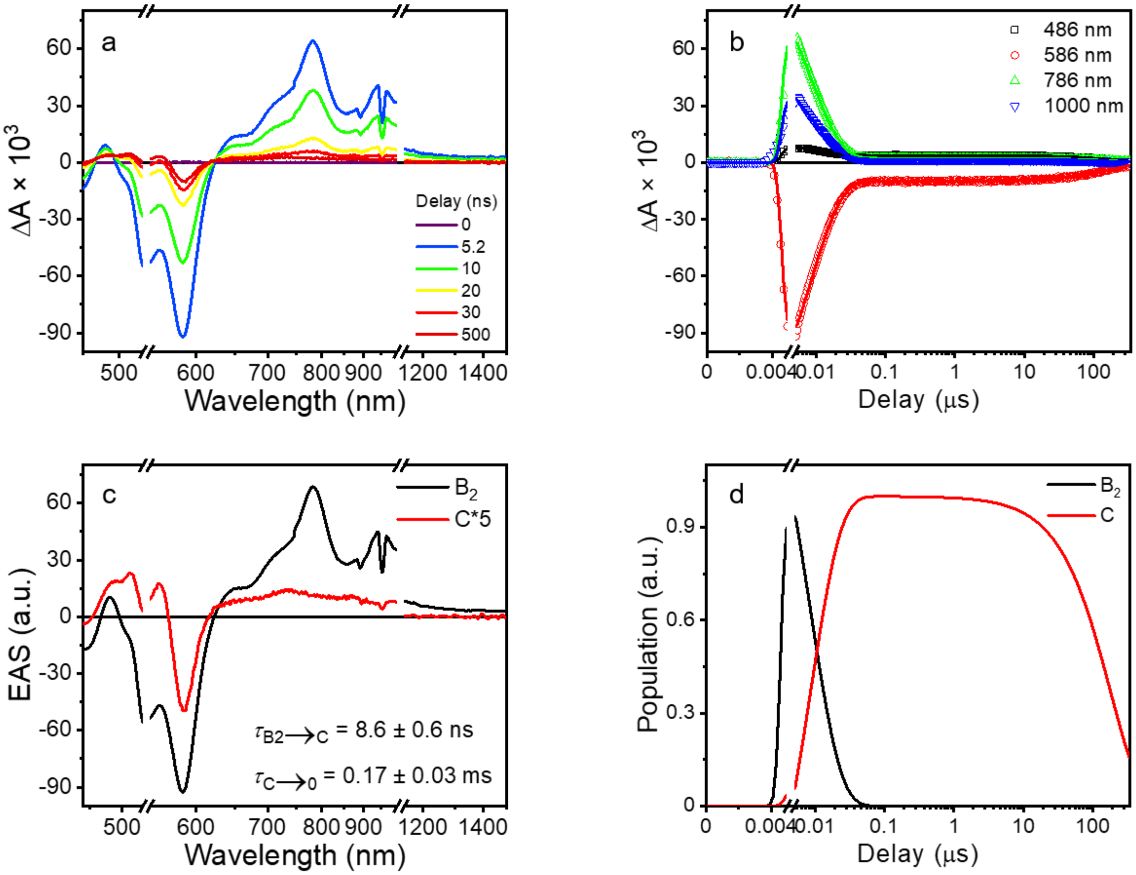

Figure 43. NsTA spectra (ex: 545 nm) of **2** in Toluene (a) TA spectra at selected delay times. (b) Kinetic traces at selected wavelengths. (c) Evolution-associated spectra obtained by wavelength global fitting to a B_2 → C → Ground state kinetic model. (d) Population distribution of the kinetic model.

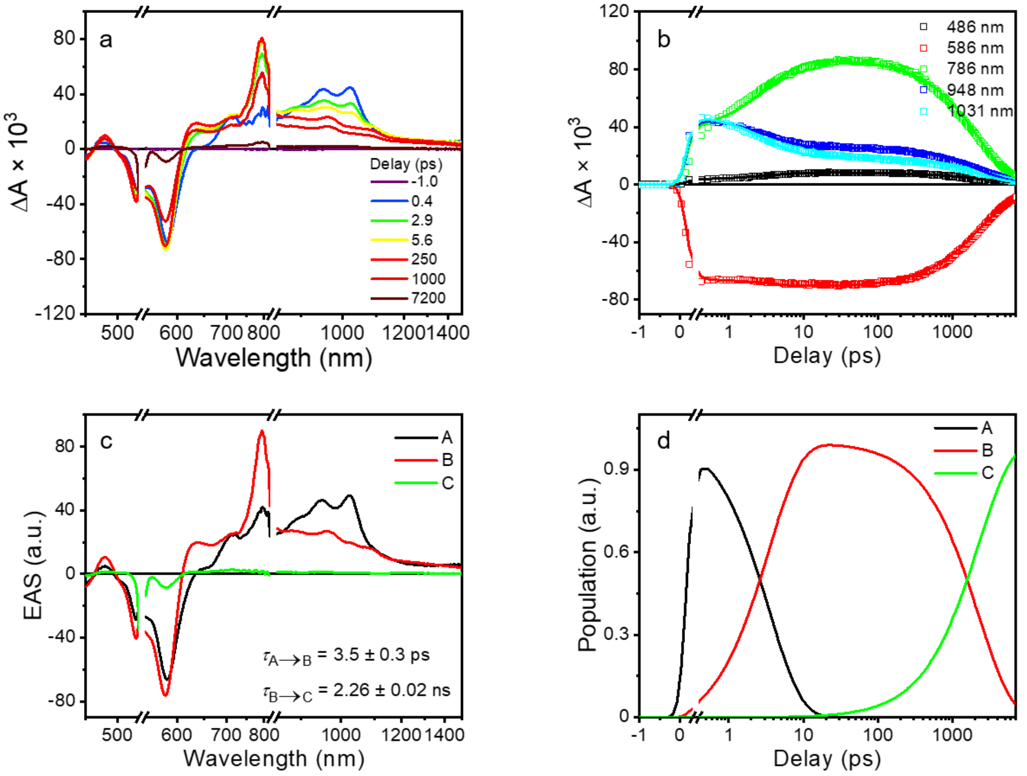

Figure 44. FsTA spectra (ex: 545 nm) of **2** in THF (a) TA spectra at selected delay times. (b) Kinetic traces at selected wavelengths. (c) Evolution-associated spectra obtained by wavelength global fitting to an A → B → C kinetic model. (d) Population distribution of the kinetic model.

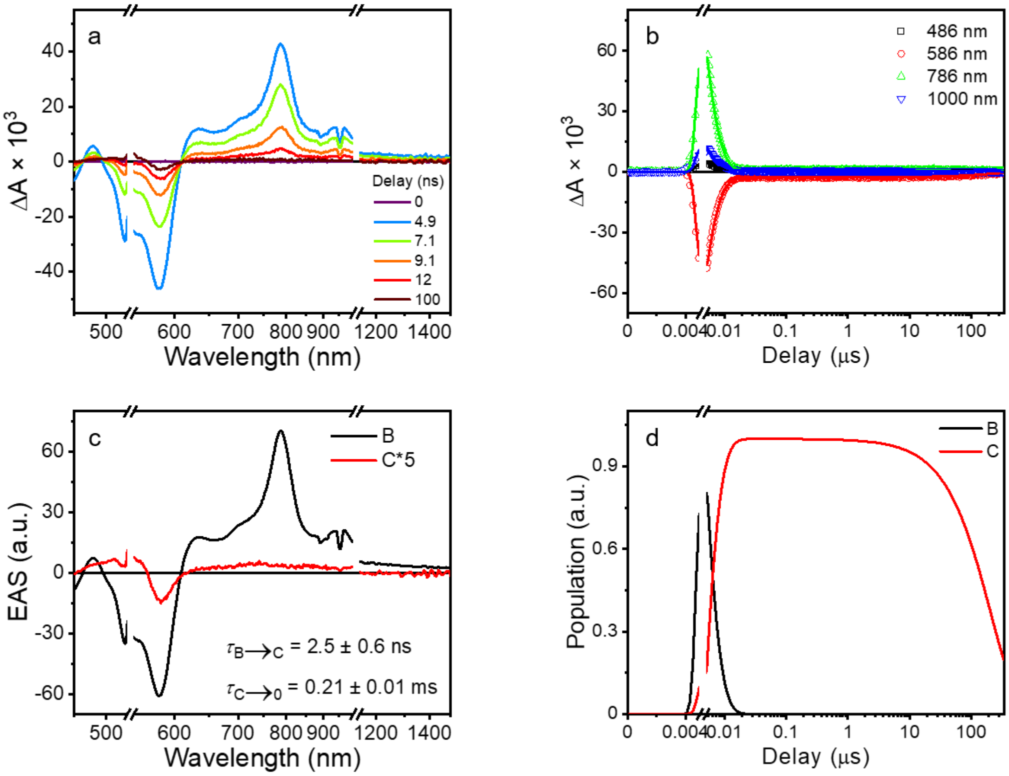

Figure 45. NsTA spectra (ex: 545 nm) of **2** in THF (a) TA spectra at selected delay times. (b) Kinetic traces at selected wavelengths. (c) Evolution-associated spectra obtained by wavelength global fitting to a B → C → Ground state kinetic model. (d) Population distribution of the kinetic model.

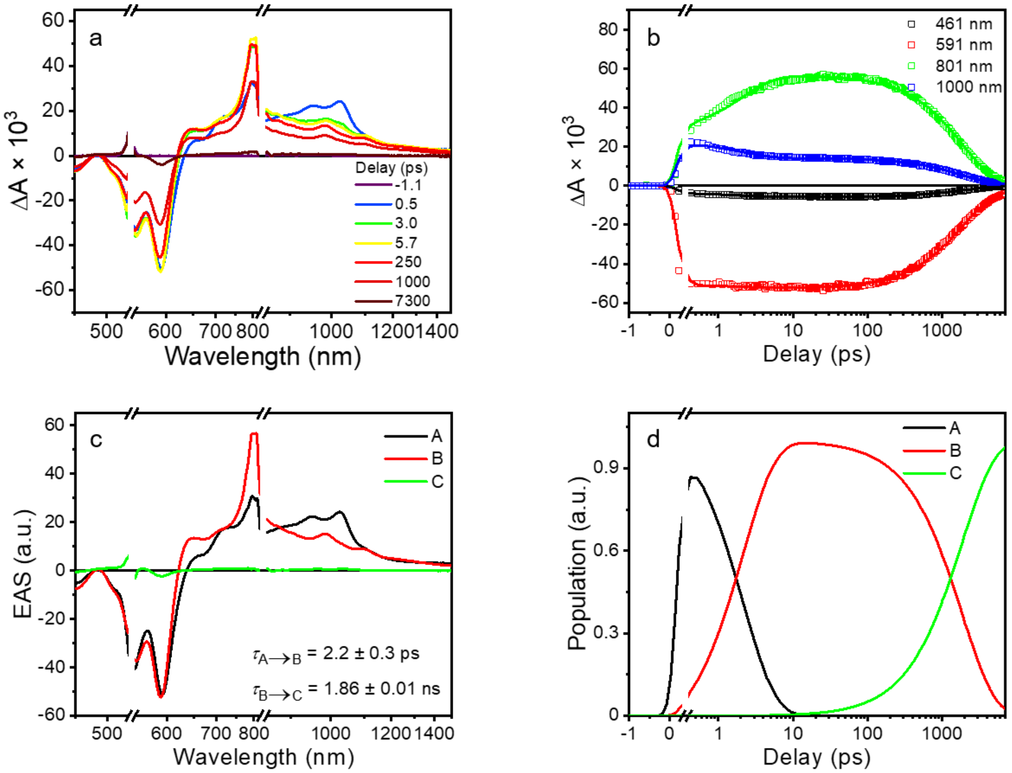

Figure 46. FsTA spectra (ex: 545 nm) of **3** in DCM (a) TA spectra at selected delay times. (b) Kinetic traces at selected wavelengths. (c) Evolution-associated spectra obtained by wavelength global fitting to an A → B → C kinetic model. (d) Population distribution of the kinetic model.

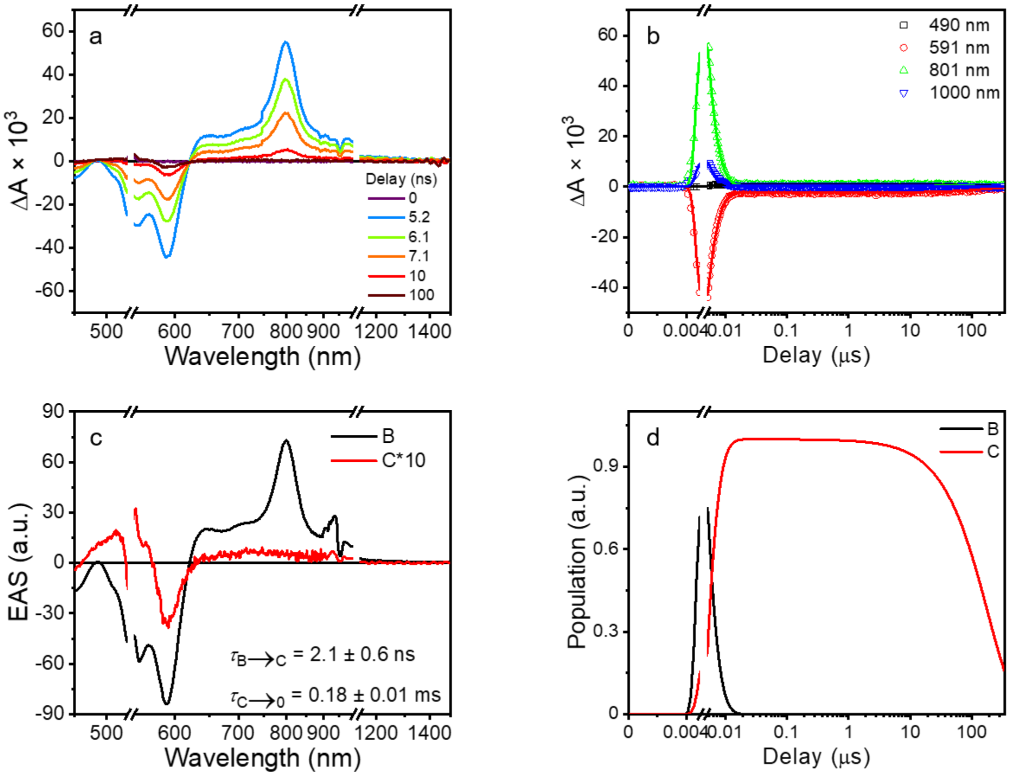

Figure 47. NsTA spectra (ex: 545 nm) of **3** in DCM (a) TA spectra at selected delay times. (b) Kinetic traces at selected wavelengths. (c) Evolution-associated spectra obtained by wavelength global fitting to a B → C → Ground state kinetic model. (d) Population distribution of the kinetic model.

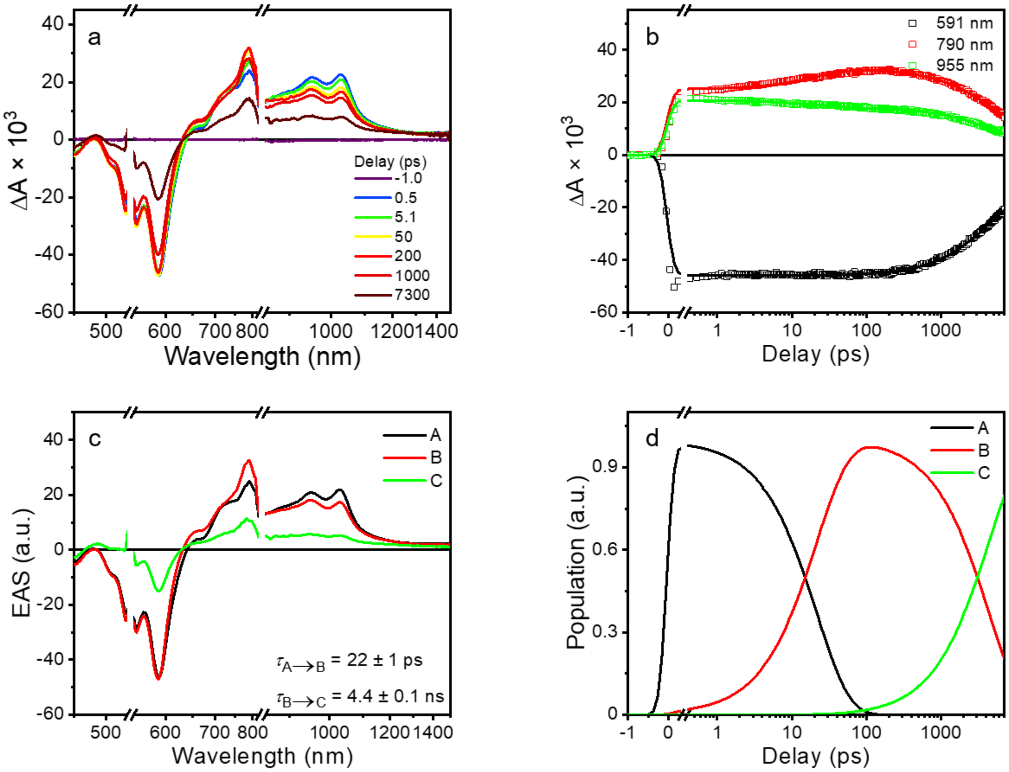

Figure 48. FsTA spectra (ex: 545 nm) of **3** in Toluene (a) TA spectra at selected delay times. (b) Kinetic traces at selected wavelengths. (c) Evolution-associated spectra obtained by wavelength global fitting to an A → B → C kinetic model. The state C is not fully resolved in this timescale due to the slow rate and 8 ns temporal window of the instrument. (d) Population distribution of the kinetic model.

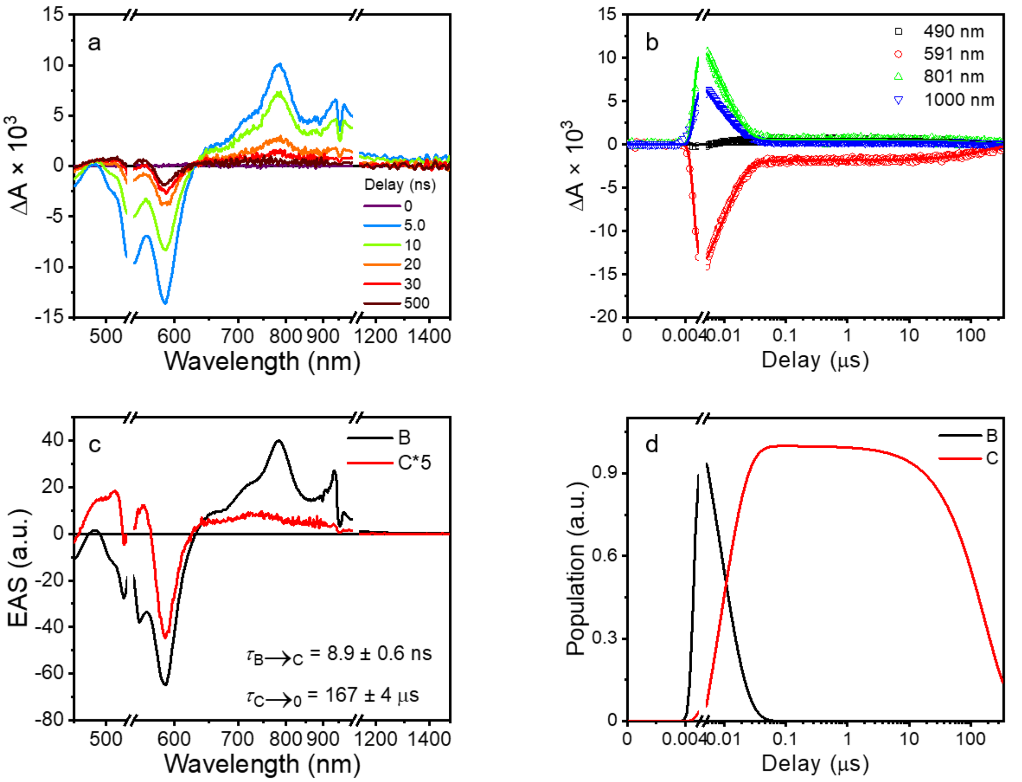

Figure 49. NsTA spectra (ex: 545 nm) of **3** in Toluene (a) TA spectra at selected delay times. (b) Kinetic traces at selected wavelengths. (c) Evolution-associated spectra obtained by wavelength global fitting to a B → C → Ground state kinetic model. (d) Population distribution of the kinetic model.

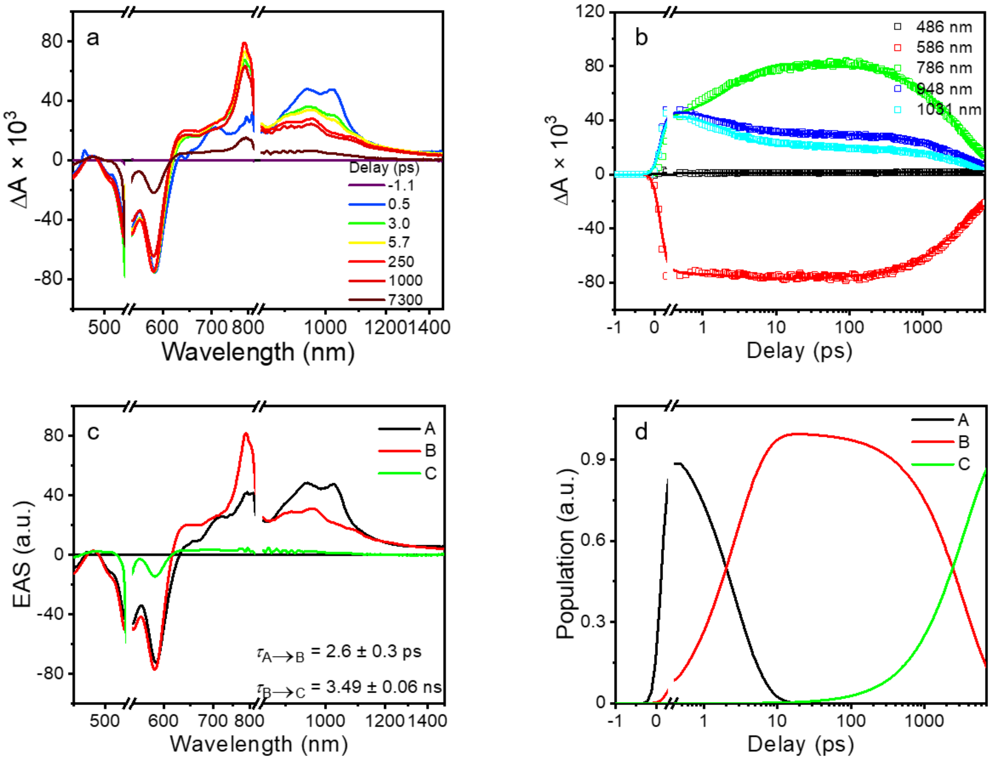

Figure 50. FsTA spectra (ex: 545 nm) of **3** in THF (a) TA spectra at selected delay times. (b) Kinetic traces at selected wavelengths. (c) Evolution-associated spectra obtained by wavelength global fitting to an A → B → C kinetic model. (d) Population distribution of the kinetic model.

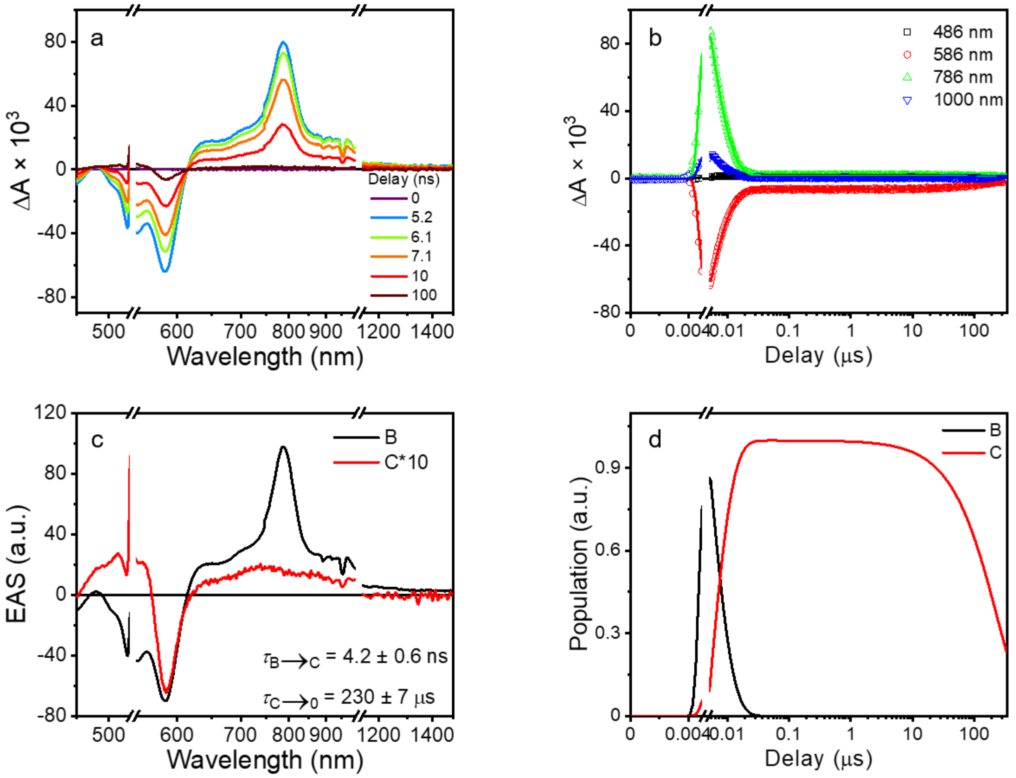

Figure 51. NsTA spectra (ex: 545 nm) of **3** in THF (a) TA spectra at selected delay times. (b) Kinetic traces at selected wavelengths. (c) Evolution-associated spectra obtained by wavelength global fitting to a B → C → Ground state kinetic model. (d) Population distribution of the kinetic model.

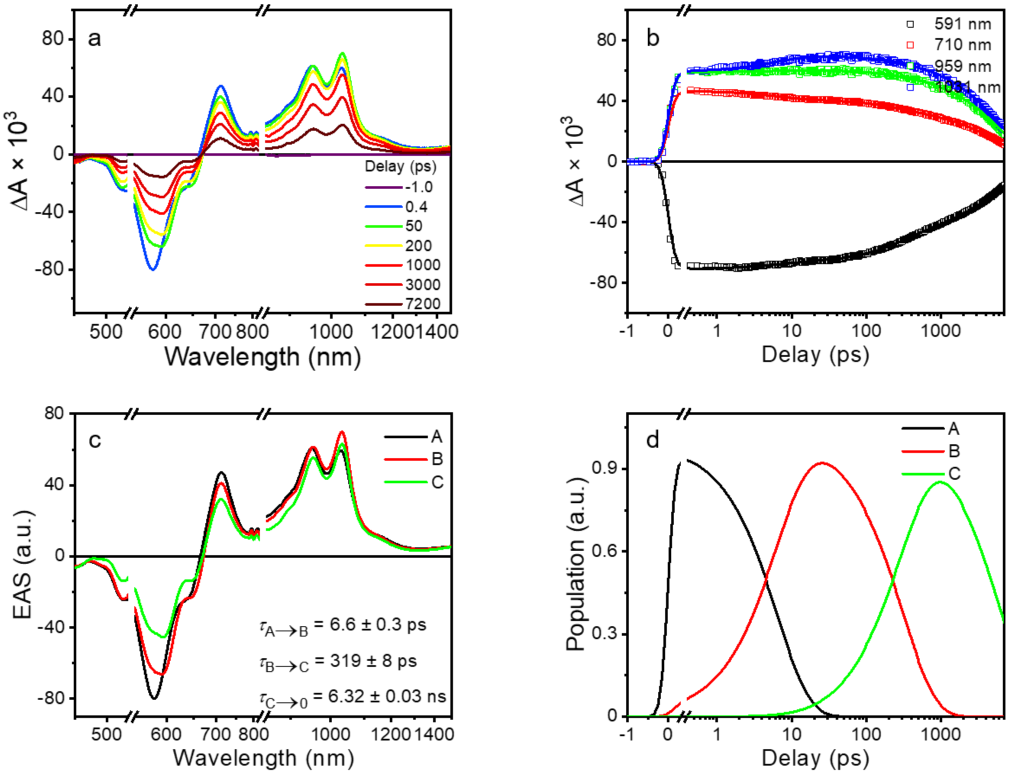

Figure 52. FsTA spectra (ex: 545 nm, 0.5 μJ/pulse) of **1** in THF (a) TA spectra at selected delay times. (b) Kinetic traces at selected wavelengths. (c) Evolution-associated spectra obtained by wavelength global fitting to an A → B → C → Ground state kinetic model. (d) Population distribution of the kinetic model.

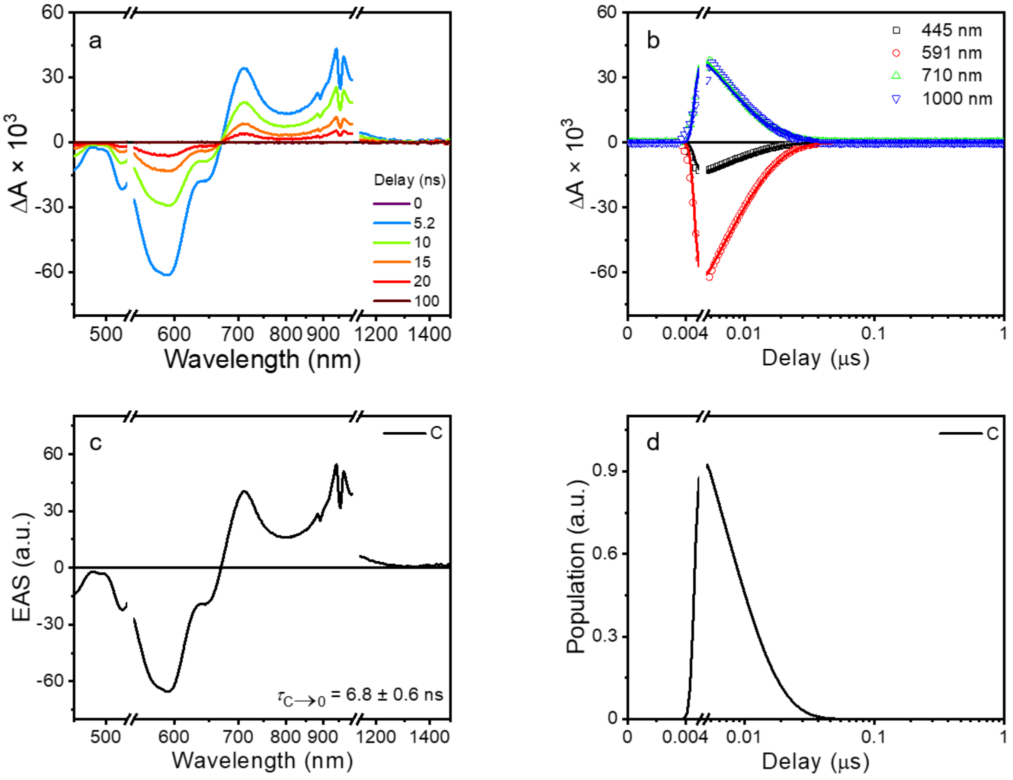

Figure 53. NsTA spectra (ex: 545 nm, 0.5 μJ/pulse) of **1** in THF (a) TA spectra at selected delay times. (b) Kinetic traces at selected wavelengths. (c) Evolution-associated spectrum obtained by wavelength global fitting to a C → Ground state kinetic model. (d) Population distribution of the kinetic model.

The difference in the lifetimes of the state B in THF between **2** and **3**, as described in the main text, is also observed in DCM, which further supports the idea that the presence of a third chromophore alters the nature of this state. The overall faster lifetimes in DCM than in THF originate from the greater dielectric constant, which lowers the energy of the CT state, giving more driving force to the charge separation process. Detailed lifetimes are shown in the table below.

Table 4. Average lifetimes of **2** and **3** in different solvents from narrowband TA measurements

Compound	**Solvent**	$\boldsymbol{\tau_{A\to B}}$ **/ ps**	$\boldsymbol{\tau_{B\to C}}$ **/ ns**	$\boldsymbol{\tau_{C\to 0}}$ **/ ms**

2	DCM	2.2 ± 0.3	1.40 ± 0.09	0.20 ± 0.09
2	THF	3.7 ± 0.3	2.30 ± 0.06	0.206 ± 0.002
3	DCM	2.1 ± 0.3	1.7 ± 0.2	0.20 ± 0.02
3	THF	2.7 ± 0.3	3.8 ± 0.4	0.224 ± 0.009
3	Toluene	21.0 ± 0.9	8.9 ± 0.6	0.19 ± 0.02

*The first two lifetimes are obtained from the fsTA data (except for **3** in toluene) while the third one is from the nsTA data. The errors for the lifetimes are derived from the standard deviation of multiple measurements and propagated with the uncertainty due to the instrument temporal response.

Differential Pulse Voltammetry

Differential Pulse Voltammetry (DPV) experiments were carried out at room temperature in argon-purged solutions of DCM with a Gamry Multipurpose instrument (Reference 600) interfaced to a PC. All DPV experiments were performed using a glassy carbon working electrode (0.071 cm^2). The electrode surface was polished routinely with 0.05 µm alumina-water slurry on a felt surface immediately before use. The counter electrode was a Pt wire and the reference electrode was an Ag wire. The supporting electrolyte, tetrabutylammonium hexafluorophosphate ($TBAPF_6$), was recrystallized in ethanol before use. The cell was dried in an oven immediately before use, and argon was continually flushed through the cell. The internal standard, ferrocene (Fc), was sublimated before use. The spectrum was corrected to the Fc/Fc$^+$ peak at 0.46 V[108].

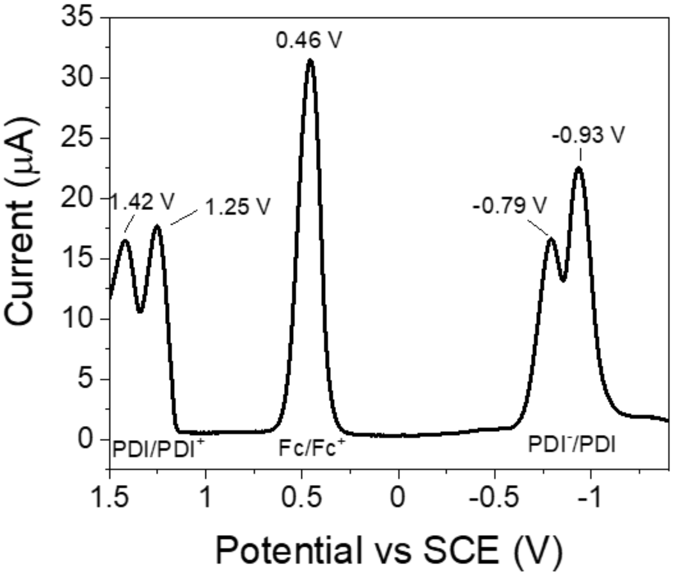

Figure 54. DPV spectrum of **2** in DCM.

Multi-dimensional NMR spectra

The multi-dimensional NMR spectra, including ^1H-^1H Correlated spectroscopy (COSY), ^1H-^{13}C Heteronuclear single quantum coherence (HSQC), and ^1H-^1H Rotating frame Overhauser effect spectroscopy (ROESY), were collected on the Bruker Avance III 500 MHz system w/ DCH cryoprobe (ag500) or w/ Prodigy probe (x500) at Integrated Molecular Structure Education and Research Center (IMSERC) at Northwestern University.

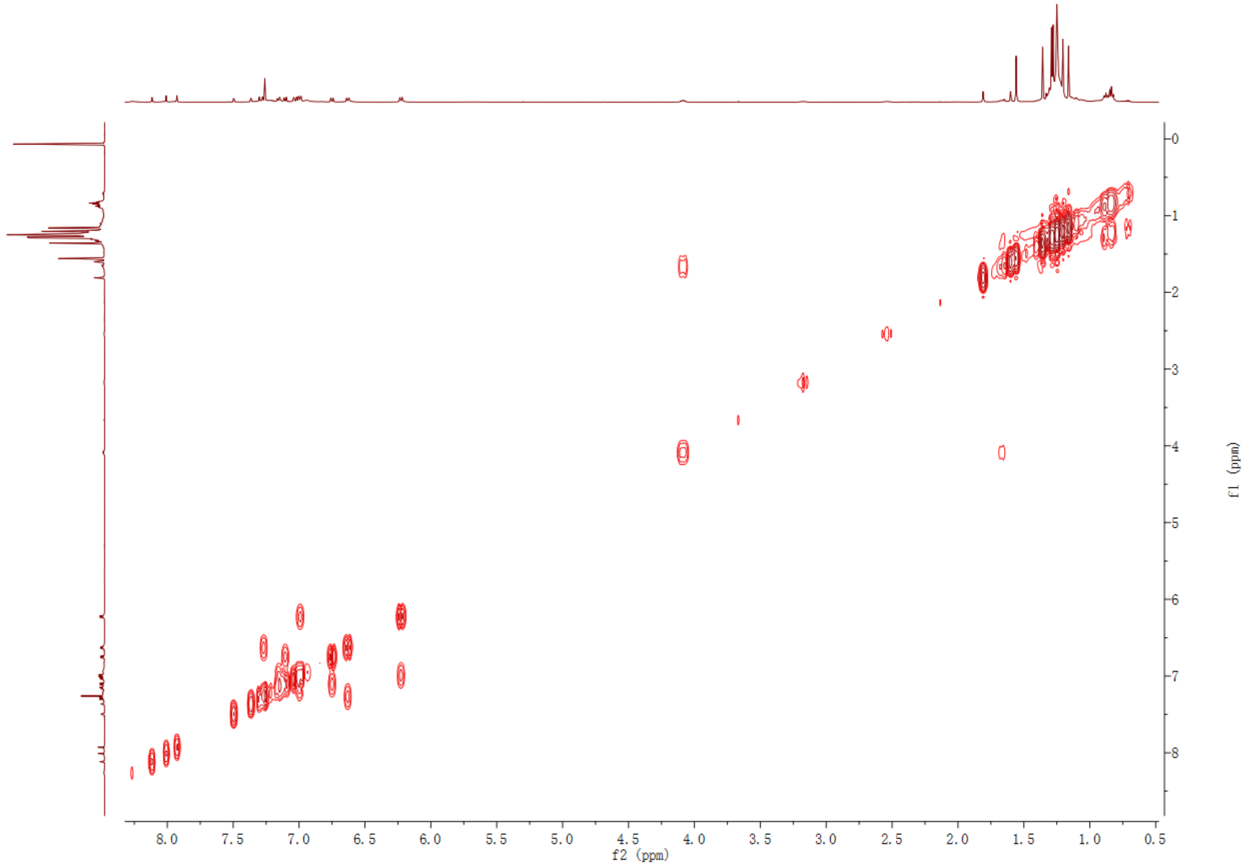

Figure 55. COSY spectrum of **2** in $CDCl_3$.

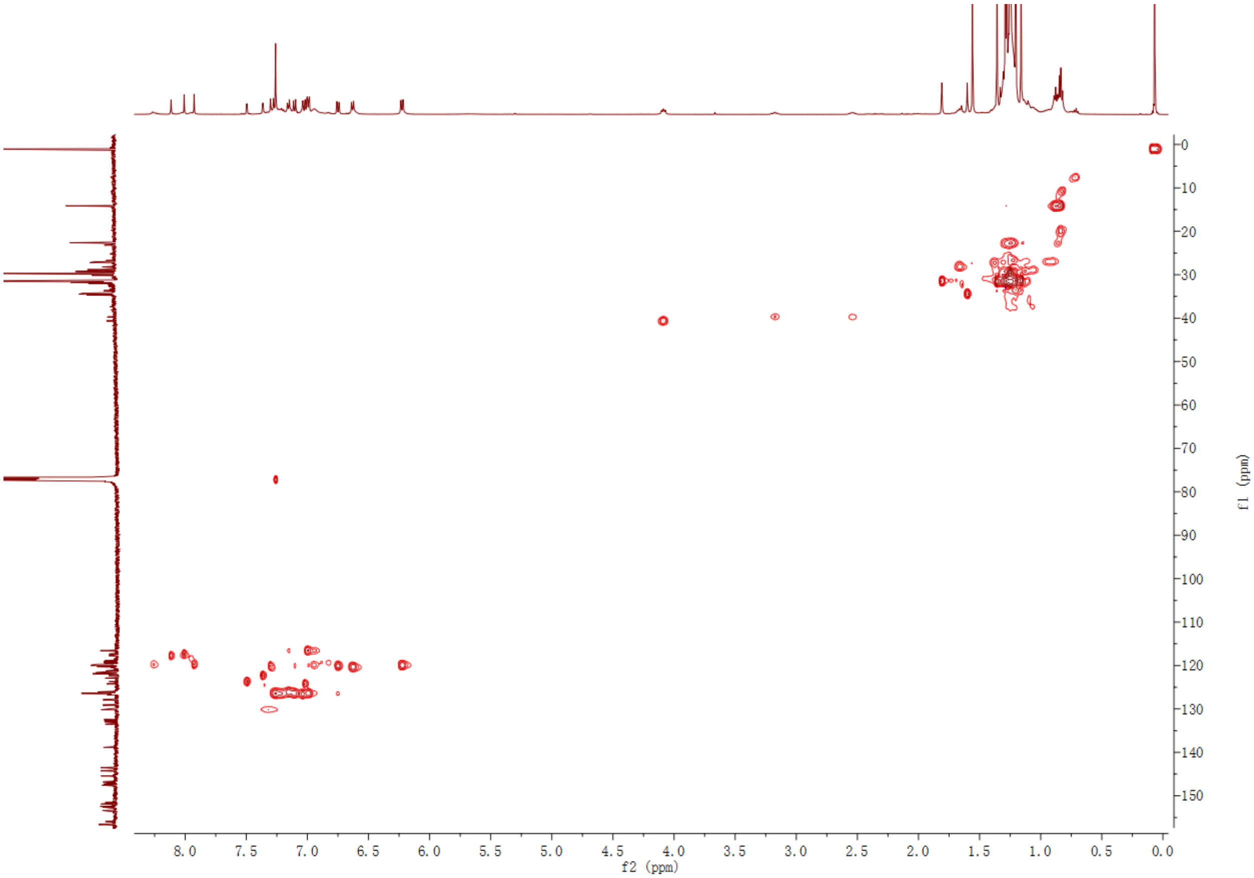

Figure 56. HSQC spectrum of **2** in $CDCl_3$.

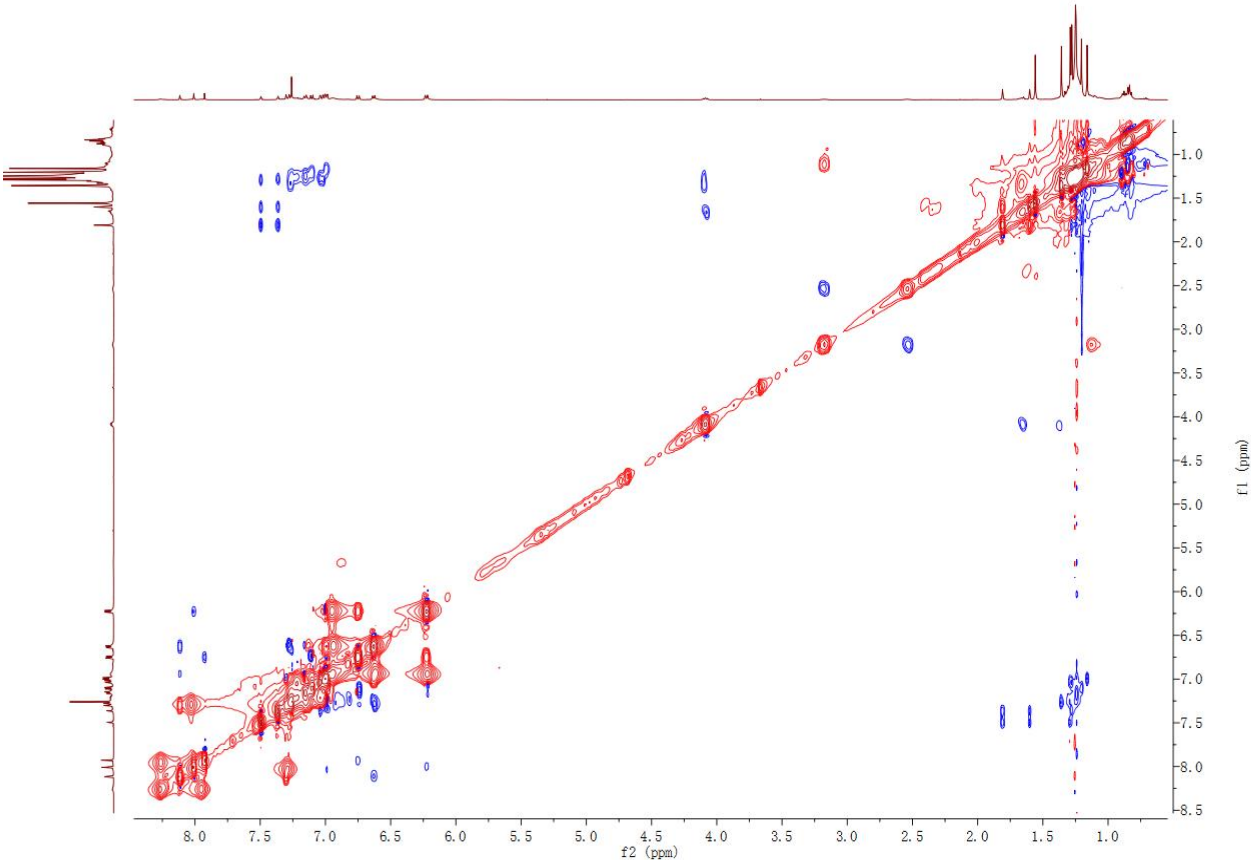

Figure 57. ROESY spectrum of **2** in $CDCl_3$.

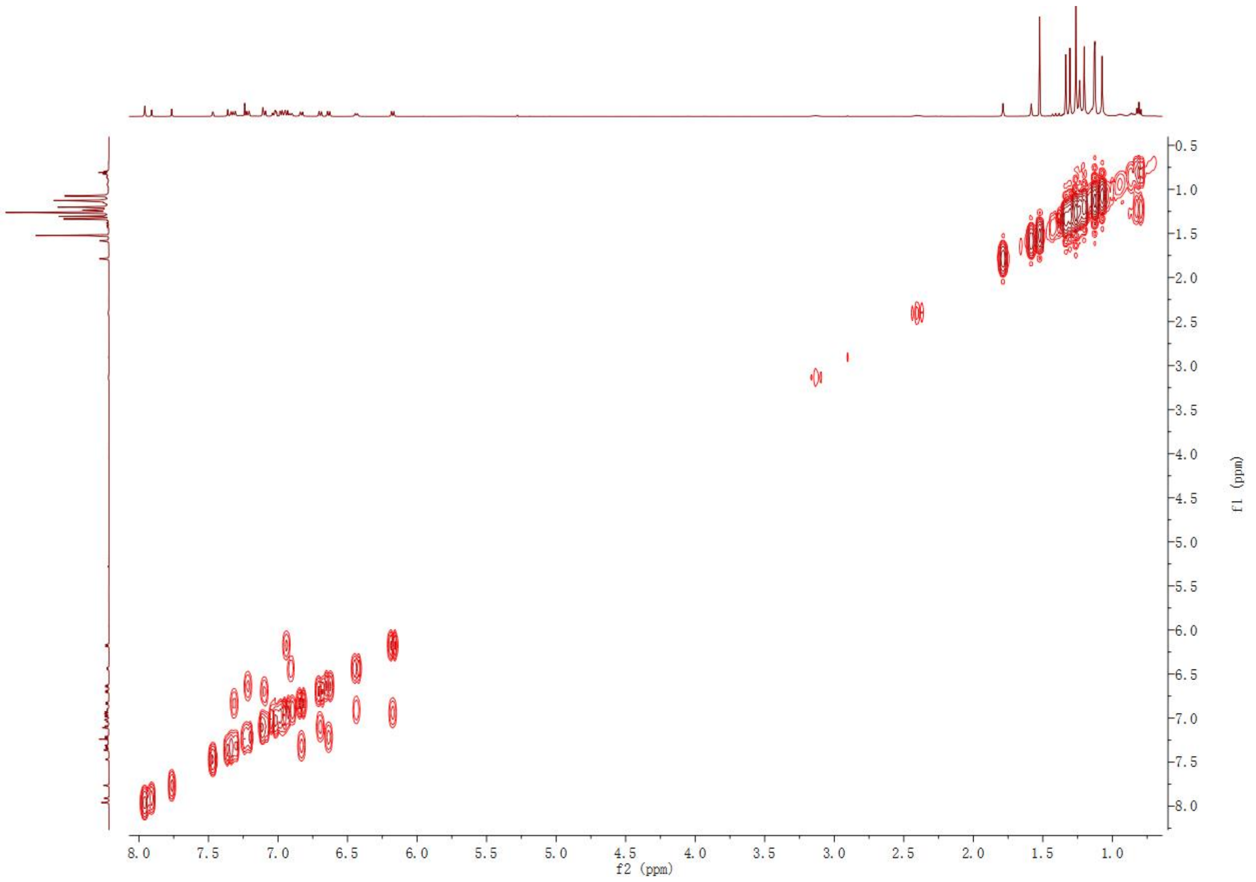

Figure 58. COSY spectrum of **3** in $CDCl_3$.

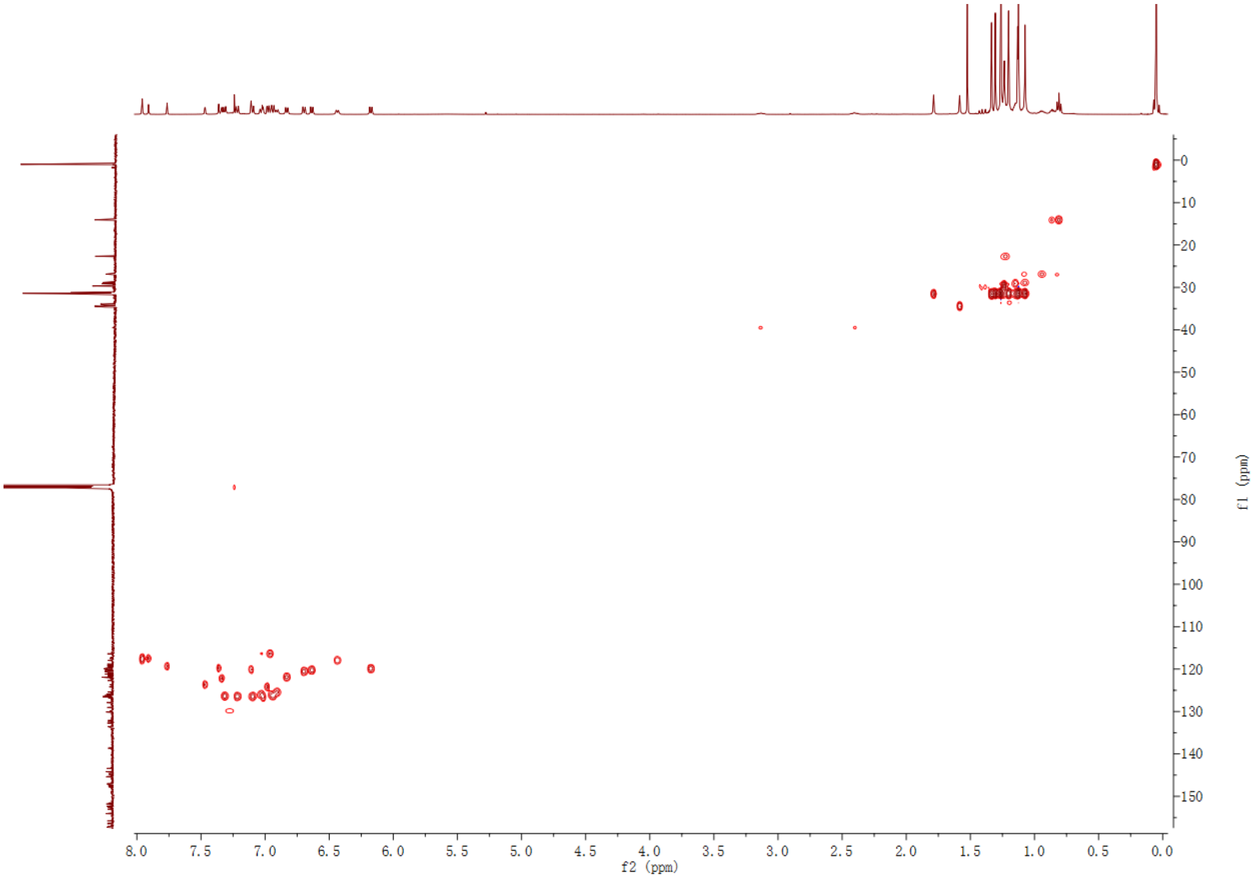

Figure 59. HSQC spectrum of **3** in $CDCl_3$.

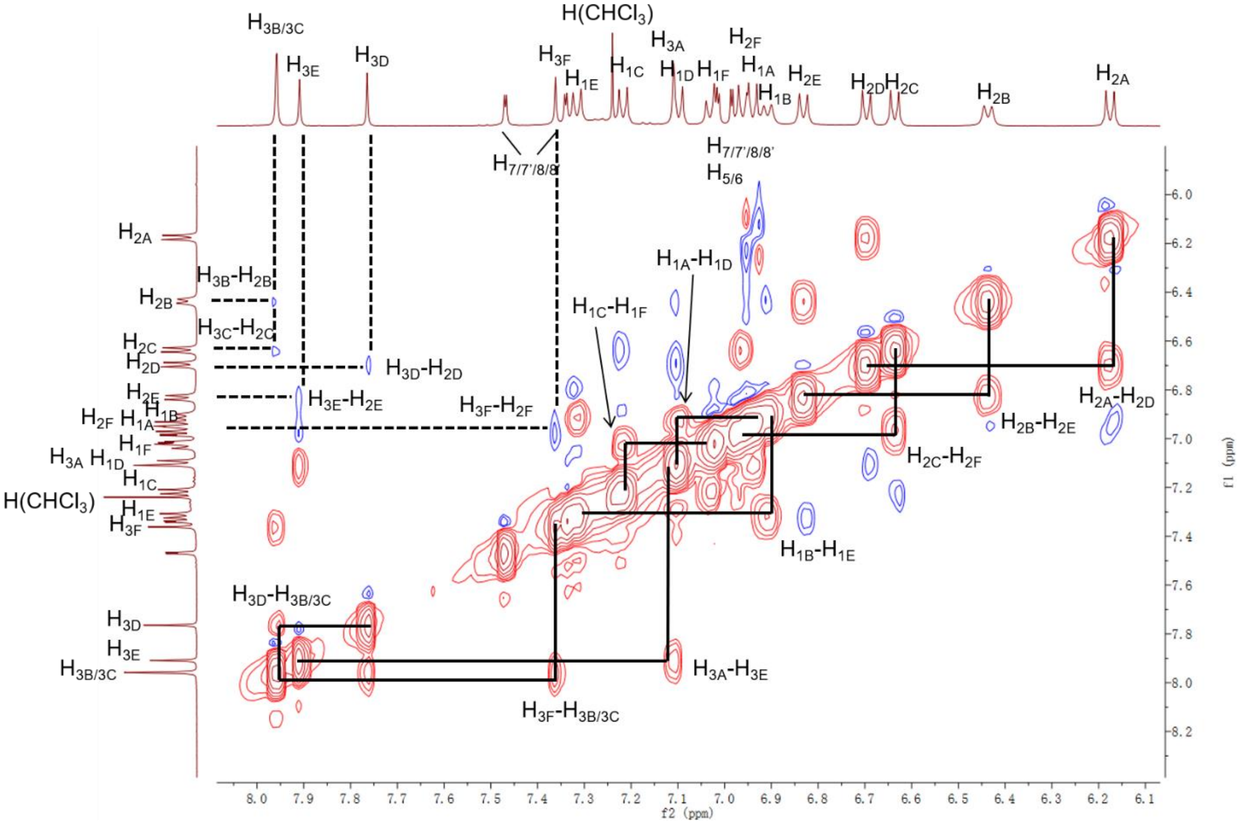

Figure 60. ROESY spectrum of **3** in $CDCl_3$.

The proton labeling of **2** is shown in **Figure 61**, where the two PDIs are divided into four of naphthalenemonoimide (NMI) subunits (A-D). While these subunits are magnetically distinct, an absolute assignment of which protons belong to a particular NMI subunit cannot be made unambiguously. Nevertheless, by analyzing the ^{1}H-NMR spectrum, COSY spectrum, and ROESY spectra, the NMR peaks within each subunit can be assigned. The proton correlations between different NMI subunits are shown in the solid lines in **Figure 57**. Among the six possible different interactions between the four NMI subunits (A-B, A-C, A-D, B-C, B-D, C-D), there is one interaction (B-C) not shown in the spectrum, which is assigned to the most distal NMI units. Regardless of the correspondence between the proton peaks A-D and the relative NMI subunit positions, there is always a proton correlation between protons within two NMI units located on the different PDIs, which supports the stacked structure of **2**.

We applied a similar analysis to **3**, which is divided into six NMI subunits (A-F). The proton correlations on both positions 1 and 2 between the subunits A-D, B-E, C-F are observed (**Figure 60**, solid lines on the top right part), thus it is reasonable to assign these three pairs to three different PDIs. The proton correlations of positions 1 and 3 between subunits A-E, F-B (or F-C), D-B (or D-C) are also observed (**Figure 60**, solid lines on the bottom left). In the case of unit F interacting with unit C, two of the three interactions (A-E, DB/ C) arise from different PDIs, which supports the stacked structure of **3**.

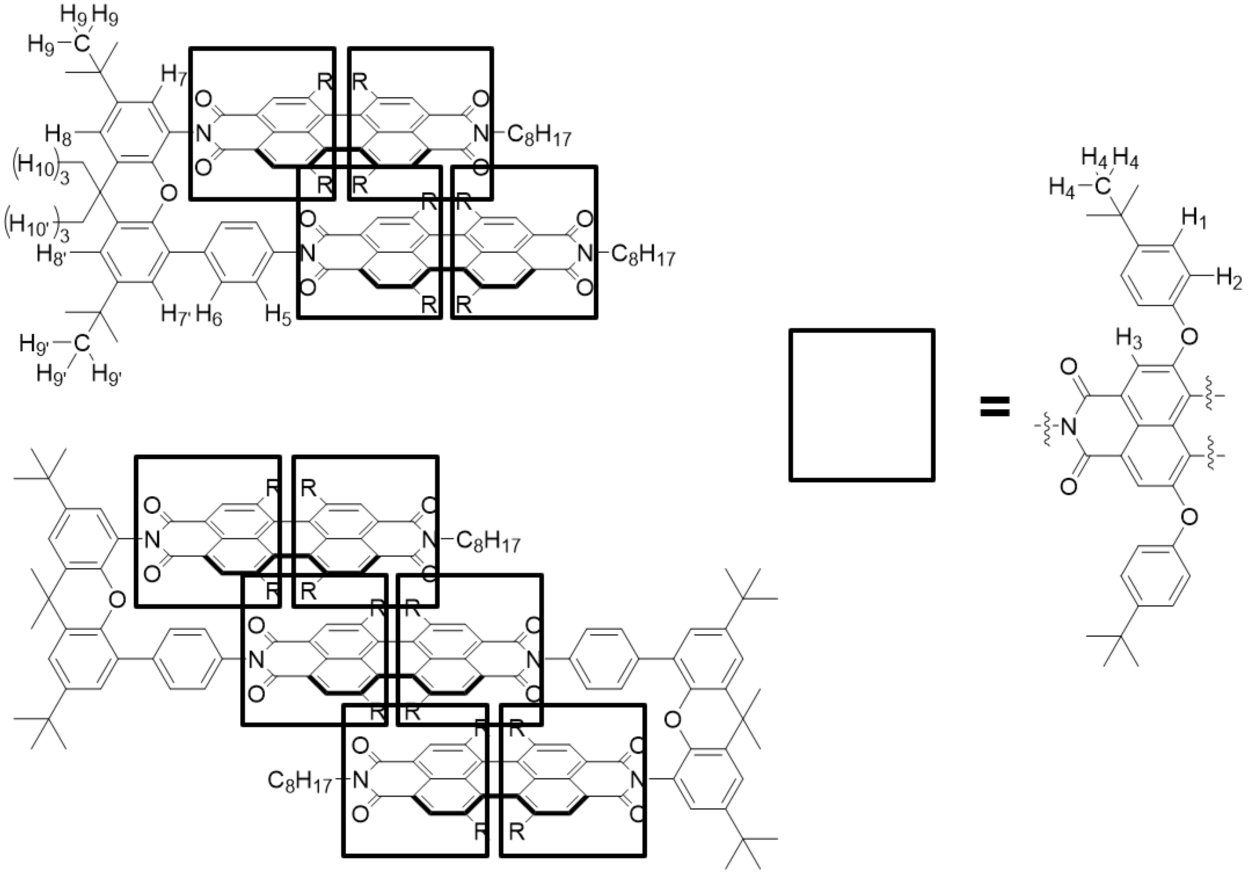

Figure 61. Proton labeling of **2** and **3** (ignoring the octyl tails for simplicity). The PDI units are divided into NMI units (A-D for **2** and A-F for **3**), the labels of which are shown on the right side. The same labeling systems for the xanthene-phenyl bridge are used for both **2** and **3**.

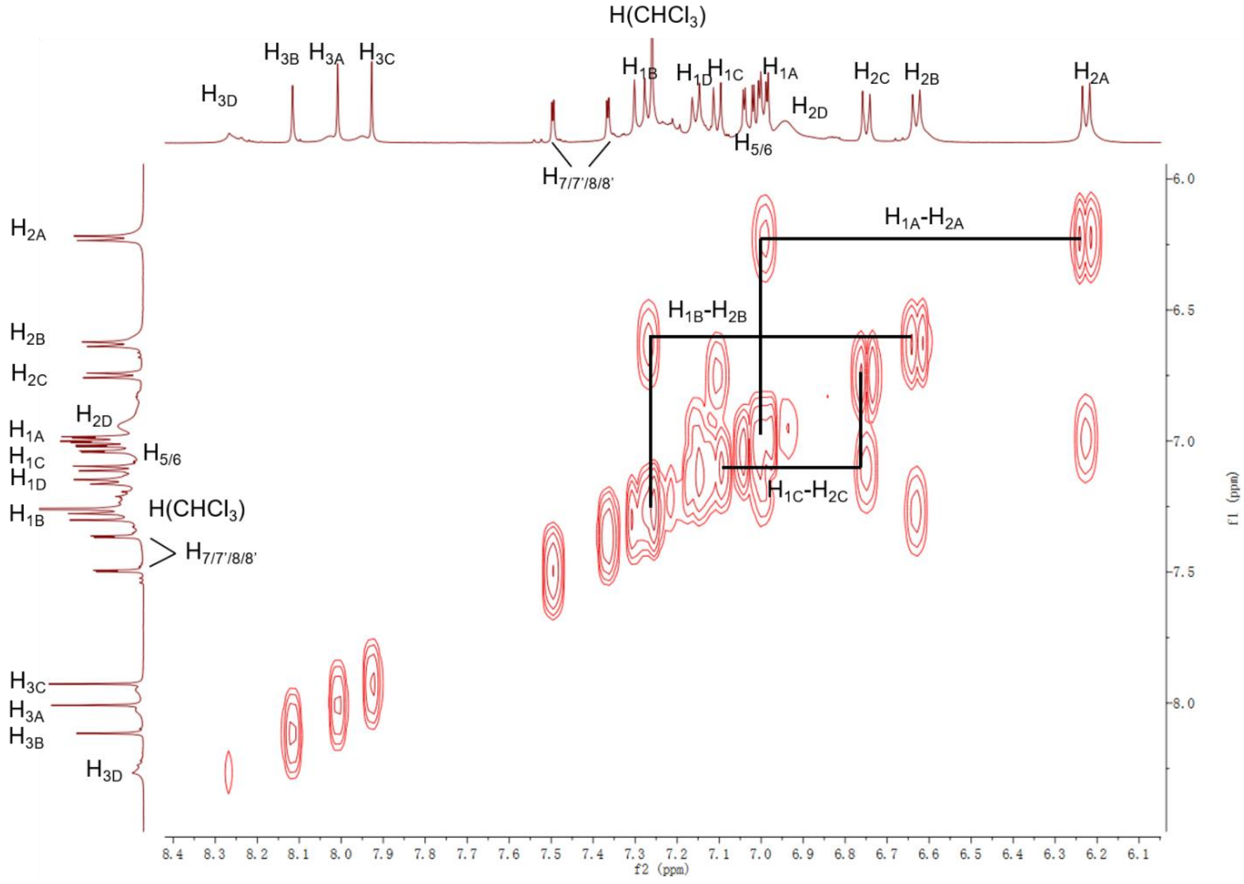

Figure 62. COSY spectrum of **2** in $CDCl_3$ scaling to the aromatic area. The solid lines show the proton correlations between the 1 and 2 positions on the NMI units.

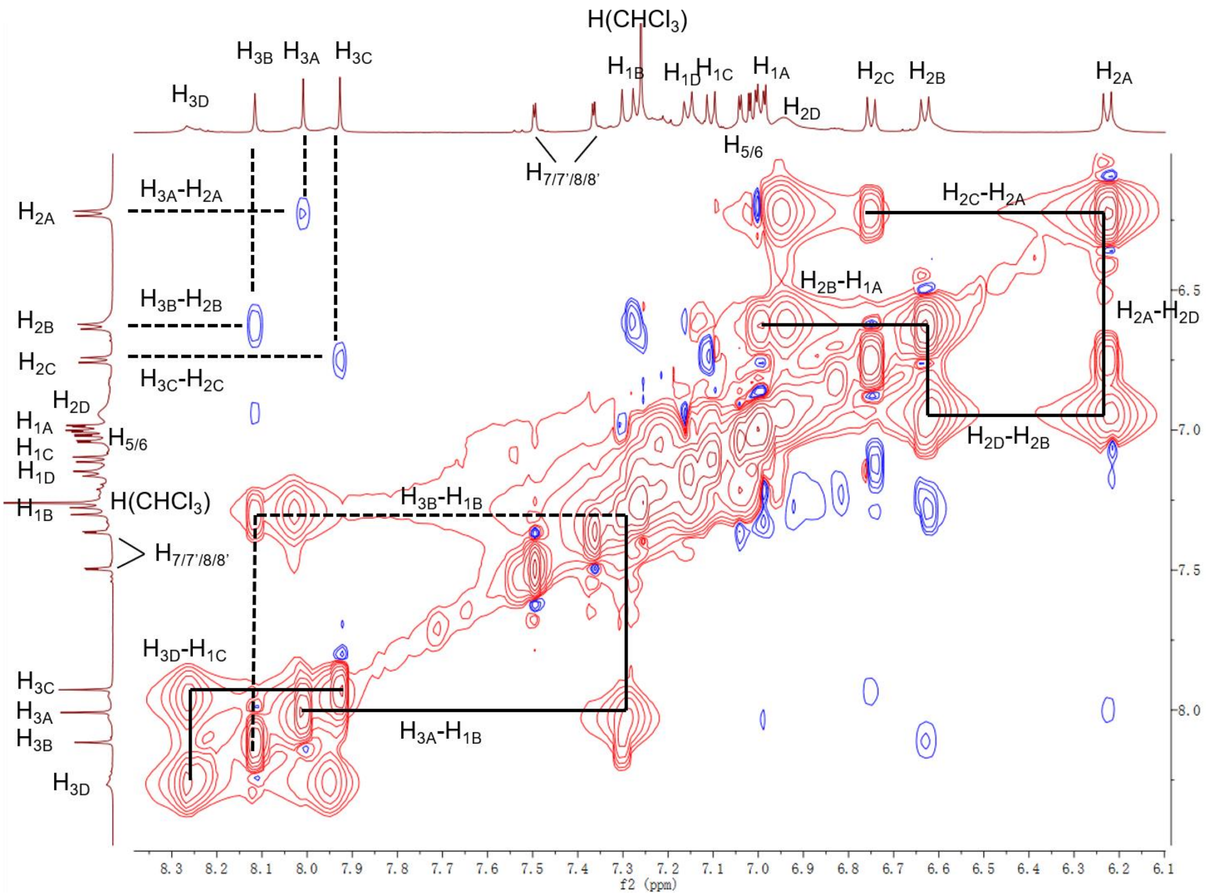

Figure 63. ROESY spectrum of **2** in $CDCl_3$ scaling to the aromatic area. The dashed lines show the proton correlations within one NMI unit, where the solid lines show the proton correlations between two different NMI units.

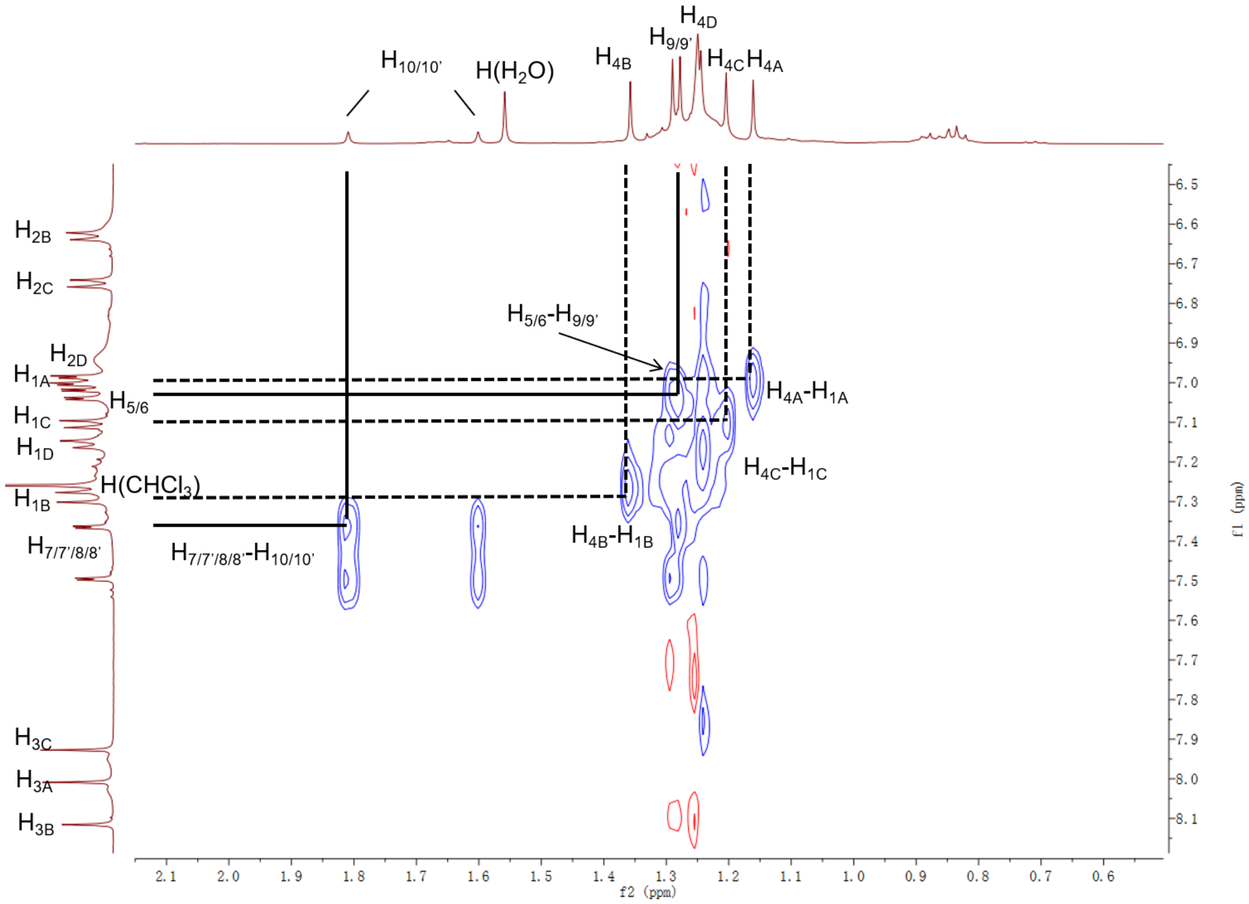

Figure 64. ROESY spectrum of **2** in $CDCl_3$ scaling to the aromatic area on one axis and the alkane area on the other axis. The dashed lines show the proton correlations within one NMI unit, where the solid lines show the proton correlations on the xanthene-phenyl bridge unit.

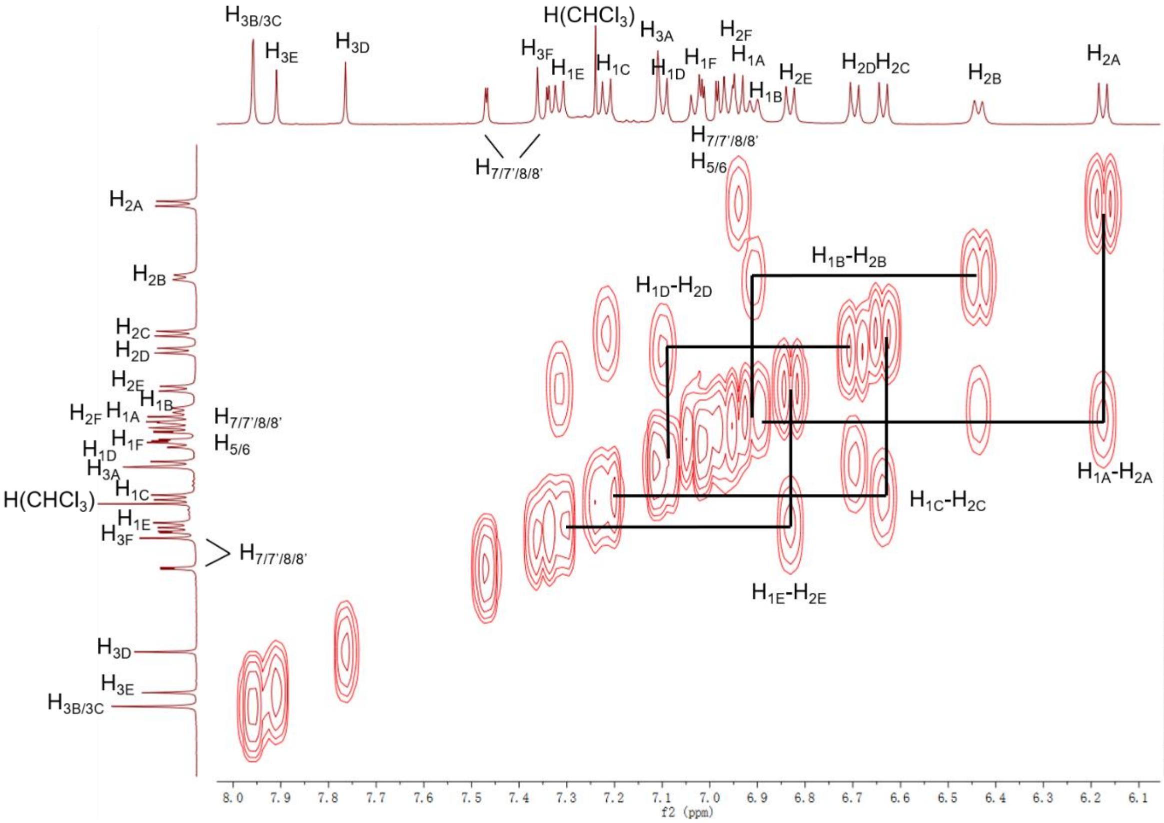

Figure 65. COSY spectrum of **3** in CDCl$_3$ scaling to the aromatic area. The solid lines show the proton correlations between the 1 and 2 positions on the NMI units.

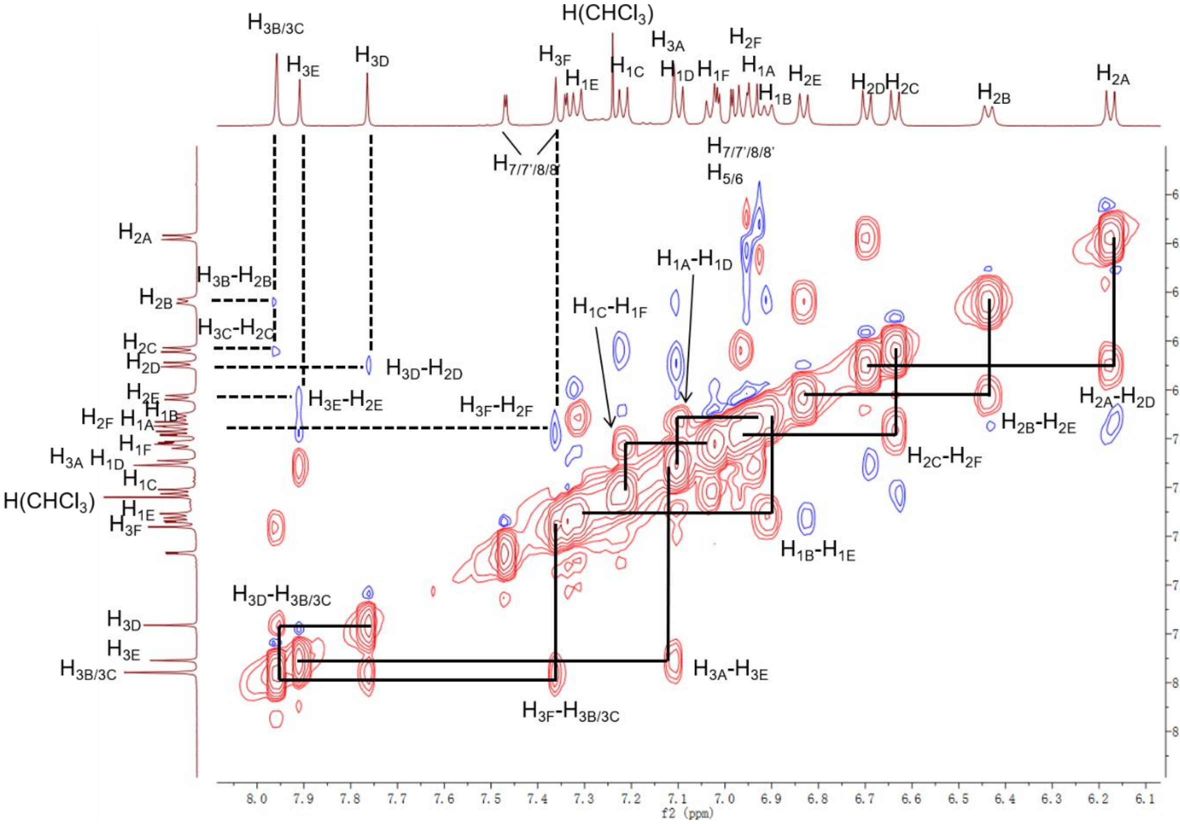

Figure 66. ROESY of **3** in $CDCl_3$ scaling to the aromatic area. The dashed lines show the proton correlations within one NMI unit, where the solid lines show the proton correlations between two different NMI units.

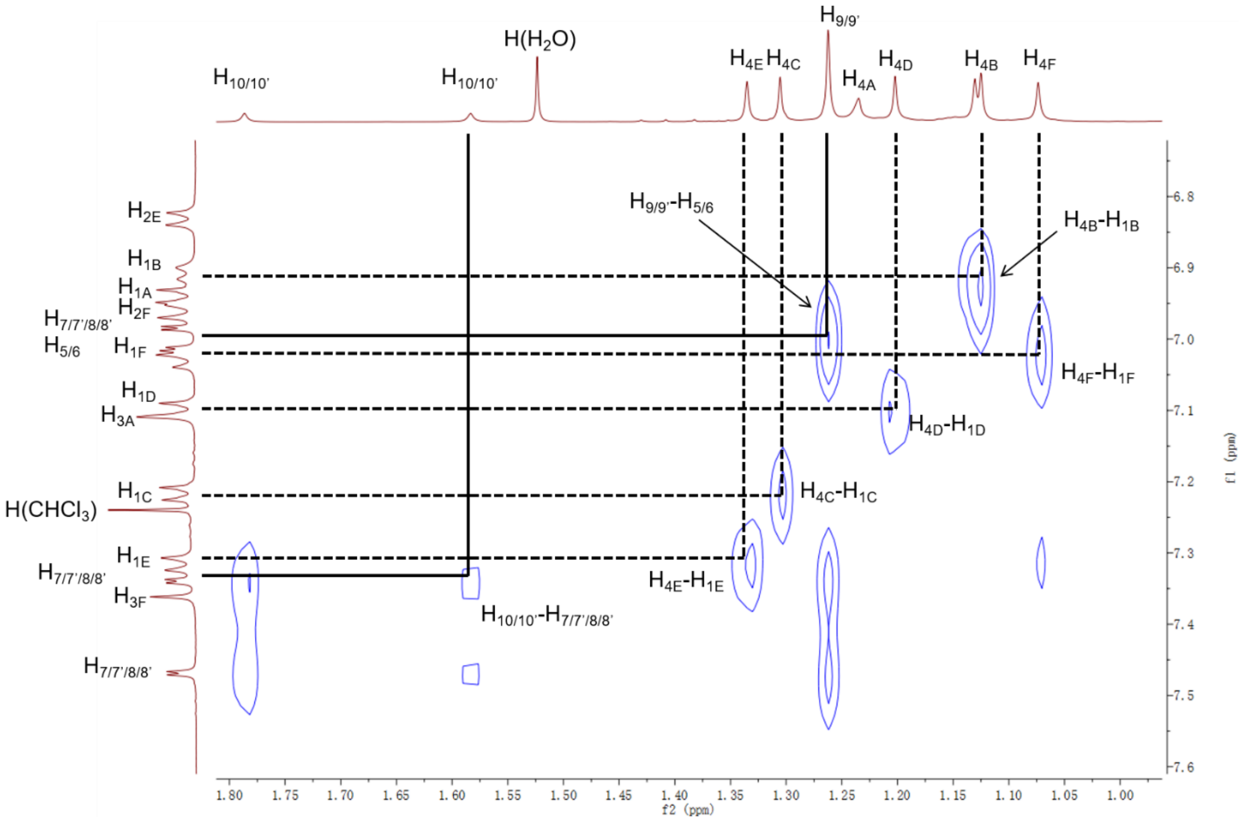

Figure 67. ROESY spectrum of **3** in $CDCl_3$ scaling to the aromatic area on one axis and the alkane area on the other axis. The dashed lines show the proton correlations within one NMI unit, where the solid lines show the proton correlations on the xanthene-phenyl bridge unit.

Chapter 5. Utilizing Mixed Electronic States in Donor-(Acceptor)2 Systems

Photoinduced intramolecular charge transfer (CT) occurs in systems ranging from simple electron donor-acceptor (D-A)[109-113] dyads to systems in which the donor and acceptor are the same molecule and undergo symmetry-breaking charge separation (SB-CS).[4, 50-52, 76-79, 114-121] The use of these molecules as potential functional materials for solar cells depends on achieving fast charge separation rates while maintaining a relatively slow charge recombination (CR) rates.[4] Additionally, synthetic tunability enables the adjustment of the energy levels of the frontier molecular orbitals for better overlap with the charge transporting layers in solar cell applications.

Previously, we reported a null-type slip-stacked perylenediimide (PDI) trimer **PDI_3** that forms a coherent mixed state between the Frenkel exciton (FE) state and the SB-CS state of two of the PDI molecules in ~200 fs after photoexcitation.[4] The mixed state then collapses by transferring a charge to the third PDI chromophore to generate a CS state with the charges on the distal PDIs. While coherent wavepacket analysis,[4] and two-dimensional electronic spectroscopy (2DES)[122] give insights into the formation of the mixed electronic state and its transformation to the symmetry-broken CT state, it is still unclear how the mixed state can be utilized in terms of moving one of the charges generated by SB-CS in a PDI dimer to another electron donor or acceptor.

To address this issue, we have designed a donor-acceptor$_1$-acceptor$_2$ type molecule **Per-PDI_2** (**Figure 68**), where the electron donor perylene is connected to the PDI dimer, which serves as the chromophore pair that can undergo SB-CS. By comparing the photophysics of **Per-PDI_2** to a reference donor-acceptor molecule **Per-PDI** and the **PDI_2** dimer, we observe that the majority of excited states produced by selective photoexcitation of PDI within **Per-PDI_2** result in SB-CS within PDI_2 followed by oxidation of Per to produce the distal $Per^{\bullet+}$-PDI-$PDI^{\bullet-}$ ion pair. This CS process occurs on the picosecond time scale, which is comparable to other PDI oligomer systems.

The CR lifetime of the final CT state is $\tau = 2.4$ ns in both DCM and toluene, which is 30-fold and 2-fold slower, respectively, than for the proximal ion pair Per$^{\bullet+}$-PDI$^{\bullet-}$-PDI in each solvent. Our findings elucidate the utility of mixed electronic states in broader CT processes and provide a general platform to further develop various CT materials suitable for increasing solar cell efficiencies.

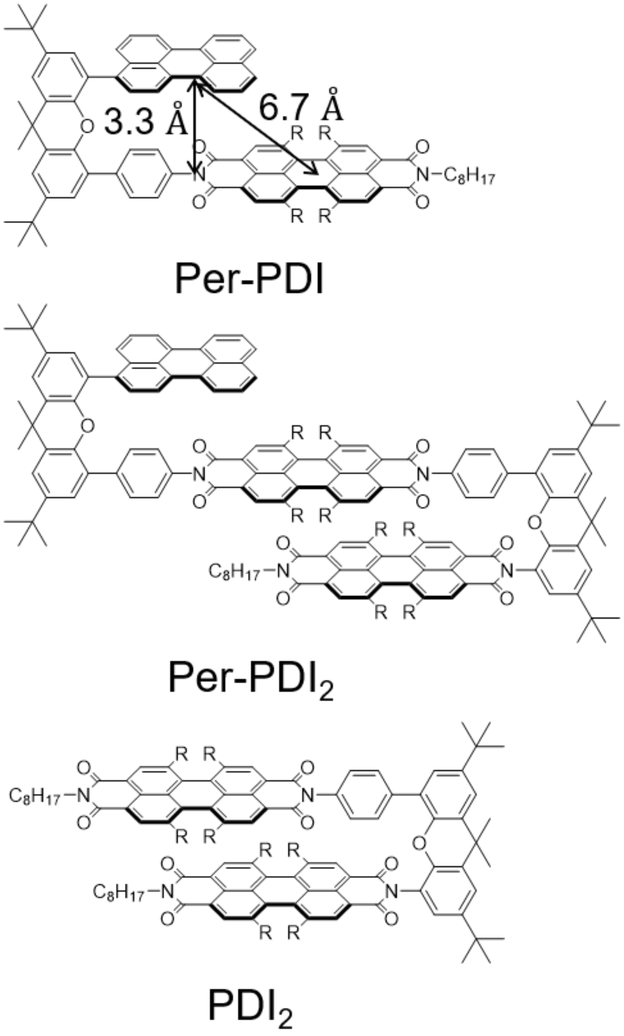

Figure 68. Chemical structures of **Per-PDI**, **Per-PDI$_2$**, and **PDI$_2$** and interchromophoric distances.

Results and Discussion

Synthesis

Per-PDI was synthesized by condensing the perylenemonoimidemonanhydride to the xanthene bridge with the perylene already attached. **Per-PDI$_2$** was synthesized by condensing perylenedianhydride to the xanthene bridge with the perylene attached, then condensing another PDI with the xanthene bridge. Detailed synthetic procedures and characterization of all molecules in this study can be found in the additional data. The synthesis of **PDI$_2$** has been reported previously.[4]

Geometry Optimization

Density functional theory (DFT) optimization (M06-2X/6-31G(d)) of the ground-state geometry (**Figure 73**) of **Per-PDI** shows that the perylene and PDI moieties are slip-stacked as designed with an average π-π distance of 3.3 Å. The center-to-center distance between the perylene and PDI is 6.7 Å.

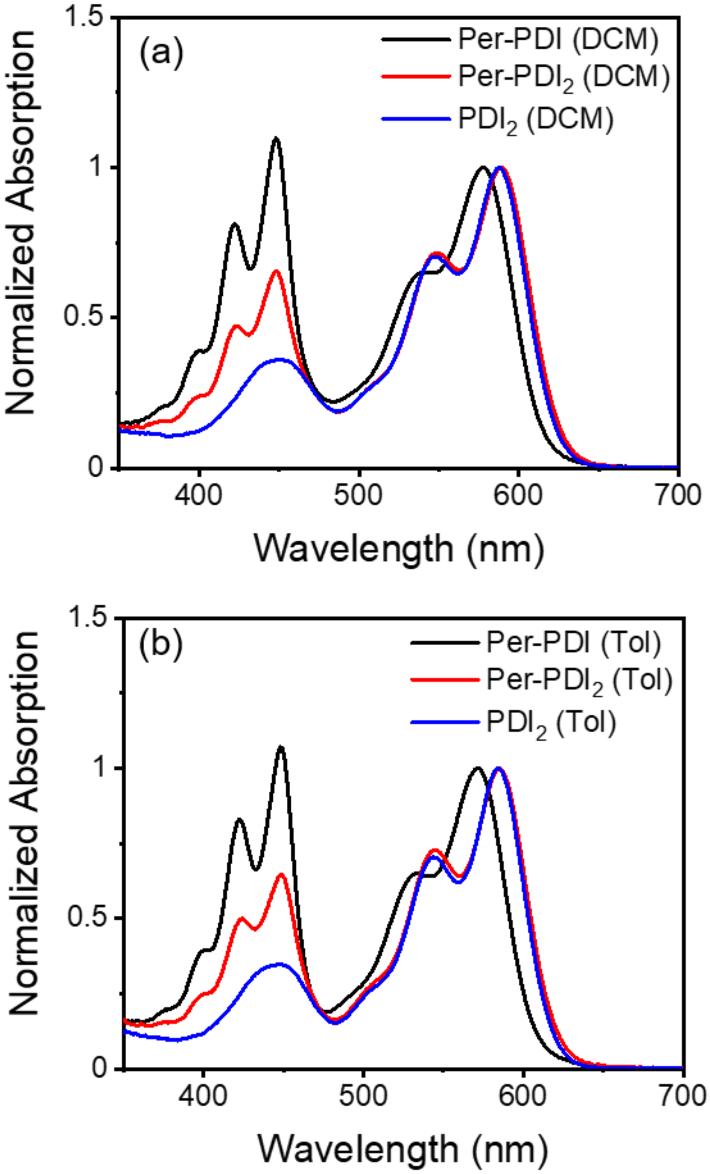

Figure 69. UV-Vis absorption spectra of the three molecules in (a) DCM and (b) toluene.

Steady-State Spectroscopy

Figure 69a shows the comparison of the steady-state absorption spectra of **Per-PDI**, **Per-PDI$_2$**, and **PDI$_2$** in DCM. **Per-PDI** shows distinct vibrational bands of PDI (λ_{0-0} = 578 nm, λ_{0-1} = 537 nm) and Per (λ_{0-0} = 448 nm, λ_{0-1} = 423 nm). **Per-PDI$_2$** also shows distinct vibrational bands of PDI (λ_{0-0} = 588 nm, λ_{0-1} = 548 nm) and perylene (λ_{0-0} = 448 nm, λ_{0-1} = 423 nm). Due to the *J*-type coupling between the PDIs within **PDI$_2$**, the PDI bands are red-shifted compared to **Per-PDI** (λ_{0-0} = 578 nm, λ_{0-1} = 537 nm). The PDI bands of **Per-PDI$_2$** are nearly identical to those in **PDI$_2$**,[4] which means that the coupling between two PDI chromophores is similar between the two molecules. We note that PDI also has a broad absorption band at 450 nm which overlaps with the perylene bands. When exciting the PDI chromophore at 540 nm, **Per-PDI$_2$** shows monomeric PDI emission bands (λ_{0-0} = 615 nm, λ_{0-1} = 665 nm, **Figure 74b**) which are similar to **Per-PDI** (**Figure 74a**) and **PDI$_2$** emission.[4] The fluorescence quantum yield is below the instrument detection threshold, indicating the existence of ultrafast non-radiative decay pathways. The same steady-state measurements were also performed in toluene (**Figure 69b** and **Figure 74b**); the absorption and emission bands are similar to those in DCM, with slight shifts and a higher fluorescence quantum yield (0.04 ± 0.01).

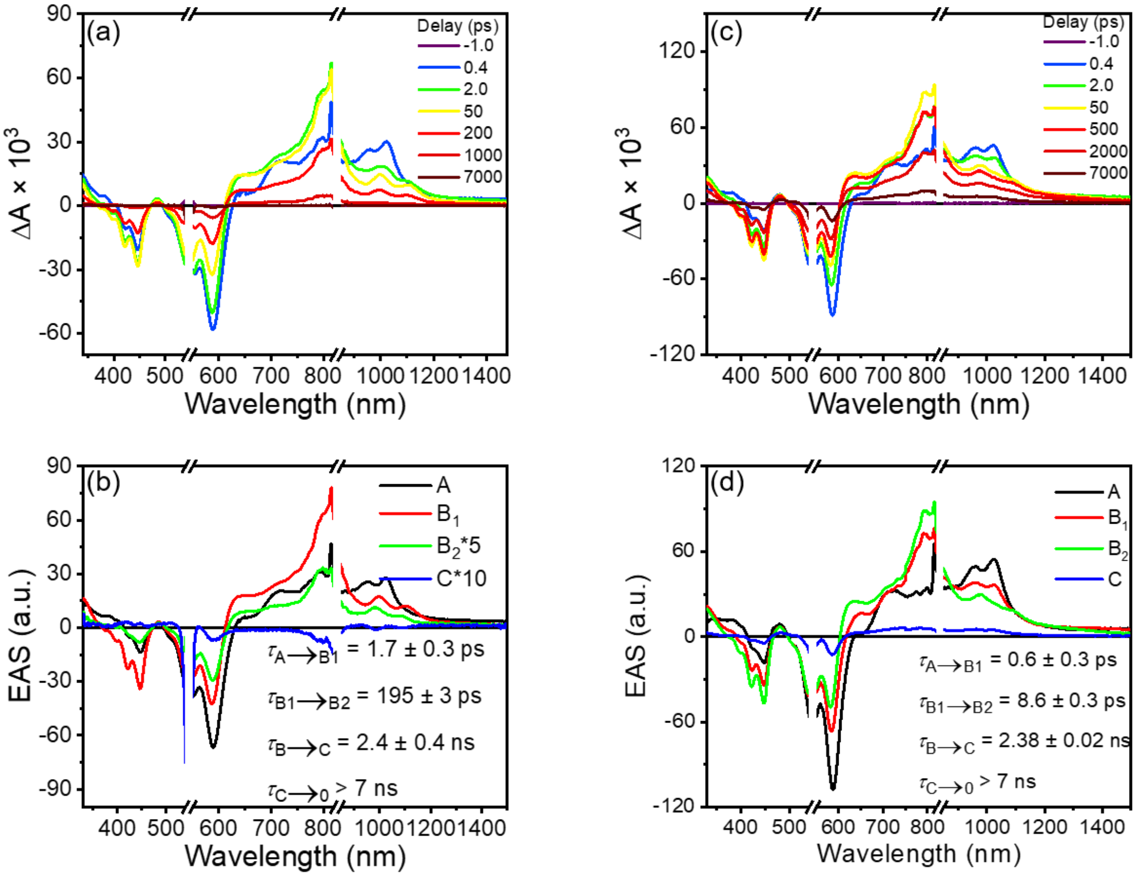

Figure 70. FsTA spectra for **Per-PDI$_2$** at selected decay times in DCM (a) and in toluene (c). Evolution-associated spectra in DCM (b) and in toluene (d) obtained by wavelength global fitting to kinetic model discussed in the text.

Transient Absorption Spectroscopy

To explore the excited-state dynamics, we performed femtosecond transient absorption (fsTA) spectroscopy on **Per-PDI**, **Per-PDI$_2$**, and **PDI$_2$** in both DCM and toluene. Selective photoexcitation of PDI in **Per-PDI** in DCM result in formation of ^{1*}PDI, which results in a ground-state bleach (GSB) at 589 nm and excited-state absorption (ESA) at 706, 956, and 1028 nm. Within the instrument response (IRF = 0.3 ps), electron transfer from Per to ^{1*}PDI results in a hot charge transfer (CT) state (Per$^{\bullet+}$-PDI$^{\bullet-}$) as indicated by the appearance of the PDI$^{\bullet-}$ absorption at 795 nm

(**Figure 75**).[79, 119] We note that pump scatter around 545 nm overlaps with the $\text{Per}^{\bullet+}$ absorption. The hot CT state relaxes in $\tau = 1.5 \pm 0.3$ ps to a state that has similar spectral features, which then decays to ground state in $\tau = 88.4 \pm 0.3$ ps, with no observable long-lived state. In toluene, the decay of the final CT state is slower, occurring in τ=1.26 ± 0.03 ps, in concert with the expectations of electron transfer theory (**Figure 76**).[123-124]

The excited-state dynamics in **Per-PDI$_2$** are significantly different (**Figure 70a,b**). Upon selective photoexcitation of PDI, its GSB appears at 590 nm within the instrument response together with ESA at 714 nm and 640 nm and 790 nm. The 790 nm absorption is characteristic of formation of $\text{PDI}^{\bullet-}$, which suggests that SB-CS occurs within the PDI dimer of **Per-PDI$_2$**. We note that the Per GSB at 447 nm also appears at the same time. Since 545-nm pump selectively excites PDI, we attribute the Per GSB to direct CT from perylene to ^{1*}PDI, as is observed in the photoexcited **Per-PDI** dyad. This secondary pathway competes with SB-CS. After a few picoseconds, the Per GSB and $\text{PDI}^{\bullet-}$ ESA increases along with a decrease of the ^{1*}PDI ESA, indicating the formation of the CT state between the perylene and PDI (state B_1). This CT state experiences some structural relaxation to the relaxed CT state (state B_2), which then undergoes CR partially to the triplet state (state C). The triplet state then lives for microseconds and decays to the ground state as indicated by the nsTA measurements (**Figure 78**). A similar four-step process is also found in toluene (**Figure 70c,d** and **Figure 79**), with faster CS and relaxation rates, and slower CR rates.

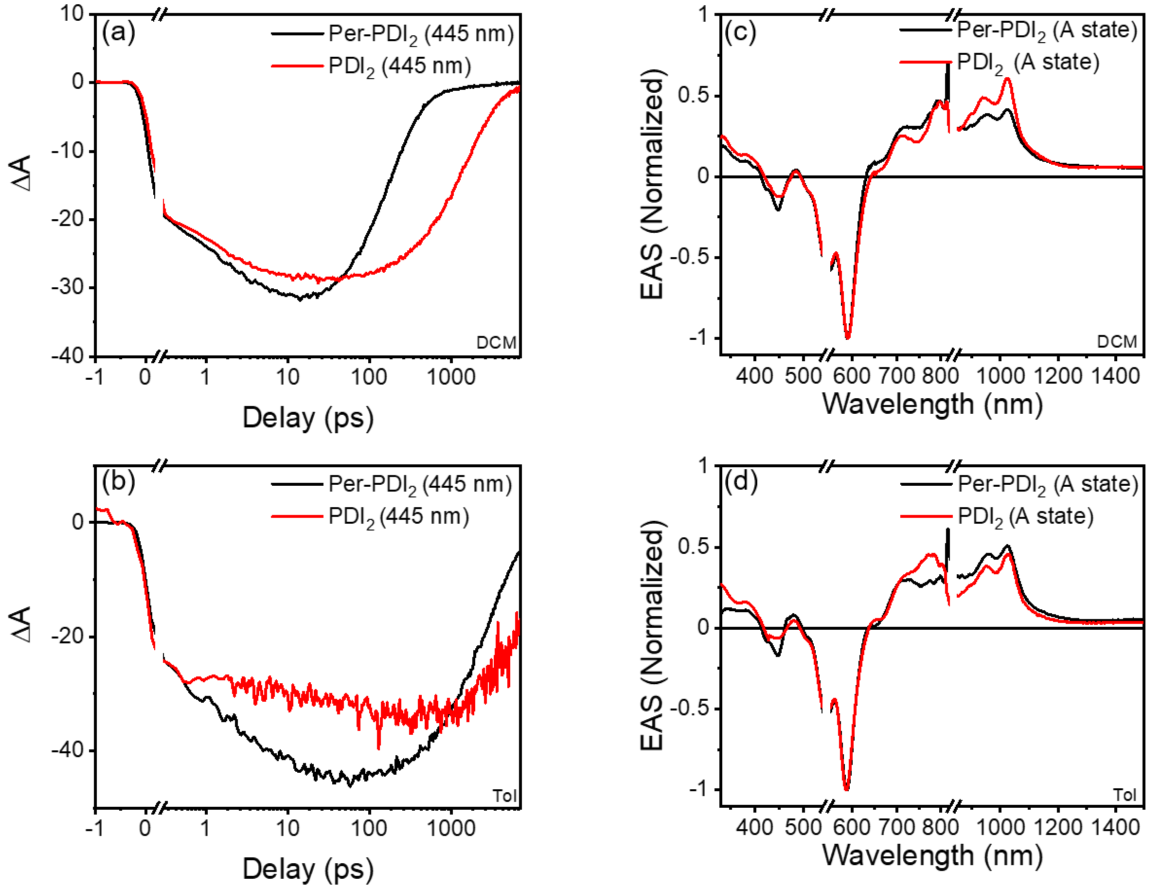

Figure 71. Kinetic traces at 445 nm for **Per-PDI$_2$** (black) and **PDI$_2$** (red) in DCM (a) and in toluene (b). The spectra were scaled to the same intensity at 0.3 ps. Normalized evolution-associated spectra (A state) for **Per-PDI$_2$** (black) and **PDI$_2$** (red) in DCM (c) and in toluene (d).

Excited-state Dynamics

In order to explore the different dynamics between **Per-PDI$_2$** and **PDI$_2$**, we compare the fsTA spectra of the two molecules (**Figure 71**). The Franck-Condon (FC) state of **Per-PDI$_2$** is effectively the delocalized ^{1*}PDI$_2$ state,[72, 89] which is common in PDI oligomer systems, including **PDI$_2$**,[4, 122] but the formation of this state from the localized ^{1*}PDI-PDI state is below the 0.3 ps instrument response. By comparing the GSB at 445 nm where both the Per and PDI ground states absorb (**Figure 71a,b**), it is apparent that the dynamics before 1 ps are similar for the two molecules in both solvents, while the dynamics after 1 ps are significantly different, indicating that the addition of the Per chromophore substantially affects the overall photophysical behavior. Comparing the first EAS (state A) of the two molecules (**Figure 71c,d**), the GSB at 400-500 nm has more structure in **Per-PDI$_2$** than in **PDI$_2$**, which indicates the present of the Per GSB. As discussed above, we attribute this result to a competition between two parallel pathways. The first pathway involves SB-CS within PDI$_2$, which in our previous study occurs in about 200 fs,[4] which is comparable to the second pathway, direct CT from Per to PDI, which occurs in <0.3 ps as indicated by the fsTA data of **Per-PDI**. By fitting the **Per-PDI** spectra (see additional data), the fraction of the population that undergoes SB-CS is 0.80 ± 0.02 in DCM and 0.68 ± 0.02 in toluene. Thus, the majority of the excited states proceed through the SB-CS pathway in both solvents, which demonstrates that SB-CS can initiate CT to a secondary donor or acceptor resulting further separation of charges that can be harvested for applications.

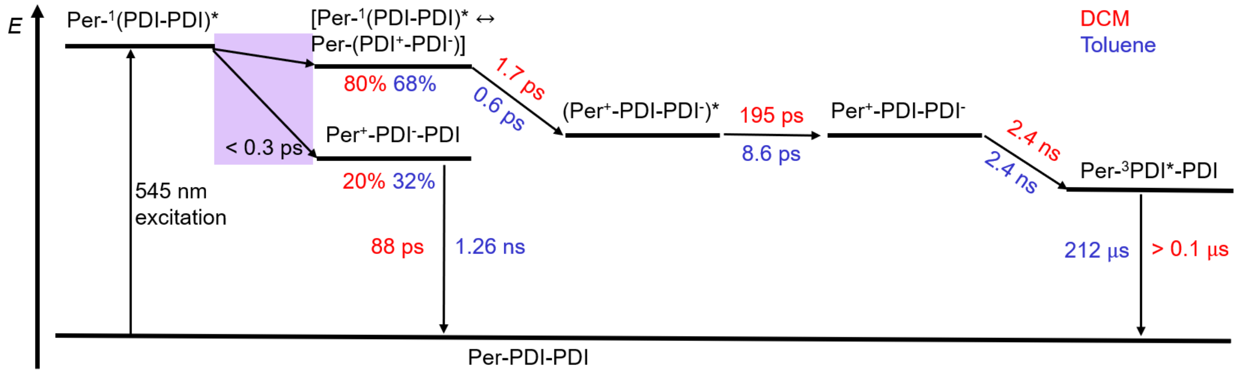

Figure 72. Jablonski diagram for the **Per-PDI$_2$** system. The ratio of the two CT pathways, and the lifetimes of each step are denoted in red for DCM and blue for toluene. The CR lifetimes for Per$^{•+}$-PDI-PDI$^{•-}$ are the effective lifetimes of this state, not strictly the CR lifetimes to the triplet. The CR lifetimes for Per$^{•+}$-PDI$^{•-}$-PDI are taken from the **Per-PDI** data. The energy levels of the different states are arbitrary.

State Assignment and Energy Diagram

As discussed above, state A of **Per-PDI$_2$** decays via two different pathways. The second pathway, which generates Per$^{\bullet+}$-PDI$^{\bullet-}$-PDI, is less likely to proceed through another charge transfer to the outer PDI due to the Coulombic attraction of the opposite charges. On the other hand, the SB-CS pathway generates a dimeric mixed state in the PDI units: [Per-^{1*}(PDI-PDI) ↔ Per-(PDI$^{\bullet+}$-PDI$^{\bullet-}$)],[4] where PDI$^{\bullet+}$ is most likely the inner PDI due its potential stabilization by the adjacent electron-rich Per. The mixed state then collapses to the CT state (state B$_1$) with the charges residing on the outer units (Per$^{\bullet+}$-PDI-PDI$^{\bullet-}$) for three different reasons. First, the CR lifetime of this state is 30-fold longer than lifetime in reference molecule **Per-PDI**. Second, it is kinetically favorable to transfer the partial positive charge from the middle PDI to the perylene, while it is also thermodynamically favorable for the solvent to stabilize the charges when they are on the outer chromophores. Third, the slow CR rates then enable the intersystem crossing to generate the triplet state of PDI (state C) in modest yield. The triplet exciton is localized on the middle PDI (Per-^{3}PDI*-PDI), assuming that the charge mobilities are similar for the electron and the hole. The overall Jablonski diagram can be summarized in **Figure 72**.

In conclusion, building on our previous work on the analogous PDI trimer,[4, 122] we have shown that the charge can be harvested from a PDI dimer that has undergone SB-CS by oxidizing an adjacent electron donor. Following photoexcitation of **Per-PDI$_2$**, femtosecond transient absorption spectroscopy shows that the majority of the excited states undergo SB-CS between the two PDI units. This CT state then oxidizes the adjacent Per to form an ion pair in which the charges reside on the outer units (Per$^{\bullet+}$-PDI-PDI$^{\bullet-}$). This ion pair has a much slower CR rate than does the corresponding ion pair Per$^{\bullet+}$-PDI$^{\bullet-}$ produced on the **Per-PDI** reference molecule in which the charges reside on adjacent molecules. These ideas can be extended to PDI dimers in which both charges resulting from SB-CS can be harvested using appropriate donors and acceptors. In this manner, separating the charge longer distance should increase the charge separation lifetime making it possible for free charge carriers to be produced in functional materials for solar cells based on this strategy.

Methods and Additional Data

Synthesis

Compounds **1**, **6**, **7**, and **9** were synthesized according to existing literature procedures.[4]

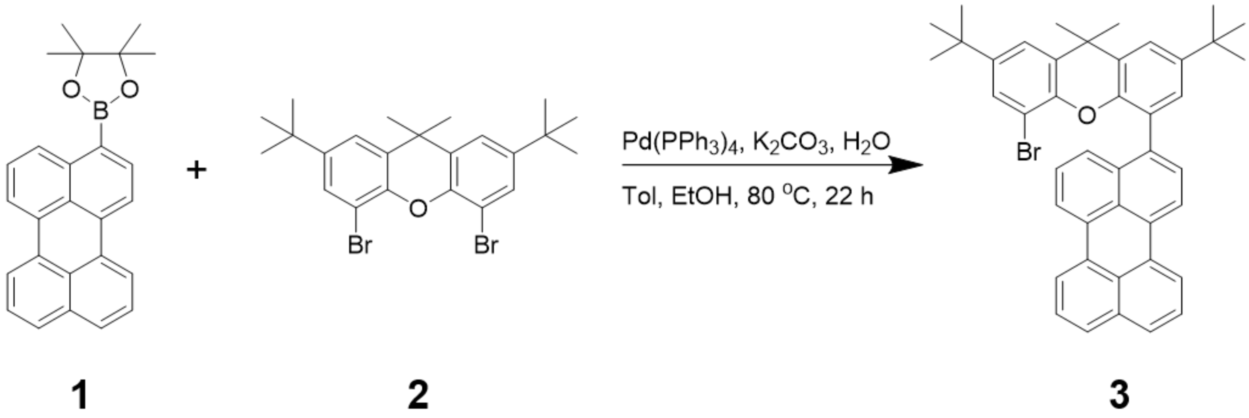

Compound 3. Compound 1 (200 mg, 0.53 mmol), **Compound 2** (385 mg, 0.80 mmol), tetrakis(triphenylphosphine)palladium(0) (40 mg, 0.035 mmol), potassium carbonate (770 mg, 5.6 mmol) were added into a round-bottom flask. The system was degassed and injected with EtOH (3.0 mL), H_2O (3.0 mL) and toluene (60 mL). The system was then heated to 80 °C for 22 h. The crude product was purified by chromatography with hexanes and dichloromethane, and yielded 100 mg (30%) **compound 3**. ^{1}H NMR (500 MHz, $CDCl_3$) δ 8.28 (d, 1H), 8.25 (d, 1H), 8.20 (t, 2H), 7.68 (d, 2H), 7.53 (d, 1H), 7.52 – 7.46 (m, 4H), 7.35 (d, 1H), 7.32 (d, 2H), 7.25 (d, 1H), 1.74 (s, 3H), 1.66 (s, 3H), 1.37 (s, 9H), 1.25 (s, 9H). MALDI-TOF (m/z): calcd. for $C_{43}H_{39}BrO$, 650.22; found, 650.13($[M]^+$)

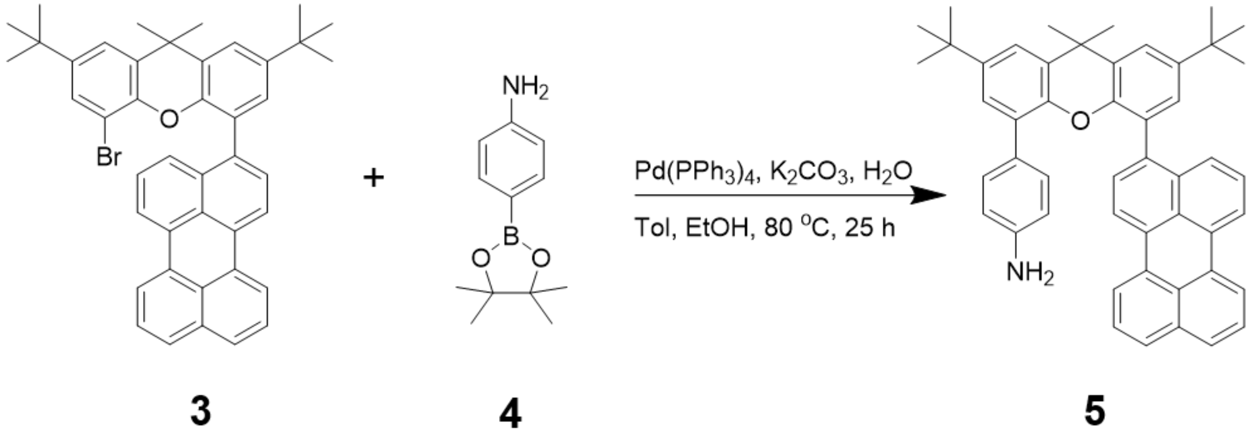

Compound 5. Compound 3 (100 mg, 0.15 mmol), **Compound 4** (52 mg, 0.24 mmol), tetrakis(triphenylphosphine)palladium(0) (9.0 mg, 7.8 µmol), potassium carbonate (67 mg, 0.48 mmol) were added into a round-bottom flask. The system was degassed and injected with EtOH (1.0 mL), H_2O (1.0 mL) and toluene (10 mL). The system was then heated to 80 °C for 25 h. The crude product was purified by chromatography with hexanes and dichloromethane, and yielded 450 mg (44%) **compound 5**. ^1H NMR (500 MHz, $CDCl_3$) δ 8.23 (dd, 2H), 8.10 (dd, 2H), 7.69 (d, 2H), 7.56 – 7.46 (m, 3H), 7.35 – 7.31 (m, 2H), 7.28 (d, 1H), 7.23 (d, 1H), 7.22 – 7.16 (m, 1H), 7.02 (d, 1H), 6.60 (d, 2H), 5.94 (d, 2H), 1.76 (s, 3H), 1.75 (s, 3H), 1.36 (s, 9H), 1.28 (s, 9H). MALDI-TOF (m/z): calcd. for $C_{49}H_{45}NO$, 663.35; found, 663.34($[M]^-$)

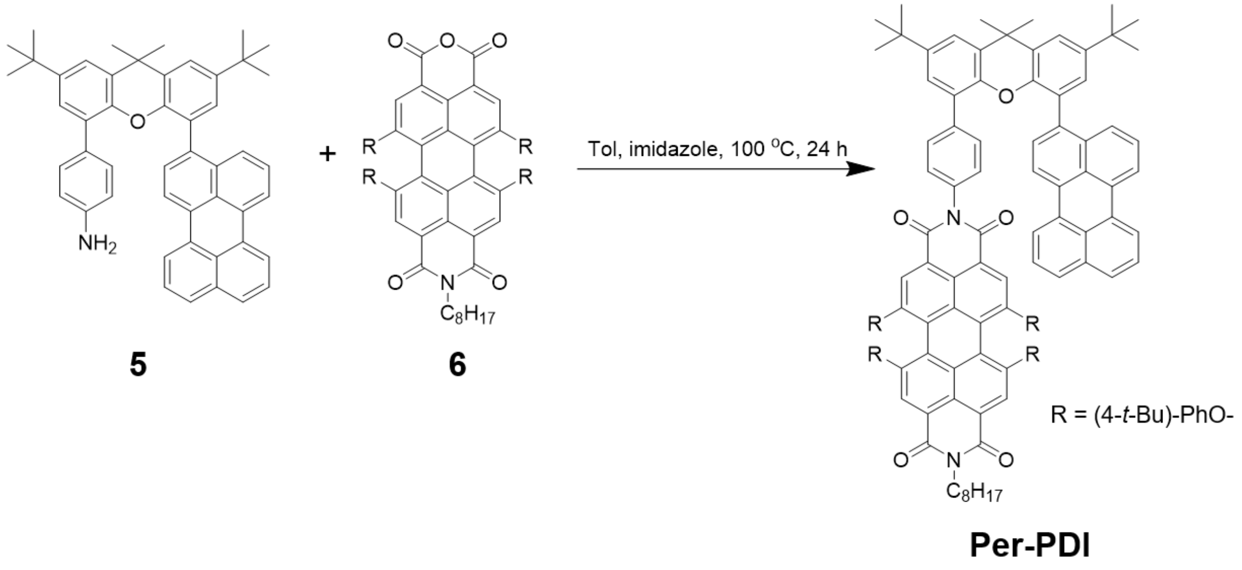

Per-PDI. Compound 5 (8.0 mg, 0.012 mmol), **Compound 6** (20 mg, 0.018 mmol), imidazole (0.5 g) were added into a round-bottom flask. The system was degassed and injected with toluene (5.0 mL). The system was then heated to 100 °C for 24 h. The crude product was purified by chromatography with hexanes and dichloromethane, and yielded 10 mg (48%) **Per-PDI**. ^{1}H NMR (500 MHz, $CDCl_3$) δ 8.32 (s, 2H), 7.88 (s, 2H), 7.50 (d, 1H), 7.41 (d, 2H), 7.27 (t, 8H), 7.17 (s, 1H), 7.15 (d, 1H), 6.94 (s, 6H), 6.89 (d, 12H), 6.47 (d, 2H), 5.83 (s, 2H), 4.14 (m, 2H), 1.77 (s, 3H), 1.51 (s, 3H), 1.36 (s, 9H), 1.36 – 1.24 (m, 12H), 1.34 (s, 9H), 1.30 (d, 36H), 1.24 (m, 3H). MALDI-TOF (m/z): calcd. for $C_{121}H_{116}N_2O_9$, 1740.87; found, 1740.87([M]$^-$)

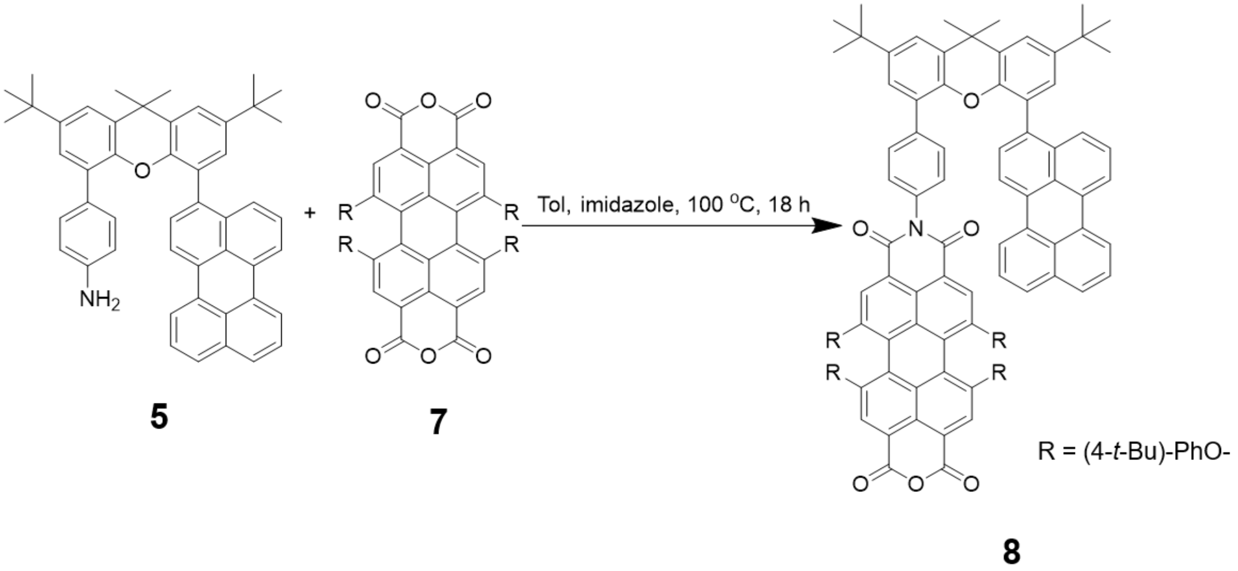

Compound 8. Compound 5 (10 mg, 0.015 mmol), **Compound 7** (20 mg, 0.024 mmol), imidazole (0.5 g) were added into a round-bottom flask. The system was degassed and injected with toluene (5.0 mL). The system was then heated to 100 ^{o}C for 18 h. The crude product was purified by chromatography with hexanes and dichloromethane, and yielded 12 mg (49%) **Compound 8**. The product was confirmed by MALDI and proceeded to the next step without further characterization on NMR. MALDI-TOF (m/z): calcd. for $C_{113}H_{99}NO_{10}$, 1631.03; found, 1629.77([M]$^{-}$).

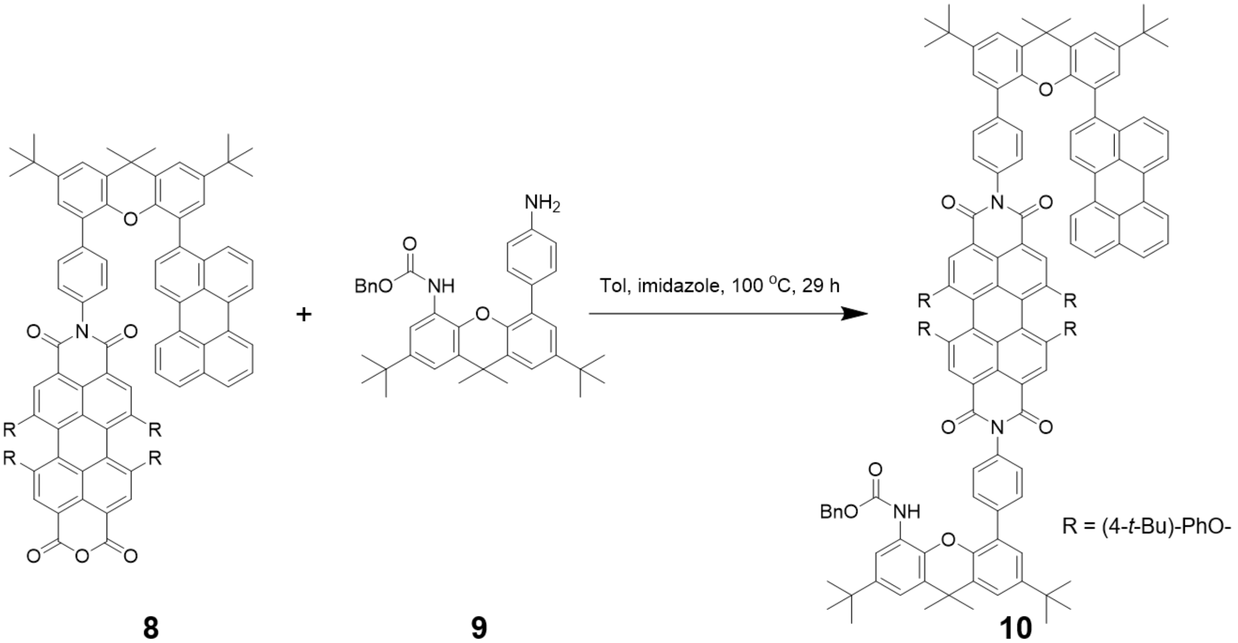

8 **9** **10**

Compound 10. Compound 8 (19 mg, 0.012 mmol), **Compound 9** (10 mg, 0.018 mmol), imidazole (0.5 g) were added into a round-bottom flask. The system was degassed and injected with toluene (5.0 mL). The system was then heated to 100 °C for 29 h. The crude product was purified by chromatography with hexanes and dichloromethane, and yielded 8.0 mg (25%) **Compound 10**. The product was confirmed by MALDI and proceeded to the next step without further characterization on NMR. MALDI-TOF (m/z): calcd. for $C_{150}H_{139}N_3O_{12}$, 2174.04; found, 2174.05($[M]^-$).

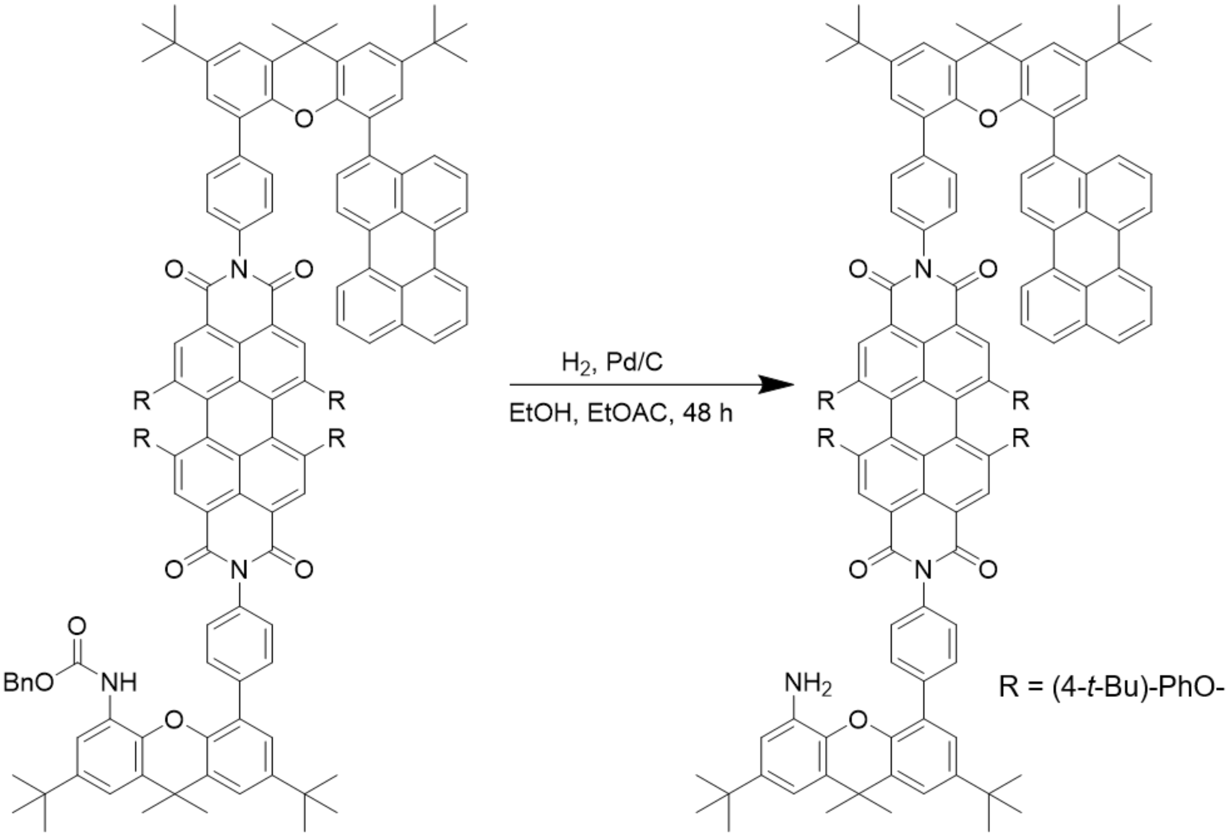

10 **11**

Compound 11. To a solution of **Compound 10** (8 mg, 3.7 μmol) in EtOH (5 mL) and EtOAc (10 mL) in a Parr bottle, was added Pd/C (6.0 mg). The Parr bottle was attached to a Parr hydrogenation apparatus, purged with H_2 (4×55 psi) and then set to shake under H_2 (55 psi) for 48 h. The reaction solution was passed through a celite plug to afford 9 mg of the crude product Compound **11**. The target molecule was confirmed by MALDI and the crude material was carried to the next step without further purification and characterization on NMR. MALDI-TOF (m/z): calcd. for $C_{142}H_{133}N_3O_{10}$, 2040.00; found, 2039.84([M]$^-$).

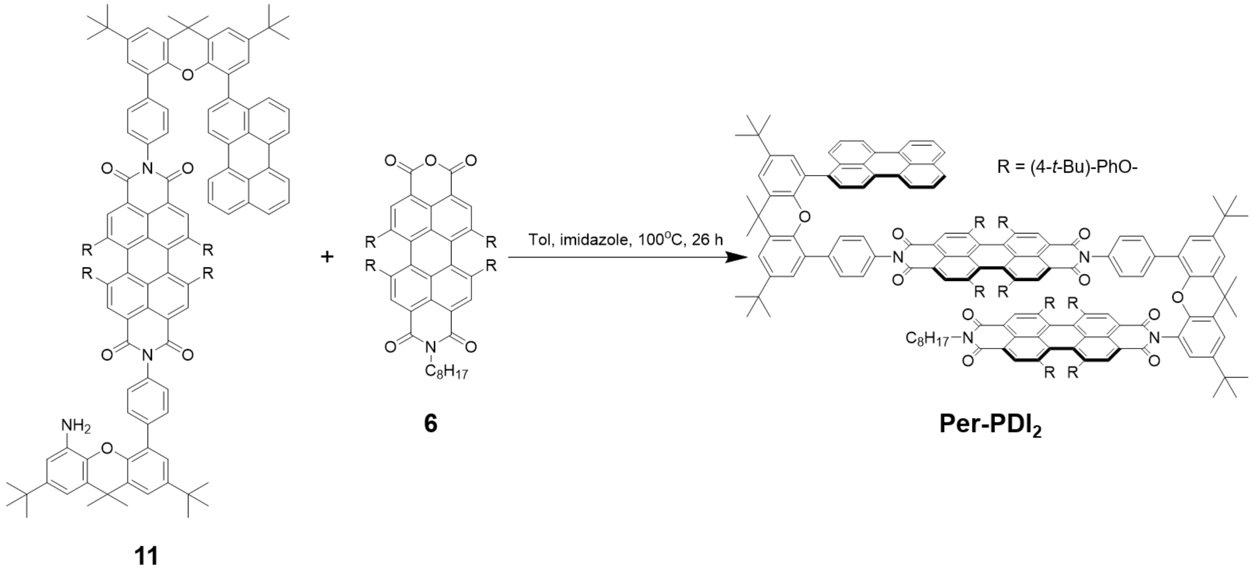

11 **6** **Per-PDI$_2$**

Per-PDI$_2$. Crude **Compound 11** from last step (9 mg, 3.7 µmol if pure), **Compound 6** (16 mg, 0.019 mmol), imidazole (0.5 g) were added into a round-bottom flask. The system was degassed and injected with toluene (5.0 mL). The system was then heated to 100 °C for 26 h. The crude product was purified by chromatography with hexanes and dichloromethane, and yielded 2.0 mg (15%) **Per-PDI$_2$**. MALDI-TOF (m/z): calcd. for $C_{214}H_{204}N_4O_{18}$, 3117.52; found, 3118.00($[M]^-$).

DFT Optimization

Molecular structures of the ground state for **Per-PDI** were optimized using density functional theory (DFT) at the level of M06-2X/6-31G(d) in QChem (version 5.1).[125] To reduce computational costs, the C_8H_{17} was replaced with CH_3 at the imide-position, the *tert*-butyl groups on the phenoxy groups on the bay positions were also replaced with CH_3, and the *tert*-butyl groups and the methyl groups on the xanthene bridge were removed.

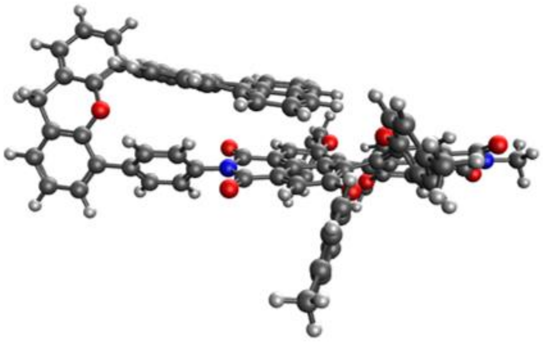

Figure 73. Ground-state optimized structure of **Per-PDI**.

Table 5. Ground-state optimized coordinates of **Per-PDI.**

O	8.16082	0.16767	-0.1295
O	2.36918	2.2673	0.56128
O	2.18877	-2.04852	2.08031
O	-9.06346	1.76025	-0.27579
O	-8.49265	-2.5357	-1.65599
O	-2.5732	-3.50701	1.2219
O	-2.37936	3.48696	-0.50279
O	-4.45216	3.37101	1.02409
O	-3.53172	-3.4224	-1.13616
N	2.31236	0.12227	1.36583
N	-8.78136	-0.38197	-0.96037
C	2.07786	0.33114	-2.31873
C	3.53595	0.51659	-2.17919
C	1.22855	1.37557	-2.63438
C	5.80317	-0.46542	-2.12934
C	7.829	1.0851	-2.28156
C	6.63013	-1.61704	-2.10526
C	0.37013	-3.4828	-1.62912
C	1.76785	-3.31725	-1.59131
C	-0.44461	-2.43436	-1.97545
C	-0.71623	-0.04893	-2.54247
C	6.07746	-2.86961	-2.03164
C	-0.1641	1.18765	-2.75336
C	6.36085	0.84955	-2.17928
C	4.11535	1.76975	-2.14713
C	8.37193	1.70355	-3.41016
C	9.73417	1.98087	-3.49562
C	10.57933	1.6351	-2.44624
C	10.07579	1.00894	-1.30838
C	8.707	0.75507	-1.24293

C	10.93313	0.5733	-0.14317
C	10.14267	0.64616	1.14196
C	8.7696	0.41985	1.07883
C	10.71216	0.92635	2.3822
C	9.92437	0.9704	3.52826
C	8.55309	0.74772	3.43793
C	7.94569	0.47267	2.211
C	6.47777	0.31753	2.07278
C	5.61675	1.26308	2.63648
C	4.24509	1.189	2.42685
C	3.72394	0.1622	1.64592
C	4.56153	-0.81879	1.12447
C	5.92929	-0.73584	1.33501
C	1.626	-1.08389	1.61045
C	0.17903	-1.11021	1.27419
C	-0.48083	0.05265	0.82935
C	0.24243	1.24741	0.64916
C	1.7162	1.28246	0.83394
C	0.11248	-1.15642	-2.22626
C	-0.5156	-2.28049	1.44398
C	-1.87037	-2.35209	1.06466
C	-2.51791	-1.2545	0.48891
C	-1.86104	0.01091	0.52733
C	-2.57218	1.2286	0.26002
C	-1.80141	2.369	0.02742
C	-0.40249	2.37233	0.20964
C	-3.84865	-1.30638	-0.11696
C	-4.63461	-0.11394	-0.09422
C	-4.04546	1.15812	0.21518
C	-4.38469	-2.42924	-0.75027
C	-5.74073	-2.49	-1.1196
C	-6.55783	-1.41153	-0.88462
C	-6.01425	-0.20412	-0.39362
C	-6.84584	0.91854	-0.19764
C	-6.31402	2.0878	0.27794
C	-4.92231	2.21371	0.47584
C	-8.00422	-1.51786	-1.20737
C	-8.30254	0.83221	-0.46529
C	3.82837	-1.94354	-1.99708
C	1.52279	-0.97478	-2.14109
C	-10.21552	-0.43754	-1.23495
C	2.36245	-2.10273	-1.89066
C	4.38561	-0.6301	-2.11103
C	4.68098	-3.03144	-1.97257

C	-2.04012	4.72245	0.01821
C	-4.91873	4.57771	0.53435
C	-2.1575	-4.43017	2.16939
C	-3.85168	-4.74958	-0.96055
C	-2.17277	5.81248	-0.83634
C	-1.96773	7.09283	-0.34258
C	-1.61073	7.30967	0.99283
C	-1.46874	6.19764	1.82127
C	-1.68913	4.90494	1.35092
C	-1.39222	8.70897	1.50916
C	-1.90751	-5.73149	1.75353
C	-1.56466	-6.6881	2.7046
C	-1.45324	-6.36236	4.05792
C	-1.71202	-5.04412	4.44413
C	-2.06882	-4.07646	3.51221
C	-4.71622	-5.20126	0.03382
C	-4.91118	-6.56828	0.18717
C	-4.2565	-7.49927	-0.62521
C	-3.39478	-7.01589	-1.61131
C	-3.19124	-5.6497	-1.7886
C	-4.90944	5.65124	1.41915
C	-5.25249	6.91415	0.95819
C	-5.62795	7.12692	-0.37281
C	-5.64325	6.0296	-1.23231
C	-5.28226	4.75705	-0.79553
C	-5.99849	8.50725	-0.85238
C	-4.48972	-8.97726	-0.44013
C	-1.03659	-7.3966	5.0724
C	5.51116	1.93226	-2.16033
H	5.92964	2.93459	-2.15472
H	4.28129	-4.03798	-1.92097
H	1.62886	2.36937	-2.80197
H	7.70748	-1.49475	-2.14685
H	-0.05953	-4.45161	-1.38804
H	-1.52266	-2.56201	-2.02908
H	-1.79178	-0.2018	-2.60367
H	6.7151	-3.74793	-2.01976
H	-0.79697	2.03809	-2.99042
H	3.49502	2.65742	-2.10571
H	7.70523	1.96594	-4.22625
H	10.13452	2.46302	-4.38131
H	11.64413	1.8467	-2.50576
H	11.8332	1.19289	-0.07601
H	11.27282	-0.45972	-0.30668

H	11.78231	1.10803	2.44392
H	10.37682	1.17998	4.49198
H	7.93224	0.78304	4.3286
H	6.0296	2.09145	3.20502
H	3.58598	1.94879	2.83086
H	4.14587	-1.64132	0.55581
H	6.57917	-1.48715	0.89912
H	-0.00216	-3.15431	1.82978
H	0.1691	3.27017	-0.0013
H	-6.14835	-3.38644	-1.57607
H	-6.96844	2.92946	0.47929
H	-10.44416	-1.43064	-1.61259
H	-10.47547	0.32542	-1.97065
H	-10.77009	-0.23538	-0.31699
H	-2.4683	5.63995	-1.8659
H	-2.09395	7.94444	-1.00686
H	-1.19969	6.33981	2.86503
H	-1.62039	4.05228	2.01813
H	-1.2628	8.7147	2.59475
H	-2.24285	9.3547	1.26724
H	-0.49985	9.16225	1.06457
H	-1.99611	-5.98382	0.70074
H	-1.37726	-7.70987	2.38386
H	-1.63953	-4.77109	5.49378
H	-2.27825	-3.05454	3.81417
H	-5.19664	-4.49254	0.70022
H	-2.87386	-7.71761	-2.25734
H	-2.52124	-5.26909	-2.55339
H	-4.60127	5.48368	2.44571
H	-5.22591	7.75567	1.64634
H	-5.92407	6.16957	-2.27322
H	-5.255	3.92026	-1.48557
H	-6.92252	8.8577	-0.38046
H	-6.15059	8.52243	-1.93491
H	-5.21316	9.23158	-0.6119
H	-4.3921	-9.26366	0.6119
H	-3.77467	-9.56656	-1.01971
H	-5.49683	-9.26119	-0.76381
H	-1.47432	-7.19092	6.05303
H	0.0525	-7.40766	5.19378
H	-1.34379	-8.4001	4.76557
H	2.37945	-4.17318	-1.3292
H	-5.57429	-6.91958	0.97351

Steady-State Spectroscopy

Steady-state absorption and fluorescence spectra were taken on the same instruments mentioned in the previous chapters.

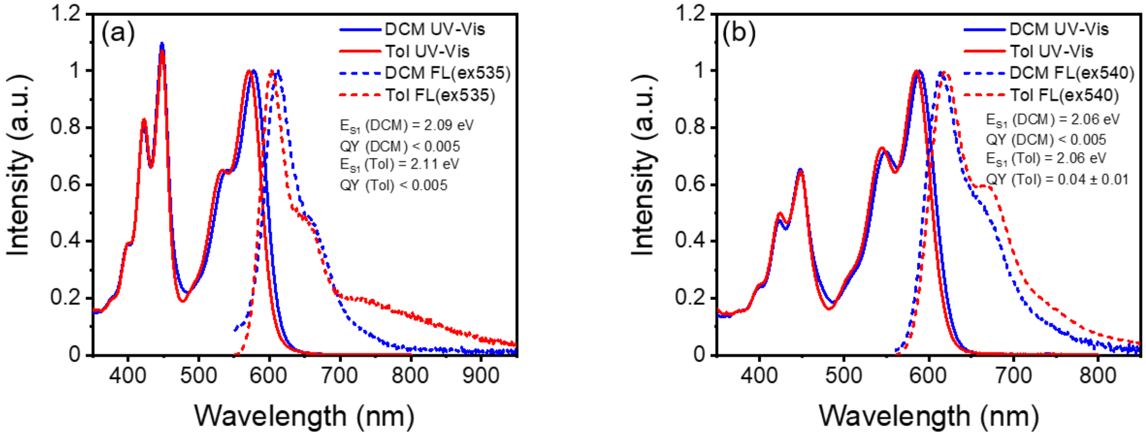

Figure 74. UV-Vis absorption spectra (solid lines) and fluorescence spectra (dashed lines) for Per-PDI (a) and Per-PDI$_2$ (b) in DCM (blue) and toluene (red). The singlet energy (E_{S1}) and the fluorescence quantum yields are denoted in the figure. E_{S1} is taken as the cross point of the absorption and emission spectra.

Transient Absorption Spectroscopy

Femtosecond transient absorption spectroscopy (fsTA) experiments and nanosecond transient absorption spectroscopy (nsTA) experiments were performed on the same instruments mentioned in previous chapters.

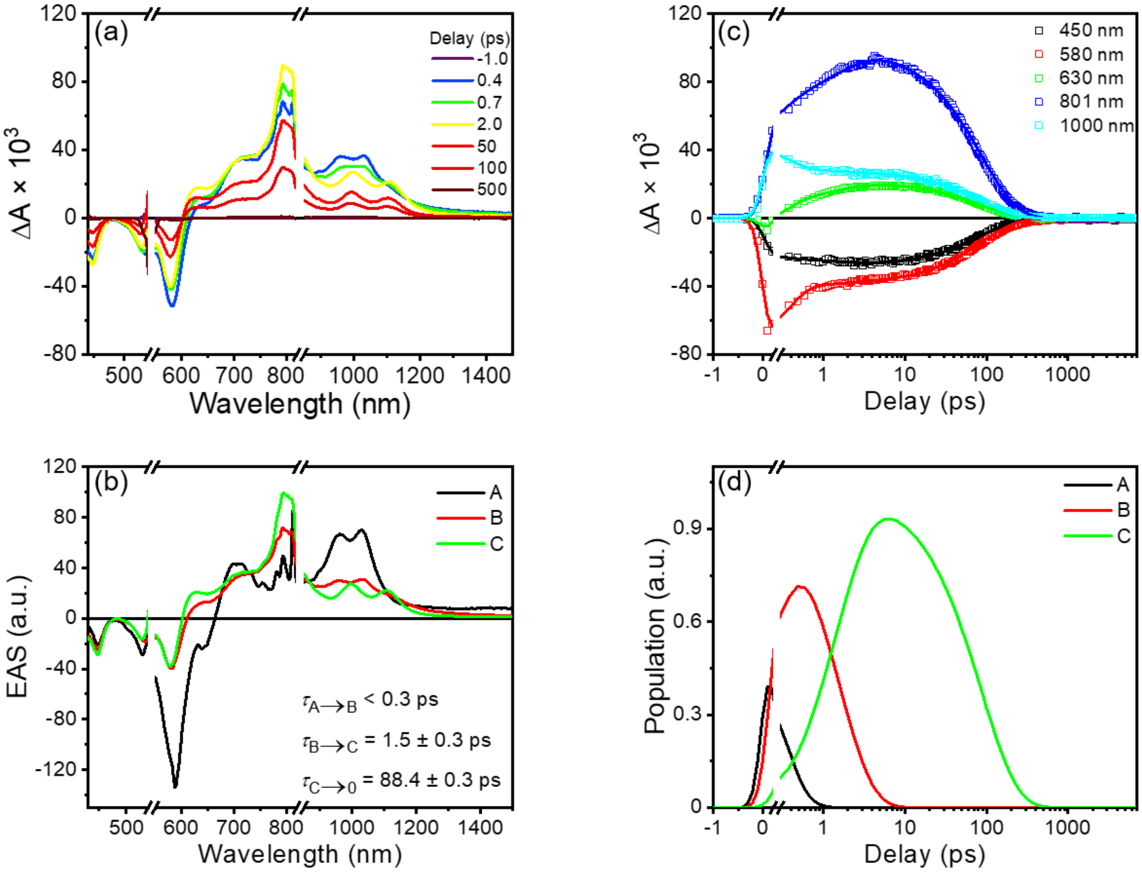

Figure 75. FsTA spectra (ex: 545 nm) of **Per-PDI** in DCM (a) TA spectra at selected delay times. (b) Evolution-associated spectra obtained by wavelength global fitting to an A → B → C → G kinetic model. (c) Kinetic traces at selected wavelengths. (d) Population distribution of the kinetic model.

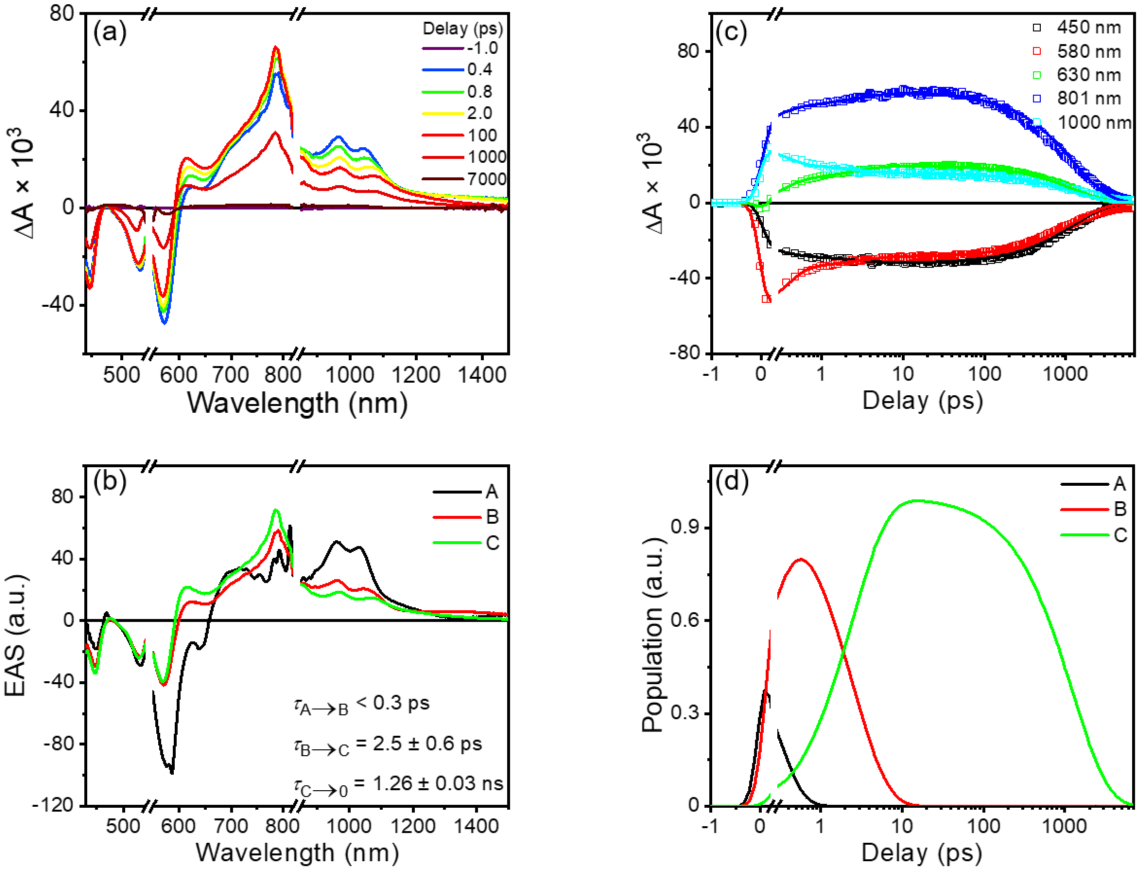

Figure 76. FsTA spectra (ex: 545 nm) of **Per-PDI** in toluene (a) TA spectra at selected delay times. (b) Evolution-associated spectra obtained by wavelength global fitting to an A → B → C → G kinetic model. (c) Kinetic traces at selected wavelengths. (d) Population distribution of the kinetic model.

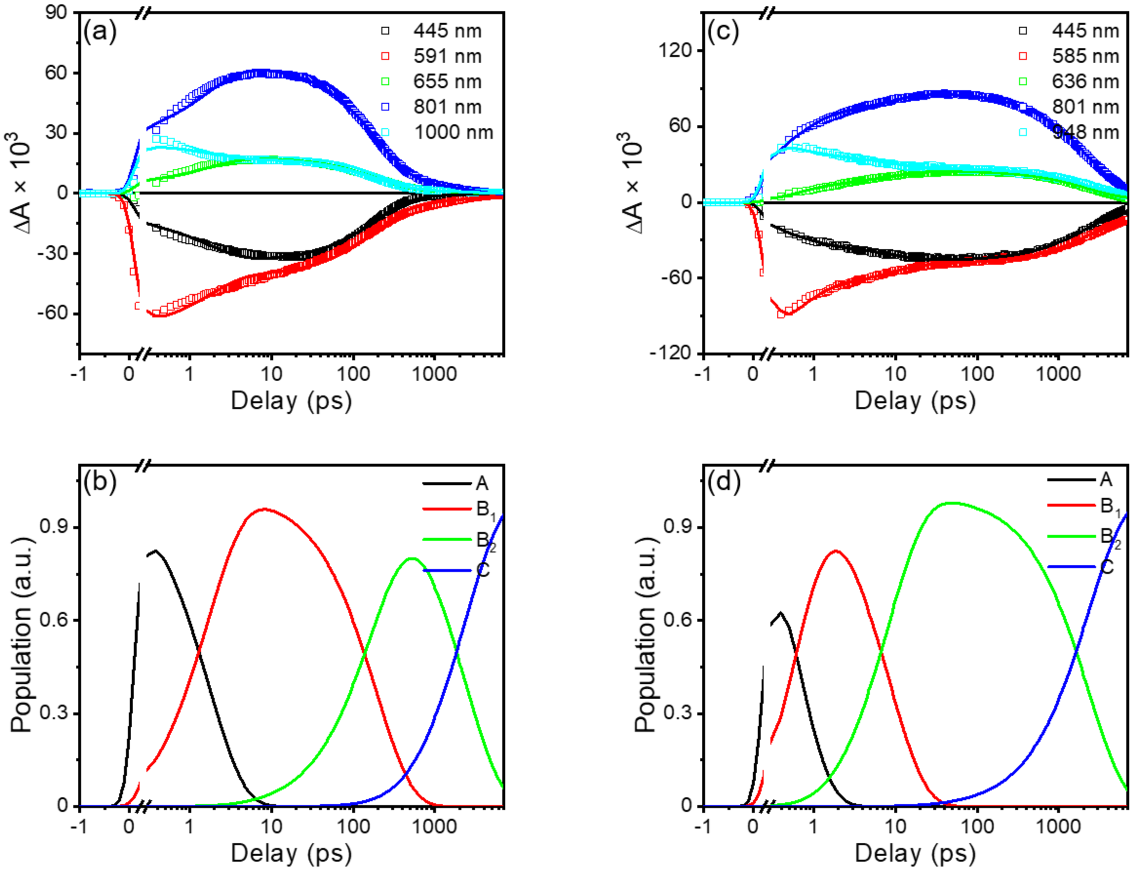

Figure 77. Kinetic traces at selected wavelengths for **Per-PDI$_2$** in DCM (a) and toluene (c). Population distribution of the kinetic model in DCM (b) and toluene (d).

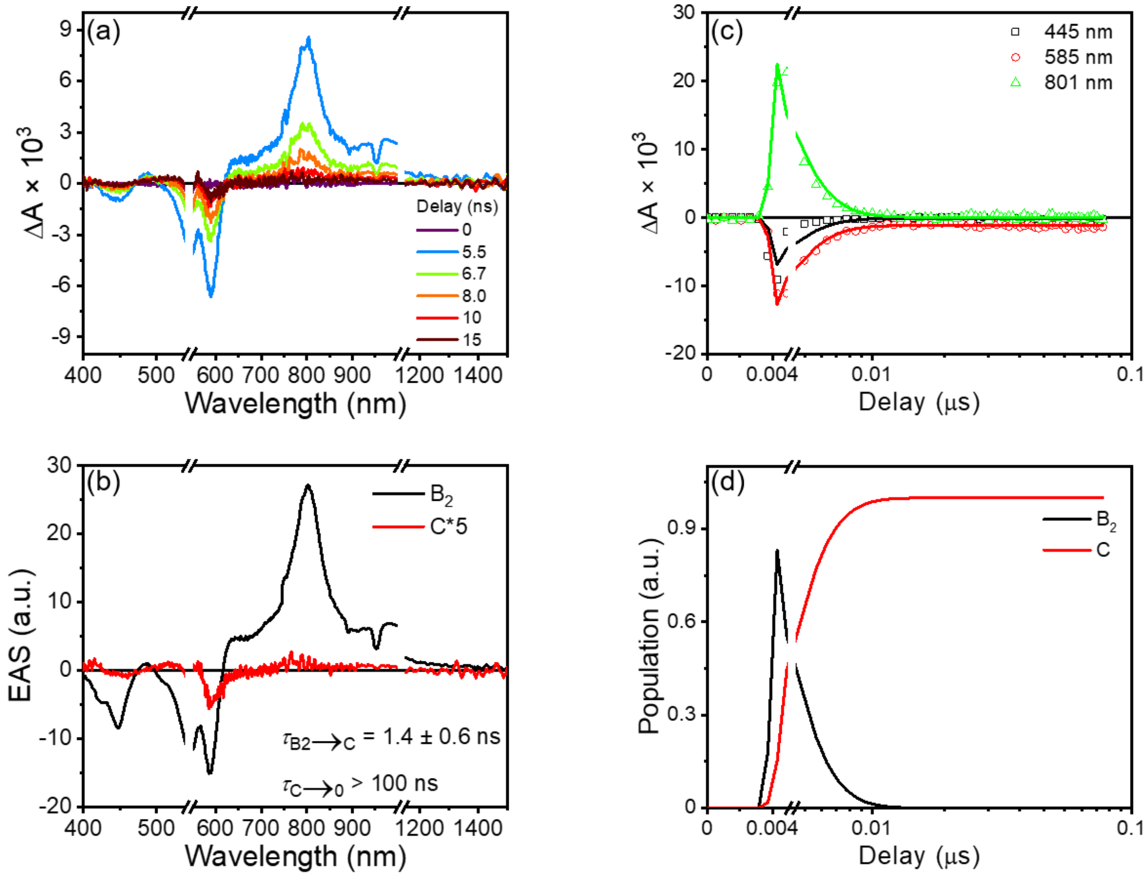

Figure 78. NsTA spectra (ex: 545 nm) of **Per-PDI$_2$** in DCM (a) TA spectra at selected delay times. (b) Evolution-associated spectra obtained by wavelength global fitting to an $B_2 \rightarrow C$ kinetic model. (c) Kinetic traces at selected wavelengths. (d) Population distribution of the kinetic model. The data was cut-off at 80 ns due to the low S/N

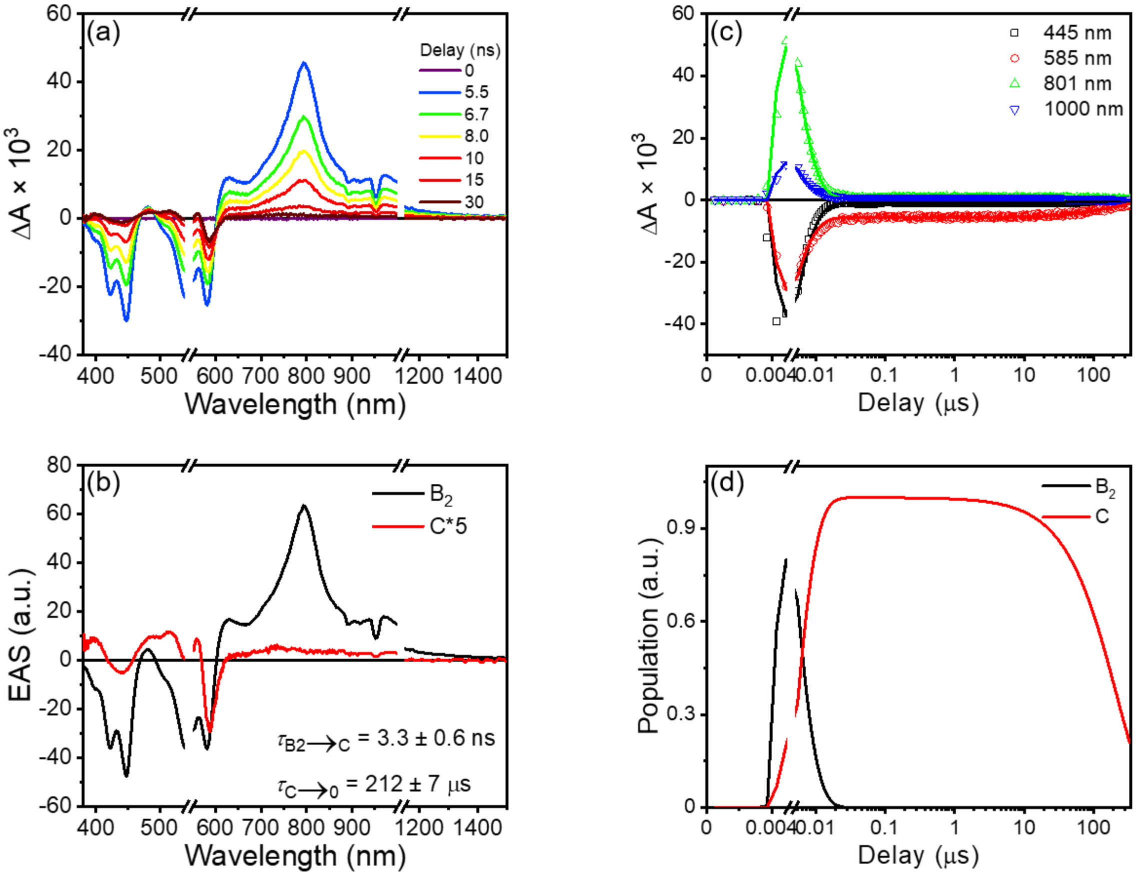

Figure 79. NsTA spectra (ex: 545 nm) of **Per-PDI$_2$** in toluene (a) TA spectra at selected delay times. (b) Evolution-associated spectra obtained by wavelength global fitting to an B$_2$ → C → G kinetic model. (c) Kinetic traces at selected wavelengths. (d) Population distribution of the kinetic model.

Calculation of Ratio between the Indirect and Direct CT Pathways

To calculate the ratio between the indirect and direct CT pathways in **Per-PDI$_2$**, the EAS (State A) of **Per-PDI$_2$** was fitted to the linear combination of two standard spectra: the EAS (State A) of **PDI$_2$**, which represents the indirect pathway; and the EAS (State B$_1$) of **Per-PDI$_2$**, which represents the direct pathway assuming the spectra of Per$^+$-PDI-PDI$^-$ and Per$^+$-PDI$^-$-PDI are similar.

Only the perylene GSB area (400 – 460 nm) were considered to avoid over fitting. The error between the linear combination spectrum and the actual spectrum is defined as the equation below

Equation 6

$$\varepsilon = \sum_{\lambda=400\,nm}^{460\,nm} \left[\frac{\delta \cdot \Delta\mathrm{A}_{\mathrm{PeP}} + (1-\delta) \cdot \Delta\mathrm{A}_{\mathrm{PP}}}{1-0.5\delta} - \Delta\mathrm{A}_{\mathrm{PePP}}\right]^2$$

where ε is the error, δ is the portion of the direct pathway, $\Delta\mathrm{A}_{\mathrm{PeP}}$ is the standard spectrum of the direct pathway normalized to -0.5 at the PDI GSB, $\Delta\mathrm{A}_{\mathrm{PP}}$ is the standard spectrum of the indirect pathway normalized to -1 at the PDI GSB, and $\Delta\mathrm{A}_{\mathrm{PePP}}$ is the actual spectrum of **Per-PDI$_2$** normalized to -1 at the PDI GSB. The different normalizing coefficients come from different numbers of PDI chromophores that are bleached in the states. We note that the overlap of the GSB and ESA may limit the accuracy of this analysis. (1-0.5δ) is the normalizing coefficient for the linearly combined spectrum.

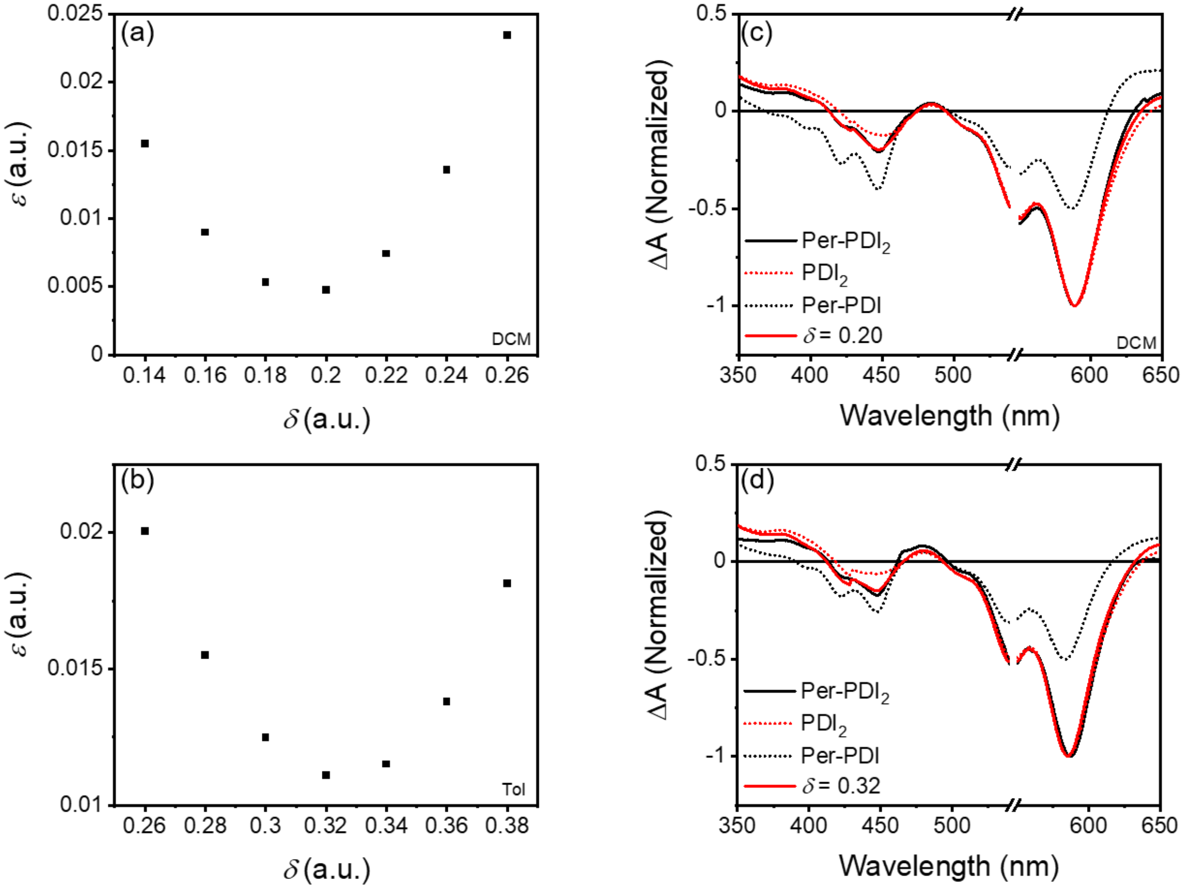

Figure 80. $\varepsilon - \delta$ plots in DCM (a) and toluene (b). Normalized plots of the actual spectra, standard spectra and linearly combined spectra in DCM (c) and toluene (d).

ε is then plotted with δ as shown in **Figure 80a, b** for DCM and toluene, respectively. The δ value with the minimum ε is taken as the portion of the direct pathway. The plotting step size (0.02) of δ is taken as the uncertainty. Finally, the linearly combined spectra are plotted together with the actual spectra as shown in **Figure 80c, d** for DCM and toluene, respectively. They show good agreement even outside the fitting area.

References

(1) Lee, J.; Jadhav, P.; Reusswig, P.D.; Yost, S.R.; Thompson, N.J.; Congreve, D.N.; Hontz, E.; Van Voorhis, T.; Baldo, M.A. Singlet exciton fission photovoltaics *Acc. Chem. Res.* **2013,** *46,* 1300-1311.

(2) Shockley, W.; Queisser, H.J. Detailed balance limit of efficiency of p ‐ n junction solar cells *J. Appl. Phys.* **1961,** *32,* 510-519.

(3) Smith, M.B.; Michl, J. Recent Advances in Singlet Fission *Annu. Rev. Phys. Chem.* **2013,** *64,* 361-386.

(4) Lin, C.; Kim, T.; Schultz, J.D.; Young, R.M.; Wasielewski, M.R. Accelerating symmetry-breaking charge separation in a perylenediimide trimer through a vibronically coherent dimer intermediate *Nat. Chem.* **2022,** *14,* 786-793.

(5) Eaton, S.W.; Shoer, L.E.; Karlen, S.D.; Dyar, S.M.; Margulies, E.A.; Veldkamp, B.S.; Ramanan, C.; Hartzler, D.A.; Savikhin, S.; Marks, T.J.; Wasielewski, M.R. Singlet Exciton Fission in Polycrystalline Thin Films of a Slip-Stacked Perylenediimide *J. Am. Chem. Soc.* **2013,** *135,* 14701-14712.

(6) Roberts, S.T.; McAnally, R.E.; Mastron, J.N.; Webber, D.H.; Whited, M.T.; Brutchey, R.L.; Thompson, M.E.; Bradforth, S.E. Efficient singlet fission discovered in a disordered acene film *J. Am. Chem. Soc.* **2012,** *134,* 6388-6400.

(7) Margulies, E.A.; Kerisit, N.; Gawel, P.; Mauck, C.M.; Ma, L.; Miller, C.E.; Young, R.M.; Trapp, N.; Wu, Y.-L.; Diederich, F.o. Substituent effects on singlet exciton fission in polycrystalline thin films of cyano-substituted diaryltetracenes *J. Phys. Chem. C* **2017,** *121,* 21262-21271.

(8) Congreve, D.N.; Lee, J.; Thompson, N.J.; Hontz, E.; Yost, S.R.; Reusswig, P.D.; Bahlke, M.E.; Reineke, S.; Van Voorhis, T.; Baldo, M.A. External quantum efficiency above 100% in a singlet-exciton-fission–based organic photovoltaic cell *Science* **2013,** *340,* 334-337.

(9) Nakamura, S.; Sakai, H.; Nagashima, H.; Kobori, Y.; Tkachenko, N.V.; Hasobe, T. Quantitative Sequential Photoenergy Conversion Process from Singlet Fission to Intermolecular Two-Electron Transfers Utilizing Tetracene Dimer *ACS Energy Lett.* **2019,** *4,* 26-31.

(10) Smith, M.B.; Michl, J. Singlet fission *Chem. Rev. (Washington, DC, U. S.)* **2010,** *110,* 6891-6936.

(11) Zhao, X.; Bae, Y.J.; Chen, M.; Harvey, S.M.; Lin, C.; Zhou, J.; Schaller, R.D.; Young, R.M.; Wasielewski, M.R. Singlet fission in core-linked terrylenediimide dimers *J. Chem. Phys.* **2020,** *153,* 244306.

(12) Zhao, X.; O'Connor, J.P.; Schultz, J.D.; Bae, Y.J.; Lin, C.; Young, R.M.; Wasielewski, M.R. Temperature Tuning of Coherent Mixing between States Driving Singlet Fission in a Spiro-Fused Terrylenediimide Dimer *J. Phys. Chem. B* **2021,** *125,* 6945-6954.

(13) Fuemmeler, E.G.; Sanders, S.N.; Pun, A.B.; Kumarasamy, E.; Zeng, T.; Miyata, K.; Steigerwald, M.L.; Zhu, X.-Y.; Sfeir, M.Y.; Campos, L.M. A direct mechanism of ultrafast intramolecular singlet fission in pentacene dimers *ACS central science* **2016,** *2,* 316-324.

(14) Hetzer, C.; Guldi, D.M.; Tykwinski, R.R. Pentacene dimers as a critical tool for the investigation of intramolecular singlet fission *Chem. Eur. J.* **2018,** *24,* 8245-8257.

(15) Mauck, C.M.; Hartnett, P.E.; Wu, Y.-L.; Miller, C.E.; Marks, T.J.; Wasielewski, M.R. Singlet Fission within Diketopyrrolopyrrole Nanoparticles in Water *Chem. Mater.* **2017,** *29,* 6810-6817.

(16) Margulies, E.A.; Miller, C.E.; Wu, Y.; Ma, L.; Schatz, G.C.; Young, R.M.; Wasielewski, M.R. Enabling singlet fission by controlling intramolecular charge transfer in π-stacked covalent terrylenediimide dimers *Nat. Chem.* **2016,** *8*, 1120-1125.

(17) Monahan, N.; Zhu, X.-Y. Charge transfer–mediated singlet fission *Annu. Rev. Phys. Chem.* **2015,** *66*, 601-618.

(18) Chen, M.; Bae, Y.J.; Mauck, C.M.; Mandal, A.; Young, R.M.; Wasielewski, M.R. Singlet Fission in Covalent Terrylenediimide Dimers: Probing the Nature of the Multiexciton State Using Femtosecond Mid-Infrared Spectroscopy *J. Am. Chem. Soc.* **2018,** *140*, 9184-9192.

(19) Bae, Y.J.; Kang, G.; Malliakas, C.D.; Nelson, J.N.; Zhou, J.; Young, R.M.; Wu, Y.-L.; Van Duyne, R.P.; Schatz, G.C.; Wasielewski, M.R. Singlet Fission in 9,10-Bis(phenylethynyl)anthracene Thin Films *J. Am. Chem. Soc.* **2018,** *140*, 15140-15144.

(20) Manna, B.; Nandi, A.; Ghosh, R. Ultrafast Singlet Exciton Fission Dynamics in 9,10-Bis(phenylethynyl)anthracene Nanoaggregates and Thin Films *J. Phys. Chem. C* **2018,** *122*, 21047-21055.

(21) Bae, Y.J.; Christensen, J.A.; Kang, G.; Zhou, J.; Young, R.M.; Wu, Y.-L.; Duyne, R.P.V.; Schatz, G.C.; Wasielewski, M.R. Substituent effects on energetics and crystal morphology modulate singlet fission in 9,10-bis(phenylethynyl)anthracenes *J. Chem. Phys.* **2019,** *151*, 044501.

(22) Ullrich, T.; Munz, D.; Guldi, D.M. Unconventional singlet fission materials *Chem. Soc. Rev.* **2021,** *50*, 3485-3518.

(23) Mastron, J.N.; Roberts, S.T.; McAnally, R.E.; Thompson, M.E.; Bradforth, S.E. Aqueous colloidal acene nanoparticles: a new platform for studying singlet fission *J. Phys. Chem. B* **2013,** *117*, 15519-15526.

(24) Sinha, S.K.; Sirota, E.B.; Garoff, S.; Stanley, H.B. X-ray and neutron scattering from rough surfaces *Physical Review B* **1988,** *38*, 2297-2311.

(25) Bae, Y.J.; Shimizu, D.; Schultz, J.D.; Kang, G.; Zhou, J.; Schatz, G.C.; Osuka, A.; Wasielewski, M.R. Balancing Charge Transfer and Frenkel Exciton Coupling Leads to Excimer Formation in Molecular Dimers: Implications for Singlet Fission *J. Phys. Chem. A* **2020,** *124*, 8478-8487.

(26) Mirjani, F.; Renaud, N.; Gorczak, N.; Grozema, F.C. Theoretical Investigation of Singlet Fission in Molecular Dimers: The Role of Charge Transfer States and Quantum Interference *J. Phys. Chem. C* **2014,** *118*, 14192-14199.

(27) Chen, M.; Krzyaniak, M.D.; Nelson, J.N.; Bae, Y.J.; Harvey, S.M.; Schaller, R.D.; Young, R.M.; Wasielewski, M.R. Quintet-triplet mixing determines the fate of the multiexciton state produced by singlet fission in a terrylenediimide dimer at room temperature *Proc. Natl. Acad. Sci. U. S. A.* **2019,** *116*, 8178-8183.

(28) Basel, B.S.; Young, R.M.; Krzyaniak, M.D.; Papadopoulos, I.; Hetzer, C.; Gao, Y.; La Porte, N.T.; Phelan, B.T.; Clark, T.; Tykwinski, R.R.; Wasielewski, M.R.; Guldi, D.M. Influence of the heavy-atom effect on singlet fission: a study of platinum-bridged pentacene dimers *Chem. Sci.* **2019,** *10*, 11130-11140.

(29) Göstl, R.; Sijbesma, R. π-extended anthracenes as sensitive probes for mechanical stress *Chem. Sci.* **2016,** *7*, 370-375.

(30) Young, R.M.; Dyar, S.M.; Barnes, J.C.; Juricek, M.; Stoddart, J.F.; Co, D.T.; Wasielewski, M.R. Ultrafast Conformational Dynamics of Electron Transfer in ExBox4+⊂Perylene *J. Phys. Chem. A* **2013,** *117*, 12438-12448.

(31) Hartnett, P.E.; Margulies, E.A.; Mauck, C.M.; Miller, S.A.; Wu, Y.; Wu, Y.-L.; Marks, T.J.; Wasielewski, M.R. Effects of crystal morphology on singlet exciton fission in diketopyrrolopyrrole thin films *J. Phys. Chem. B* **2016,** *120,* 1357-1366.

(32) Roy, I.; Bobbala, S.; Young, R.M.; Beldjoudi, Y.; Nguyen, M.T.; Cetin, M.M.; Cooper, J.A.; Allen, S.; Anamimoghadam, O.; Scott, E.A.; Wasielewski, M.R.; Stoddart, J.F. A Supramolecular Approach for Modulated Photoprotection, Lysosomal Delivery, and Photodynamic Activity of a Photosensitizer *J. Am. Chem. Soc.* **2019,** *141,* 12296-12304.

(33) Papadopoulos, I.; Gutierrez-Moreno, D.; McCosker, P.M.; Casillas, R.; Keller, P.A.; Sastre-Santos, A.; Clark, T.; Fernandez-Lazaro, F.; Guldi, D.M. Perylene-Monoimides: Singlet Fission Down-Conversion Competes with Up-Conversion by Geminate Triplet-Triplet Recombination *J. Phys. Chem. A* **2020,** *124,* 5727-5736.

(34) Lindquist, R.J.; Lefler, K.M.; Brown, K.E.; Dyar, S.M.; Margulies, E.A.; Young, R.M.; Wasielewski, M.R. Energy Flow Dynamics within Cofacial and Slip-Stacked Perylene-3,4-dicarboximide Dimer Models of π-Aggregates *J. Am. Chem. Soc.* **2014,** *136,* 14912-14923.

(35) Papadopoulos, I.; Gutiérrez-Moreno, D.; Bo, Y.; Casillas, R.; Greißel, P.M.; Clark, T.; Fernández-Lázaro, F.; Guldi, D.M. Altering singlet fission pathways in perylene-dimers; perylene-diimide versus perylene-monoimide *Nanoscale* **2022,** *14,* 5194-5203.

(36) Eaton, S.W.; Shoer, L.E.; Karlen, S.D.; Dyar, S.M.; Margulies, E.A.; Veldkamp, B.S.; Ramanan, C.; Hartzler, D.A.; Savikhin, S.; Marks, T.J.; Wasielewski, M.R. Singlet exciton fission in polycrystalline thin films of a slip-stacked perylenediimide *J. Am. Chem. Soc.* **2013,** *135,* 14701-14712.

(37) Le, A.K.; Bender, J.A.; Roberts, S.T. Slow Singlet Fission Observed in a Polycrystalline Perylenediimide Thin Film *J. Phys. Chem. Lett.* **2016,** *7,* 4922-4928.

(38) Nakazono, S.; Easwaramoorthi, S.; Kim, D.; Shinokubo, H.; Osuka, A. Synthesis of Arylated Perylene Bisimides through C H Bond Cleavage under Ruthenium Catalysis *Org. Lett.* **2009,** *11,* 5426-5429.

(39) Würthner, F.; Saha-Möller, C.R.; Fimmel, B.; Ogi, S.; Leowanawat, P.; Schmidt, D. Perylene Bisimide Dye Assemblies as Archetype Functional Supramolecular Materials *Chem. Rev. (Washington, DC, U. S.)* **2016,** *116,* 962-1052.

(40) Mauck, C.M.; Hartnett, P.E.; Margulies, E.A.; Ma, L.; Miller, C.E.; Schatz, G.C.; Marks, T.J.; Wasielewski, M.R. Singlet Fission via an Excimer-Like Intermediate in 3,6-Bis(thiophen-2-yl)diketopyrrolopyrrole Derivatives *J. Am. Chem. Soc.* **2016,** *138,* 11749-11761.

(41) Bae, Y.J.; Kang, G.; Malliakas, C.D.; Nelson, J.N.; Zhou, J.; Young, R.M.; Wu, Y.-L.; Van Duyne, R.P.; Schatz, G.C.; Wasielewski, M.R. Singlet Fission in 9,10-Bis(phenylethynyl)anthracene Thin Films *J. Am. Chem. Soc.* **2018,** *140,* 15140-15144.

(42) Hartnett, P.E.; Margulies, E.A.; Mauck, C.M.; Miller, S.A.; Wu, Y.; Wu, Y.-L.; Marks, T.J.; Wasielewski, M.R. Effects of Crystal Morphology on Singlet Exciton Fission in Diketopyrrolopyrrole Thin Films *J. Phys. Chem. B* **2016,** *120,* 1357-1366.

(43) Myong, M.S.; Qi, Y.; Stern, C.; Wasielewski, M.R. Ultrafast photo-driven charge transfer exciton dynamics in mixed-stack pyrene-perylenediimide single co-crystals *J. Mater. Chem. C* **2021,** *9,* 16911-16917.

(44) Sheldrick, G.M. SHELXT–Integrated space-group and crystal-structure determination *Acta Crystallographica Section A: Foundations and Advances* **2015,** *71,* 3-8.

(45) Dolomanov, O.V.; Bourhis, L.J.; Gildea, R.J.; Howard, J.A.; Puschmann, H. OLEX2: a complete structure solution, refinement and analysis program *J. Appl. Crystallogr.* **2009,** *42*, 339-341.

(46) Sheldrick, G.M. Crystal structure refinement with SHELXL *Acta Crystallographica Section C: Structural Chemistry* **2015,** *71,* 3-8.

(47) Vincett, P.S.; Voigt, E.M.; Rieckhoff, K.E. Phosphorescence and Fluorescence of Phthalocyanines *J. Chem. Phys.* **1971,** *55,* 4131-4140.

(48) Rihter, B.D.; Kenney, M.E.; Ford, W.E.; Rodgers, M.A.J. Synthesis and photoproperties of diamagnetic octabutoxyphthalocyanines with deep red optical absorbance *J. Am. Chem. Soc.* **1990,** *112,* 8064-8070.

(49) Stuart, A.N.; Tapping, P.C.; Schrefl, E.; Huang, D.M.; Kee, T.W. Controlling the Efficiency of Singlet Fission in TIPS-Pentacene/Polymer Composite Nanoparticles *J. Phys. Chem. C* **2019,** *123,* 5813-5825.

(50) Vauthey, E. Photoinduced symmetry-breaking charge separation *ChemPhysChem* **2012,** *13,* 2001-2011.

(51) Dereka, B.; Vauthey, E. Solute–Solvent Interactions and Excited-State Symmetry Breaking: Beyond the Dipole–Dipole and the Hydrogen-Bond Interactions *J. Phys. Chem. Lett.* **2017,** *8,* 3927-3932.

(52) Dereka, B.; Koch, M.; Vauthey, E. Looking at Photoinduced Charge Transfer Processes in the IR: Answers to Several Long-Standing Questions *Acc. Chem. Res.* **2017,** *50,* 426-434.

(53) Vos, M.H.; Rappaport, F.; Lambry, J.-C.; Breton, J.; Martin, J.-L. Visualization of coherent nuclear motion in a membrane protein by femtosecond spectroscopy *Nature* **1993,** *363,* 320-325.

(54) Romero, E.; Novoderezhkin, V.I.; van Grondelle, R. Quantum design of photosynthesis for bio-inspired solar-energy conversion *Nature* **2017,** *543,* 355-365.

(55) Bartynski, A.N.; Gruber, M.; Das, S.; Rangan, S.; Mollinger, S.; Trinh, C.; Bradforth, S.E.; Vandewal, K.; Salleo, A.; Bartynski, R.A.; Bruetting, W.; Thompson, M.E. Symmetry-breaking charge transfer in a zinc chlorodipyrrin acceptor for high open circuit voltage organic photovoltaics *J. Am. Chem. Soc.* **2015,** *137,* 5397-5405.

(56) Sisson, A.L.; Sakai, N.; Banerji, N.; Fürstenberg, A.; Vauthey, E.; Matile, S. Zipper assembly of vectorial rigid-rod π-stack architectures with red and blue naphthalenediimides: toward supramolecular cascade n/p-heterojunctions *Angew. Chem. Int. Ed.* **2008,** *47,* 3727-3729.

(57) Aratani, N.; Kim, D.; Osuka, A. Discrete cyclic porphyrin arrays as artificial light-harvesting antenna *Acc. Chem. Res.* **2009,** *42,* 1922-1934.

(58) Kaufmann, C.; Kim, W.; Nowak-Krol, A.; Hong, Y.; Kim, D.; Wurthner, F. Ultrafast exciton delocalization, localization, and excimer formation dynamics in a highly defined perylene bisimide quadruple pi-stack *J. Am. Chem. Soc.* **2018,** *140,* 4253-4258.

(59) Kim, T.; Kang, S.; Kirchner, E.; Bialas, D.; Kim, W.; Würthner, F.; Kim, D. Switching resonance character within merocyanine stacks and its impact on excited-state dynamics *Chem* **2021,** *7,* 715-725.

(60) Kasha, M.; Rawls, H.; El-Bayoumi, M.A. The exciton model in molecular spectroscopy *Pure Appl. Chem.* **1965,** *11,* 371-392.

(61) Davydov, A. The theory of molecular excitons *Physics-Uspekhi* **1964,** *7,* 145-178.

(62) Hestand, N.J.; Spano, F.C. Molecular aggregate photophysics beyond the Kasha model: novel design principles for organic materials *Acc. Chem. Res.* **2017,** *50,* 341-350.

(63) Spano, F.C. The spectral signatures of Frenkel polarons in H-and J-aggregates *Acc. Chem. Res.* **2010,** *43,* 429-439.

(64) Oleson, A.; Zhu, T.; Dunn, I.S.; Bialas, D.; Bai, Y.; Zhang, W.; Dai, M.; Reichman, D.R.; Tempelaar, R.; Huang, L.; Spano, F.C. Perylene diimide-based Hj- and hJ-aggregates: the prospect of exciton band shape engineering in organic materials *J. Phys. Chem. C* **2019,** *123,* 20567-20578.

(65) Zubiria-Ulacia, M.; Matxain, J.M.; Casanova, D. The role of CT excitations in PDI aggregates *Phys. Chem. Chem. Phys.* **2020,** *22,* 15908-15918.

(66) Canola, S.; Bagnara, G.; Dai, Y.; Ricci, G.; Calzolari, A.; Negri, F. Addressing the Frenkel and charge transfer character of exciton states with a model Hamiltonian based on dimer calculations: Application to large aggregates of perylene bisimide *J Chem Phys* **2021,** *154,* 124101.

(67) Bialas, D.; Kirchner, E.; Röhr, M.I.S.; Würthner, F. Perspectives in Dye Chemistry: A Rational Approach toward Functional Materials by Understanding the Aggregate State *J. Am. Chem. Soc.* **2021,** *143,* 4500-4518.

(68) Lim, J.M.; Kim, P.; Yoon, M.-C.; Sung, J.; Dehm, V.; Chen, Z.; Würthner, F.; Kim, D. Exciton delocalization and dynamics in helical π-stacks of self-assembled perylene bisimides *Chem. Sci.* **2013,** *4,* 388-397.

(69) Son, M.; Park, K.H.; Shao, C.; Wurthner, F.; Kim, D. Spectroscopic demonstration of exciton dynamics and excimer formation in a sterically controlled perylene bisimide dimer aggregate *J Phys. Chem. Lett.* **2014,** *5,* 3601-3607.

(70) Margulies, E.A.; Shoer, L.E.; Eaton, S.W.; Wasielewski, M.R. Excimer formation in cofacial and slip-stacked perylene-3, 4: 9, 10-bis (dicarboximide) dimers on a redox-inactive triptycene scaffold *Phys. Chem. Chem. Phys.* **2014,** *16,* 23735-23742.

(71) Sung, J.; Kim, P.; Fimmel, B.; Wurthner, F.; Kim, D. Direct observation of ultrafast coherent exciton dynamics in helical pi-stacks of self-assembled perylene bisimides *Nat. Comm.* **2015,** *6,* 8646.

(72) Mauck, C.M.; Young, R.M.; Wasielewski, M.R. Characterization of excimer relaxation via femtosecond shortwave- and mid-infrared spectroscopy *J. Phys. Chem. A* **2017,** *121,* 784-792.

(73) Kim, W.; Nowak-Krol, A.; Hong, Y.; Schlosser, F.; Wurthner, F.; Kim, D. Solvent-modulated charge-transfer resonance enhancement in the excimer state of a bay-substituted perylene bisimide cyclophane *J. Phys. Chem. Lett.* **2019,** *10,* 1919-1927.

(74) Myong, M.S.; Zhou, J.; Young, R.M.; Wasielewski, M.R. Charge-transfer character in excimers of perylenediimides self-assembled on anodic aluminum oxide membrane walls *J. Phys. Chem. C* **2020,** *124,* 4369-4377.

(75) Kang, S.; Kim, T.; Hong, Y.; Wurthner, F.; Kim, D. Charge-delocalized state and coherent vibrational dynamics in rigid PBI H-aggregates *J. Am. Chem. Soc.* **2021,** *143,* 9825-9833.

(76) Giaimo, J.M.; Gusev, A.V.; Wasielewski, M.R. Excited-state symmetry breaking in cofacial and linear dimers of a green perylenediimide chlorophyll analogue leading to ultrafast charge separation *J. Am. Chem. Soc.* **2002,** *124,* 8530-8531.

(77) Sung, J.; Nowak-Krol, A.; Schlosser, F.; Fimmel, B.; Kim, W.; Kim, D.; Wurthner, F. Direct observation of excimer-mediated intramolecular electron transfer in a cofacially-stacked perylene bisimide pair *J. Am. Chem. Soc.* **2016,** *138,* 9029-9032.

(78) Ramirez, C.E.; Chen, S.; Powers-Riggs, N.E.; Schlesinger, I.; Young, R.M.; Wasielewski, M.R. Symmetry-breaking charge separation in the solid state: tetra(phenoxy)perylenediimide polycrystalline films *J. Am. Chem. Soc.* **2020,** *142,* 18243-18250.

(79) Coleman, A.F.; Chen, M.; Zhou, J.; Shin, J.Y.; Wu, Y.; Young, R.M.; Wasielewski, M.R. Reversible Symmetry-Breaking Charge Separation in a Series of Perylenediimide Cyclophanes *J. Phys. Chem. C* **2020,** *124*, 10408-10419.

(80) Farag, M.H.; Krylov, A.I. Singlet fission in perylenediimide dimers *J. Phys. Chem. C* **2018,** *122*, 25753-25763.

(81) Le, A.K.; Bender, J.A.; Arias, D.H.; Cotton, D.E.; Johnson, J.C.; Roberts, S.T. Singlet Fission Involves an Interplay between Energetic Driving Force and Electronic Coupling in Perylenediimide Films *J. Am. Chem. Soc.* **2018,** *140*, 814-826.

(82) Carlotti, B.; Madu, I.K.; Kim, H.; Cai, Z.; Jiang, H.; Muthike, A.K.; Yu, L.; Zimmerman, P.M.; Goodson, T., 3rd Activating intramolecular singlet exciton fission by altering pi-bridge flexibility in perylene diimide trimers for organic solar cells *Chem. Sci.* **2020,** *11*, 8757-8770.

(83) Hong, Y.; Kim, J.; Kim, W.; Kaufmann, C.; Kim, H.; Würthner, F.; Kim, D. Efficient multiexciton state generation in charge-transfer-coupled perylene bisimide dimers via structural control *J. Am. Chem. Soc.* **2020,** *142*, 7845-7857.

(84) Hoche, J.; Schmitt, H.C.; Humeniuk, A.; Fischer, I.; Mitric, R.; Rohr, M.I.S. The mechanism of excimer formation: an experimental and theoretical study on the pyrene dimer *Phys. Chem. Chem. Phys.* **2017,** *19*, 25002-25015.

(85) Hoche, J.; Flock, M.; Miao, X.; Philipp, L.N.; Wenzel, M.; Fischer, I.; Mitric, R. Excimer formation dynamics in the isolated tetracene dimer *Chem. Sci.* **2021,** *12*, 11965-11975.

(86) Mandal, A.; Chen, M.; Foszcz, E.D.; Schultz, J.D.; Kearns, N.M.; Young, R.M.; Zanni, M.T.; Wasielewski, M.R. Two-dimensional electronic spectroscopy reveals excitation energy-dependent state mixing during singlet fission in a terrylenediimide dimer *J. Am. Chem. Soc.* **2018,** *140*, 17907-17914.

(87) Young, R.M.; Wasielewski, M.R. Mixed electronic states in molecular dimers: connecting singlet fission, excimer formation, and symmetry-breaking charge transfer *Acc. Chem. Res.* **2020,** *53*, 1957-1968.

(88) Kistler, K.; Pochas, C.; Yamagata, H.; Matsika, S.; Spano, F. Absorption, circular dichroism, and photoluminescence in perylene diimide bichromophores: Polarization-dependent H-and J-aggregate behavior *J. Phys. Chem. B* **2012,** *116*, 77-86.

(89) Kaufmann, C.; Bialas, D.; Stolte, M.; Wurthner, F. Discrete pi-Stacks of perylene bisimide dyes within folda-dimers: insight into long- and short-range exciton coupling *J. Am. Chem. Soc.* **2018,** *140*, 9986-9995.

(90) Sebastian, E.; Hariharan, M. Null Exciton-Coupled Chromophoric Dimer Exhibits Symmetry-Breaking Charge Separation *J. Am. Chem. Soc.* **2021,** *143*, 13769-13781.

(91) Wu, Y.; Young, R.M.; Frasconi, M.; Schneebeli, S.T.; Spenst, P.; Gardner, D.M.; Brown, K.E.; Wurthner, F.; Stoddart, J.F.; Wasielewski, M.R. Ultrafast photoinduced symmetry-breaking charge separation and electron sharing in perylenediimide molecular triangles *J. Am. Chem. Soc.* **2015,** *137*, 13236-13239.

(92) Fuller, F.D.; Pan, J.; Gelzinis, A.; Butkus, V.; Senlik, S.S.; Wilcox, D.E.; Yocum, C.F.; Valkunas, L.; Abramavicius, D.; Ogilvie, J.P. Vibronic coherence in oxygenic photosynthesis *Nat. Chem.* **2014,** *6*, 706-711.

(93) De Sio, A.; Troiani, F.; Maiuri, M.; Rehault, J.; Sommer, E.; Lim, J.; Huelga, S.F.; Plenio, M.B.; Rozzi, C.A.; Cerullo, G.; Molinari, E.; Lienau, C. Tracking the coherent generation of polaron pairs in conjugated polymers *Nat. Comm.* **2016,** *7*, 13742.

(94) Bakulin, A.A.; Morgan, S.E.; Kehoe, T.B.; Wilson, M.W.; Chin, A.W.; Zigmantas, D.; Egorova, D.; Rao, A. Real-time observation of multiexcitonic states in ultrafast singlet fission using coherent 2D electronic spectroscopy *Nat. Chem.* **2016,** *8*, 16-23.

(95) De Sio, A.; Lienau, C. Vibronic coupling in organic semiconductors for photovoltaics *Phys. Chem. Chem. Phys.* **2017,** *19*, 18813-18830.

(96) Stern, H.L.; Cheminal, A.; Yost, S.R.; Broch, K.; Bayliss, S.L.; Chen, K.; Tabachnyk, M.; Thorley, K.; Greenham, N.; Hodgkiss, J.M.; Anthony, J.; Head-Gordon, M.; Musser, A.J.; Rao, A.; Friend, R.H. Vibronically coherent ultrafast triplet-pair formation and subsequent thermally activated dissociation control efficient endothermic singlet fission *Nat. Chem.* **2017,** *9*, 1205-1212.

(97) Miyata, K.; Kurashige, Y.; Watanabe, K.; Sugimoto, T.; Takahashi, S.; Tanaka, S.; Takeya, J.; Yanai, T.; Matsumoto, Y. Coherent singlet fission activated by symmetry breaking *Nat. Chem.* **2017,** *9*, 983-989.

(98) Gaynor, J.D.; Sandwisch, J.; Khalil, M. Vibronic coherence evolution in multidimensional ultrafast photochemical processes *Nat. Comm.* **2019,** *10*, 5621.

(99) Arsenault, E.A.; Bhattacharyya, P.; Yoneda, Y.; Fleming, G.R. Two-dimensional electronic-vibrational spectroscopy: Exploring the interplay of electrons and nuclei in excited state molecular dynamics *J. Chem. Phys.* **2021,** *155*, 020901.

(100) Schultz, J.D.; Shin, J.Y.; Chen, M.; O'Connor, J.P.; Young, R.M.; Ratner, M.A.; Wasielewski, M.R. Influence of Vibronic Coupling on Ultrafast Singlet Fission in a Linear Terrylenediimide Dimer *J. Am. Chem. Soc.* **2021,** *143*, 2049-2058.

(101) Halpin, A.; Johnson, P.J.M.; Tempelaar, R.; Murphy, R.S.; Knoester, J.; Jansen, T.L.C.; Miller, R.J.D. Two-dimensional spectroscopy of a molecular dimer unveils the effects of vibronic coupling on exciton coherences *Nat. Chem.* **2014,** *6*, 196-201.

(102) Lim, J.; Paleček, D.; Caycedo-Soler, F.; Lincoln, C.N.; Prior, J.; von Berlepsch, H.; Huelga, S.F.; Plenio, M.B.; Zigmantas, D.; Hauer, J. Vibronic origin of long-lived coherence in an artificial molecular light harvester *Nat. Comm.* **2015,** *6*, 7755.

(103) Christensson, N.; Kauffmann, H.F.; Pullerits, T.; Mančal, T. Origin of Long-Lived Coherences in Light-Harvesting Complexes *J. Phys. Chem. B* **2012,** *116*, 7449-7454.

(104) Kim, W.; Kim, T.; Kang, S.; Hong, Y.; Würthner, F.; Kim, D. Tracking Structural Evolution during Symmetry-Breaking Charge Separation in Quadrupolar Perylene Bisimide with Time-Resolved Impulsive Stimulated Raman Spectroscopy *Angew. Chem. Int. Ed.* **2020,** *59*, 8571-8578.

(105) Rafiq, S.; Fu, B.; Kudisch, B.; Scholes, G.D. Interplay of vibrational wavepackets during an ultrafast electron transfer reaction *Nat. Chem.* **2021,** *13*, 70-76.

(106) Kim, P.; Valentine, A.J.S.; Roy, S.; Mills, A.W.; Chakraborty, A.; Castellano, F.N.; Li, X.; Chen, L.X. Ultrafast excited-state dynamics of photoluminescent Pt(II) dimers probed by a coherent vibrational wavepacket *J. Phys. Chem. Lett.* **2021,** *12*, 6794-6803.

(107) Rafiq, S.; Scholes, G.D. From Fundamental Theories to Quantum Coherences in Electron Transfer *J. Am. Chem. Soc.* **2019,** *141*, 708-722.

(108) Connelly, N.G.; Geiger, W.E. Chemical redox agents for organometallic chemistry *Chem. Rev. (Washington, DC, U. S.)* **1996,** *96*, 877-910.

(109) Wasielewski, M.R. Photoinduced electron transfer in supramolecular systems for artificial photosynthesis *Chem. Rev. (Washington, DC, U. S.)* **1992,** *92*, 435-461.

(110) Gaines III, G.L.; O'Neil, M.P.; Svec, W.A.; Niemczyk, M.P.; Wasielewski, M.R. Photoinduced electron transfer in the solid state: Rate vs. free energy dependence in fixed-distance porphyrin-acceptor molecules *J. Am. Chem. Soc.* **1991,** *113*, 719-721.

(111) Ward, M.D. Photo-induced electron and energy transfer in non-covalently bonded supramolecular assemblies *Chem. Soc. Rev.* **1997,** *26,* 365-375.

(112) Frischmann, P.D.; Mahata, K.; Würthner, F. Powering the future of molecular artificial photosynthesis with light-harvesting metallosupramolecular dye assemblies *Chem. Soc. Rev.* **2013,** *42,* 1847-1870.

(113) Gust, D.; Moore, T.A.; Moore, A.L. Solar fuels via artificial photosynthesis *Acc. Chem. Res.* **2009,** *42,* 1890-1898.

(114) Vauthey, E. Photoinduced Symmetry ‐ Breaking Charge Separation *ChemPhysChem* **2012,** *13,* 2001-2011.

(115) Markovic, V.; Villamaina, D.; Barabanov, I.; Lawson Daku, L.M.; Vauthey, E. Photoinduced Symmetry ‐ Breaking Charge Separation: The Direction of the Charge Transfer *Angew. Chem.* **2011,** *123,* 7738-7740.

(116) Sung, J.; Nowak-Król, A.; Schlosser, F.; Fimmel, B.; Kim, W.; Kim, D.; Würthner, F. Direct observation of excimer-mediated intramolecular electron transfer in a cofacially-stacked perylene bisimide pair *J. Am. Chem. Soc.* **2016,** *138,* 9029-9032.

(117) Powers-Riggs, N.E.; Zuo, X.; Young, R.M.; Wasielewski, M.R. Symmetry-breaking charge separation in a nanoscale terrylenediimide guanine-quadruplex assembly *J. Am. Chem. Soc.* **2019,** *141,* 17512-17516.

(118) Piet, J.J.; Schuddeboom, W.; Wegewijs, B.R.; Grozema, F.C.; Warman, J.M. Symmetry breaking in the relaxed S1 excited state of bianthryl derivatives in weakly polar solvents *J. Am. Chem. Soc.* **2001,** *123,* 5337-5347.

(119) Wu, Y.; Young, R.M.; Frasconi, M.; Schneebeli, S.T.; Spenst, P.; Gardner, D.M.; Brown, K.E.; Würthner, F.; Stoddart, J.F.; Wasielewski, M.R. Ultrafast photoinduced symmetry-breaking charge separation and electron sharing in perylenediimide molecular triangles *J. Am. Chem. Soc.* **2015,** *137,* 13236-13239.

(120) Spenst, P.; Young, R.M.; Wasielewski, M.R.; Würthner, F. Guest and solvent modulated photo-driven charge separation and triplet generation in a perylene bisimide cyclophane *Chem. Sci.* **2016,** *7,* 5428-5434.

(121) Holman, M.W.; Yan, P.; Adams, D.M.; Westenhoff, S.; Silva, C. Ultrafast spectroscopy of the solvent dependence of electron transfer in a perylenebisimide dimer *J. Phys. Chem. A* **2005,** *109,* 8548-8552.

(122) Kim, T.; Lin, C.; Schultz, J.D.; Young, R.M.; Wasielewski, M.R. π-Stacking-Dependent Vibronic Couplings Drive Excited-State Dynamics in Perylenediimide Assemblies *J. Am. Chem. Soc.* **2022,** *144,* 11386-11396.

(123) Marcus, R.A. On the theory of oxidation ‐ reduction reactions involving electron transfer. I *J. Chem. Phys.* **1956,** *24,* 966-978.

(124) Marcus, R.A. On the theory of electron ‐ transfer reactions. VI. Unified treatment for homogeneous and electrode reactions *J. Chem. Phys.* **1965,** *43,* 679-701.

(125) Shao, Y.; Gan, Z.; Epifanovsky, E.; Gilbert, A.T.B.; Wormit, M.; Kussmann, J.; Lange, A.W.; Behn, A.; Deng, J.; Feng, X.; Ghosh, D.; Goldey, M.; Horn, P.R.; Jacobson, L.D.; Kaliman, I.; Khaliullin, R.Z.; Kuś, T.; Landau, A.; Liu, J.; Proynov, E.I.; Rhee, Y.M.; Richard, R.M.; Rohrdanz, M.A.; Steele, R.P.; Sundstrom, E.J.; Woodcock, H.L.; Zimmerman, P.M.; Zuev, D.; Albrecht, B.; Alguire, E.; Austin, B.; Beran, G.J.O.; Bernard, Y.A.; Berquist, E.; Brandhorst, K.; Bravaya, K.B.; Brown, S.T.; Casanova, D.; Chang, C.-M.; Chen, Y.; Chien, S.H.; Closser, K.D.; Crittenden, D.L.; Diedenhofen, M.; DiStasio, R.A.; Do, H.; Dutoi, A.D.; Edgar, R.G.; Fatehi, S.;

Fusti-Molnar, L.; Ghysels, A.; Golubeva-Zadorozhnaya, A.; Gomes, J.; Hanson-Heine, M.W.D.; Harbach, P.H.P.; Hauser, A.W.; Hohenstein, E.G.; Holden, Z.C.; Jagau, T.-C.; Ji, H.; Kaduk, B.; Khistyaev, K.; Kim, J.; Kim, J.; King, R.A.; Klunzinger, P.; Kosenkov, D.; Kowalczyk, T.; Krauter, C.M.; Lao, K.U.; Laurent, A.D.; Lawler, K.V.; Levchenko, S.V.; Lin, C.Y.; Liu, F.; Livshits, E.; Lochan, R.C.; Luenser, A.; Manohar, P.; Manzer, S.F.; Mao, S.-P.; Mardirossian, N.; Marenich, A.V.; Maurer, S.A.; Mayhall, N.J.; Neuscamman, E.; Oana, C.M.; Olivares-Amaya, R.; O'Neill, D.P.; Parkhill, J.A.; Perrine, T.M.; Peverati, R.; Prociuk, A.; Rehn, D.R.; Rosta, E.; Russ, N.J.; Sharada, S.M.; Sharma, S.; Small, D.W.; Sodt, A.; Stein, T.; Stück, D.; Su, Y.-C.; Thom, A.J.W.; Tsuchimochi, T.; Vanovschi, V.; Vogt, L.; Vydrov, O.; Wang, T.; Watson, M.A.; Wenzel, J.; White, A.; Williams, C.F.; Yang, J.; Yeganeh, S.; Yost, S.R.; You, Z.-Q.; Zhang, I.Y.; Zhang, X.; Zhao, Y.; Brooks, B.R.; Chan, G.K.L.; Chipman, D.M.; Cramer, C.J.; Goddard, W.A.; Gordon, M.S.; Hehre, W.J.; Klamt, A.; Schaefer, H.F.; Schmidt, M.W.; Sherrill, C.D.; Truhlar, D.G.; Warshel, A.; Xu, X.; Aspuru-Guzik, A.; Baer, R.; Bell, A.T.; Besley, N.A.; Chai, J.-D.; Dreuw, A.; Dunietz, B.D.; Furlani, T.R.; Gwaltney, S.R.; Hsu, C.-P.; Jung, Y.; Kong, J.; Lambrecht, D.S.; Liang, W.; Ochsenfeld, C.; Rassolov, V.A.; Slipchenko, L.V.; Subotnik, J.E.; Van Voorhis, T.; Herbert, J.M.; Krylov, A.I.; Gill, P.M.W.; Head-Gordon, M. Advances in molecular quantum chemistry contained in the Q-Chem 4 program package *Mol. Phys.* **2015,** *113,* 184-215.

Vita

Chenjian Lin

Northwestern University, 2145 Sheridan Rd., Evanston, IL 60208, U.S.
chenjianlin2023@u.northwestern.edu

Education

Northwestern University, Evanston, IL, U.S. **Sep 2018-Nov 2022**

Ph.D. candidate in Chemistry, Department of Chemistry, Weinberg College of Arts and Sciences

Peking University, Beijing, China **Sep 2014-Jun 2018**

Bachelor in Material Chemistry, College of Chemistry and Molecular Engineering

Research Experience

Prof. Michael Wasielewski group, Northwestern University **Aug 2018-Dec 2022**

Synthesized different series of blue-absorbed organic molecules and their oligomers in order to study the light harvesting processes, including 9,10-bis(phenylethynyl)anthracene[4], perylenediimide[1-3] and perylenemonoimide[5] derivatives, etc.

Studied the photophysical properties of the organic chromophores in solution[1-3, 8-9, 11], colloidal nanoparticles[4], thin films[5] and single crystals[5] to enhance the fundamental understanding of structure-property relationship of the light-matter interaction processes, especially in singlet fission[4-5, 8-9] and symmetry-breaking charge separation.[1-3]

Characterized the steady-state and transient photophysical processes by photoluminescence (fluorimetry) and transient absorption (TA)[1-11] spectroscopy, etc.

Prof. Michael Wasielewski group, Northwestern University, Internship **Jun 2017-Sep 2017**

Synthesized a terrylenediimide dimer which has the potential for singlet fission.

Prof. Chunhui Huang group, Peking University **Mar 2016-Jun 2018**

Independently designed and synthesized a group of lanthanide complexes, and characterized their emission by fluorimetry using UV and IR excitation.

First discovered room temperature up-conversion in a lanthanide complex series from 980 nm ytterbium excitation to 500 nm phosphorescence of organic ligands and to terbium visible emission.

Synthesized a hole-transporting material with high triplet energy and excellent hole mobility, which are favorable for OLED fabrication.

Research Skill

Organic Synthesis: Synthesizing organic compounds in air & moisture-free conditions on a Schlenk line; purifying compounds by recrystallization, sublimation, centrifugation and column chromatography; performing hydro-thermal reactions, etc.

Sample Preparation: Air-free solution preparation using the glovebox, freeze-pump-thawing or flame-sealing technique; thin-film fabrication by spin-coating or vapor deposition method; thin-film annealing by solvent vapor annealing or thermal annealing method; single-crystal growing by solution evaporation method, etc.

Characterization: Steady-state and time-resolved photoluminescence (fluorimetry), transient absorption (TA) spectroscopy, electro-chemistry (CV & DPV), UV-Vis absorption spectroscopy, NMR spectroscopy, mass spectrometry, thermal gravimetric analysis (TGA), etc.

Data analysis: Origin (plotting), Qchem (DFT & TD-DFT), Surface Xplorer (TA), Mercury (XRD), Matlab (fitting), Python, etc.

Publication

(1) **Lin, C.**[†]; Kim, T.[†]; Schultz, J.D.; Young, R.M.; Wasielewski, M.R. Accelerating symmetry-breaking charge separation in a perylenediimide trimer through a vibronically coherent dimer intermediate *Nat. Chem.*, **2022**, *14*, 786-793. ([†]Contributed equally to this work)

(2) Kim, T.[†]; **Lin, C.**[†]; Schultz, J.D.; Young, R.M.; Wasielewski, M.R. π-Stacking-Dependent Vibronic Couplings Drive Excited-State Dynamics in Perylenediimide Assemblies *J. Am. Chem. Soc.* **2022**, *144*, 11386-11396. ([†]Contributed equally to this work)

(3) **Lin, C.**; Young, R.M.; Wasielewski, M.R. Utilizing Mixed Electronic States in Donor-(Acceptor)2 Systems (manuscript prepared)

(4) **Lin, C.**; Bae, Y.J.; Young, R.M.; Wasielewski, M.R. Singlet Fission in Nanoparticle Solutions of 9,10-bis(phenylethynyl)anthracene Derivatives (manuscript prepared)

(5) **Lin, C.**; Yue, Q.; Brown, P.J.; Myong, M.; Zhao, X.; Young, R.M.; Wasielewski, M.R. Singlet Fission in Perylenemonoimide Single Crystals and Thin Films (manuscript prepared)

(6) Liu, W.; **Lin, C.**; Weber, J.A.; Stern, C.L.; Young, R.M.; Wasielewski, M.R.; Stoddart, J.F. Cyclophane-Sustained Ultrastable Porphyrins *J. Am. Chem. Soc.* **2020**, *142,* 8938-8945.

(7) Su, N.; Ma, R.; Li, G.; Liu, T.; Feng, L.-W.; **Lin, C.**; Chen, J.; Song, J.; Xiao, Y.; Qu, J.; Lu, X.; Sangwan, V.K.; Hersam, M.C.; Yan, H.; Facchetti, A.; Marks, T.J. High-Efficiency All-Polymer Solar Cells with Poly-Small-Molecule Acceptors Having π-Extended Units with Broad Near-IR Absorption *ACS Energy Lett.* **2021**, *6,* 728-738.

(8) Zhao, X.; O'Connor, J.P.; Schultz, J.D.; Bae, Y.J.; **Lin, C.**; Young, R.M.; Wasielewski, M.R. Temperature Tuning of Coherent Mixing between States Driving Singlet Fission in a Spiro-Fused Terrylenediimide Dimer *J. Phys. Chem. B* **2021**, *125,* 6945-6954.

(9) Zhao, X.; Bae, Y.J.; Chen, M.; Harvey, S.M.; **Lin, C.**; Zhou, J.; Schaller, R.D.; Young, R.M.; Wasielewski, M.R. Singlet fission in core-linked terrylenediimide dimers *J. Chem. Phys.* **2020**, *153,* 244306.

(10) Afraj, S.N.; Zheng, D.; Velusamy, A.; Ke, W.; Cuthriell, S.; Zhang, X.; Chen, Y.; **Lin, C.**; Ni, J.-S.; Wasielewski, M.R.; Huang, W.; Yu, J.; Pan, C.-H.; Schaller, R.D.; Chen, M.-C.; Kanatzidis, M.G.; Facchetti, A.; Marks, T.J. 2,3-Diphenylthieno[3,4-b]pyrazines as Hole-Transporting Materials for Stable, High-Performance Perovskite Solar Cells *ACS Energy Lett.* **2022**, *7,* 2118-2127.

(11) Qiu, Y.; Equbal, A.; **Lin, C.**; Brown, P.J.; Krzyaniak, M.D.; Wasielewski, M.R. Photoexcited chromophore-stable radicals as spin-polarized molecular qubits (manuscript submitted)

(12) Zhao, Z.; Bian, M.; **Lin, C.**; Fu, X.; Yu, G.; Wei, H.; Liu, Z.; Bian, Z.; Huang, C. Efficient green OLEDs achieved by a terbium(III) complex with photoluminescent quantum yield close to 100% *Sci. China Chem.* **2021**, *64,* 1504-1509.

Teaching Experience

Northwestern University, Teaching Assistant **Sep 2018-Mar 2020**

General Chemistry, Advanced General Chemistry (recitation and lab teaching assistant)

Additional Information

Languages: English (fluent), Mandarin Chinese (native), Cantonese (native), Korean (intermediate), Japanese (basic)

Other Skills: Video editing, live streaming, foreign language translation

Sports: Track & field (undergrad college team leader, #6 in 100 m sprint in Beijing), badminton, soccer, swimming, weight-lifting, etc.